Università di Pisa

Facoltà di Scienze Matematiche, Fisiche e Naturali
Corso di Laurea in Fisica

Tesi di Laurea Magistrale

TLD efficiency calculations with heavy ions

Relatrice:
Chiar.ma Prof.ssa
VALERIA ROSSO

Candidato:
DARIA BOSCOLO

Relatore:
Chiar.mo Prof.
MARCO DURANTE

Anno Accademico 2013/2014

TLD efficiency calculations with heavy ions

Contents

Abbreviations

ATM	Amorphous Track Model
CPE	Charged Particles Equilibrium
CPP	Compound Poisson Process
CPP-SC	Compound Poisson Process using Successive Convolution
CSDA	Continuous Slowing Down Approximation
ECLaT	Efficiency CaLculation for all Thermoluminescent detectors
ETIM	Extended Track Interaction Model
GSI	Helmholtzzentrum für Schwerionenforschung GmbH
GSM	Grid Summation Model
HCP	Heavy Charged Particle
HI	Heavy Ion
HTR	High Temperature Region
ICRU	International Commission on Radiation Units
IGK	Ion/Gamma-Kill
LEM	Local Effect Model
LET	Linear Energy Transfer
NIST	National Institute of Standards and Technology
PET	Positron Emission Tomography
RBE	Relative Biological Effectiveness
RE	Relative Effectiveness
TIM	Track Interaction Model
TL	Thermoluminescence
TLD	Thermoluminescent Detector
TRiP98	TReatment planning for Particles

Introduction

High energy beams of heavy charged particles offer significant advantages for treating deep-seated tumors with respect to conventional photon radiotherapy. Indeed, ions show an advantageous depth-dose distribution: a small amount of dose is deposited in the first part of their range, while a narrow dose peak is present at the end of the particles path (the so called Bragg peak). By varying the beam energy, the penetration depth (and thus the Bragg peak position) can be shifted. In this way, by superimposing several Bragg peaks, one can cover the tumor volume with a homogeneous dose distribution, substantially sparing the normal tissue surrounding the tumor. Moreover, charged particles are also characterized by a small lateral beam spread. Taking full advantage of these characteristic of ion beams, modern scanning beam systems allow to delivery the dose with millimeter and even sub-millimeter precision. Furthermore, ions heavier than protons exhibit an enhanced biological effectiveness, particularly at the Bragg peak (caused by a higher ionization density) which reduce the tumor cells repair capability.

The successful application of ion beam therapy critically depends on the capability to deliver the dose to the target volume with a high accuracy. However, these accuracy relies not only on the beam delivery system precision, but also on the capability to precisely measure the absorbed dose.

For this reason, devices capable of measuring the absorbed dose with a high precision and spatial resolution are needed. In general, absorbed dose distributions are experimentally verified by using ionization chambers. However, due to their dimensions and to the need of power supply, ionization chambers are not always suitable. In several circumstances the use of solid state detectors, such as thermoluminescent dosimeters (TLDs), or of radiographic films can be advantageous. In this thesis we will focus on the case of TLDs.

These detectors are widely used in conventional radiation detection and dose verification. However with the development of ion beam cancer therapy an extension of TLD usage is needed also for heavy charged particle radiation fields. Such an extension can

also be useful for space radiation protection purposes. Their main advantages, with respect to ionization chambers, are the small dimensions, ease of handling, the absence of interference with the radiation field and the usability in solid state phantoms. However, the response of TLDs with dose is non-linear and their response strongly depends on the quality of the radiation. For this reason, in order to use TLDs with particle beams, and specifically to get a prediction of their response in a treatment plan, a model that can reproduce the behavior of these detectors in different conditions is needed.

In literature, several models describing the TLDs behavior can be found and some of them will be introduced in the following: in particular, we focus on an extension of the local effect model (LEM). Even though the LEM was originally developed for predicting the response of biological systems following ion irradiation, it can also be extended to efficiency calculations of many solid state detectors, such as TLD.

In this context, a new, simple, and completely analytical algorithm for the calculation of the efficiency dependence on ion charge Z and energy E has been developed by the author of this work, in collaboration with the Biophysics Department of GSI (Helmholtzzentrum für Schwerionenforschung GmbH), Darmstadt. The aim of this work is the exposition of this algorithm, its comparison with other methods, the analysis of its validity and of its applicability in treatment planning.

This thesis is organized as follows. Chapter 1 summarizes the physical basis of heavy ion beam radiation damage: after describing the basic principles of the interaction of radiation with matter, we will introduce the main dosimetric quantities and characteristics of heavy charged particle dose deposition. Chapter 2 briefly reviews some of the most common detectors for dose verification, with a special focus on TLDs. Chapter 3 deals with theoretical models used to describe TLDs behavior, in particular it introduces the local effect model (LEM) [1] which will be used in this work. In Chapter 4 we describe several approaches, based on LEM, to compute the efficiencies of TLDs. We start with the approach introduced by Geiss [2], which correctly describes experimental data but relies on some *ad hoc* prescriptions which are not theoretically justified. For this reason we introduce a new algorithm for TLDs efficiency calculations, the Single Ion approach. In particular we study its limitations and its robustness, we compare the calculated efficiency values with experimental measurements and with the results of different methods. At the end of this chapter the results of signal calculation on macroscopic target are presented. These are performed by implementing efficiency tables calculated with the Single Ion approach on treatment planning tools. In Chapter 5 we summarize our results and briefly discuss the prospectives for future work.

Chapter 1

Physical basis of ion beam radiation damage

1.1 Interaction of radiation with matter

Ionizing radiations are radiations able to deliver enough energy to ionize atoms or molecules. These radiations can interact with matter in different ways depending on the medium as well as on the nature and on the energy of the radiation.

A general classification between directly and indirectly ionizing radiations is useful to better understand the different interaction processes of radiations with matter. Charged particles can directly ionize the atoms of the medium via Coulomb interactions with electrons and nuclei in matter.
Uncharged particles, such as neutrons or photons, are considered to be indirectly ionizing radiations, since they create secondary charged particles which then induce most of the ionizations and deposit most of the energy in the target material.

This section focuses on interactions of photons and particles in a energy range that is relevant in radiation therapy:

- photons with energies below 50 MeV;
- protons and ions with energies from 50 to 500 MeV/u.

1.1.1 Photons

An important difference between photons and charged particles interactions with matter is that the primary beam traversing the medium will not undergo a slowing down

processes but instead is attenuated in intensity. This can be explained considering that the main processes involved either remove the photons from the beam entirely or scatter them through a significant angle. Indeed, the photons which pass straight through the medium are those which have not suffered any interaction, therefore they retain the original energy. In this way the total number of photons is reduced only by the number of those who have interacted. The attenuation suffered by a photon beam is exponential with respect to the thickness, i.e.,

$$I(x) = I_0 e^{-\mu x} \tag{1.1}$$

with I_0 incident beam intensity, x the thickness of the absorber and μ the total absorption coefficient. The total absorption coefficient is characteristic of the absorbing material as well as of the photons energy and is directly related to the total interaction cross-section. Before turning to the calculation of the absorption coefficient, a short description of photon's interaction processes with matter will be done.

Usually one distinguishes between three ways of how photons can lose energy when interacting with matter: the photoelectric effect, Compton scattering and pair production.

Elastic scattering processes, such as Rayleigh or Thomson scattering, are less important in this context since no energy from the photons is transferred to the medium, no dose is deposited. Also possible, but much less common, are nuclear dissociation reactions, for example (γ, n), which we will neglect in our discussion as they give a negligible contribution to the dose rise.

Photoelectric effect. In the photoelectric effect the incoming photon is completely absorbed by one atom and, consequently, an orbital electron is released. The kinetic energy of the ejected electron is equal to the difference between the energy of the photon E_γ and the binding energy B_e of the electronic shell from which it was ejected :

$$E_{pe} = E_\gamma - B_e. \tag{1.2}$$

The reaction cross-section for this effect depends from the atomic number of the medium, as Z^n with $n = 4$ or 5, and from the energy of the photon as $E_\gamma^{-3.5}$ [3].
This effect is dominant for low photon energy, *e.g.*, below 40 KeV for targets with a low average atomic number, such as human tissue.

Compton effect. Compton scattering is an inelastic scattering of an incoming photon, with energy E_γ, and a bound electron. In this case the photon loses some of its energy and is deflected by an angle θ from its original direction. The electron is ejected

and the atom is ionized.
The energy of the scattered photon, E'_γ,can be calculated from the energy and momentum conservation [4]:

$$E'_\gamma = \frac{E_\gamma}{1 + \left(\frac{E_\gamma}{m_e c^2}\right)(1 - cos\theta)} \tag{1.3}$$

where m_e is the mass of the electron and c is the speed of light. The reaction cross-section for Compton scattering is proportional to $\frac{Z}{E_\gamma}$, where Z is the atomic number of the medium. The Compton effect is the dominant energy loss mechanism of photons in a range of energies between$\sim$ 100KeV and $\sim$ 30 MeV.

Pair production. In this process an electron and a positron are generated from a photon in the vicinity of a nuclear Coulomb field.
This process has an energy threshold of $2m_e c^2$, the rest mass of the electron and the positron. The photon exceeding energy is carried away as kinetic energy of the two particles which in turn will produce ionizations along their tracks. Pair production is a dominant process in material with high atomic number and for high energy photons.

Photon attenuation. The total probability for a photon interaction in matter is the sum of the individual cross-sections of the processes described above [3].

$$\sigma = \sigma_{photo} + \sigma_{Compton} + \sigma_{PairProduction} \tag{1.4}$$

The total absorption coefficient can be obtained multiplying the total cross-section by the density of the atoms, N,

$$\mu = N\sigma \tag{1.5}$$

The fraction of photons surviving a distance x is then

$$\frac{I(x)}{I_0} = e^{-\mu x} \tag{1.6}$$

where I_0 is the incident intensity.

The energy deposition in matter deviates from a pure exponential law in the entrance region of the irradiated volume, because in this region an equilibrium between the energy loss of the radiation field and energy absorption of the material has not been yet established. The surface effect is called *build-up* effect and is shown in Figure 1.1. In the distal region, behind the maximum peak, the equilibrium is established and the energy deposition decreases exponentially with the depth as in Eq. 1.6.

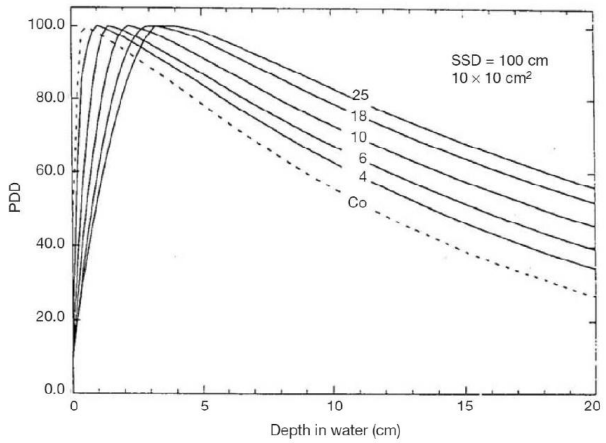

FIGURE 1.1: Percentage depth dose curves in water for a $10 \times 10\text{cm}^2$ field for various megavoltage photon beams ranging from ^{60}Co γ-rays to 25MV X-rays. Figure from [5].

1.1.2 Charged particles

The behavior of charged particles in matter is significantly different from the one of photons. In particular the photon's lack of an electric charge makes impossible the many inelastic collisions with atomic electrons, which are the main characteristic of the interaction of charged particles with matter.

The energy loss of a particle is primarily due to Coulomb interactions between their charge and the negative charge of the atomic electrons within the absorber. Depending on the proximity of the particles trajectory to a nucleus, the Coulomb's force may be sufficient to rise an electron to a higher-lying shell within the absorber atom (*excitation*) or to remove completely an electron from the atom (*ionization*). The direct removal of an electron from neutral atoms by the incident particle is called *primary ionization*. An ionization process looks like a collision between the charge particle and an orbital electron. The energy lost from the particle during these collisions is in part used to overcome the bending energy of the atomic electron and the remaining energy is given to the ejected *secondary electron* as kinetic energy. If this ejected electron has enough energy to ionize another atom is called δ-ray and represents an indirect way by which the charged particle energy is transfered to the absorbing medium. Under typical conditions, the majority of the energy lost by the charged particle occurs via δ-rays.

For high energy charged particles another energy loss process has to be taken into account. When an high energy charged particle passes through the Coulomb field of an atom, the most likely result is that the particle will simply be deflected by the strong repulsive forces exerted on it from the nucleus (*elastic scattering process*). Due to the deviation from the straight-line course, the particle is decelerated and loses energy:

this energy appears as a continuous X-ray spectrum called bremsstrahlung. Since this deceleration is proportional to the inverse of the particle mass, bremsstrahlung radiation will be much smaller for protons and heavy ions with respect to electrons. In general the deflection of a proton and especially of a carbon ion is extremely small and a very little energy is transferred in these collisions. For these reasons radiative energy loss can be neglected for ions at energies available at medical accelerators.

The particle projectile can also lose its energy interacting with the nuclei of the medium. The main process is due to the elastic collisions of the particle with the Coulomb field of the nuclei of the absorber. However, the contribution to the total energy transferred due to these interactions (so called nuclear stopping power) is much smaller than the one of the inelastic scattering with the orbital electrons, and dominates the stopping process only at the very end of the projectile path (the last few μm), *i.e.* speeds around and below the Bohr velocity v_0, which corresponds to a particle energy of 25 keV/u, as shown in Figure 1.2. Furthermore the corresponding dose contribution is very small and in general can be neglected in radiotherapy applications.

Since the contribution of nuclear interactions and radiative processes are very small, in order to describe the heavy ion energy loss only inelastic collisions with the orbital electrons of the medium will be treated in the following section.

Stopping power

The inelastic collisions are, of course, statistical in nature, occurring with a certain probability. However, because their number per macroscopic path length in dense matter is large, the fluctuations in the total energy loss are small. Thus, one can reasonably work with the average energy loss by the particle, dE, in traversing a distance dx in the material. This quantity is called *linear stopping power*, S, and is defined as [6]

$$S = -\left(\frac{dE}{dx}\right) \tag{1.7}$$

Another quantity, strictly related is the *mass stopping power* defined for a medium with density ρ as [6]:

$$\frac{1}{\rho}S = -\frac{1}{\rho}\left(\frac{dE}{dx}\right) \tag{1.8}$$

The mass stopping power is generally expressed in $\mathrm{MeVcm^2g^{-1}}$.

For a particle with speed v, charge z (in units of e) and energy E traversing a medium with atomic number Z, relative atomic weight A, density ρ and mean excitation potential I, the electronic stopping power can be expressed by the Eq. 1.9, which is commonly

referred to as Bethe-Bloch formula

$$\frac{1}{\rho}\frac{dE}{dx} = 2\pi N_A r_e^2 m_e c^2 z^2 \frac{Z}{A}\frac{1}{\beta^2}\left[\ln\frac{2\beta^2 m_e}{I(1-\beta^2)} - \beta^2 - \frac{C}{Z} - \frac{\delta}{2}\right] \tag{1.9}$$

with r_e the classical electron radius, m_e the electron mass, N_A the Avogadro's number, $\beta = \frac{v}{c}$, δ the density correction and C the shell correction factors.

The shell and density corrections occur for low and high energy respectively. The first one becomes relevant when the electrons can not be considered stationary with respect to the incident particle and, therefore, the speed of the orbital electrons has to be taken into account. On the other side, the density correction arises from the fact that the electric field of the particle tends to polarize the atoms along its path. This effect becomes more important as the energy of the particle increases.
The main parameter of the Bethe Bloch formula, however, is the mean excitation potential I that can be theoretically calculated or extracted from penetration depth measurements. This parameter appears in the term $\ln\left(\frac{1}{I}\right)$, in the bracket and the net effect is to decrease the stopping power as Z increases. Besides the mean excitation potential the shell and density correction, the dependence on the absorber medium of the stopping power appears also in the terms $\frac{Z}{A}$ outside the bracket, which makes the formula proportional to the number of electron per unit mass of the medium.

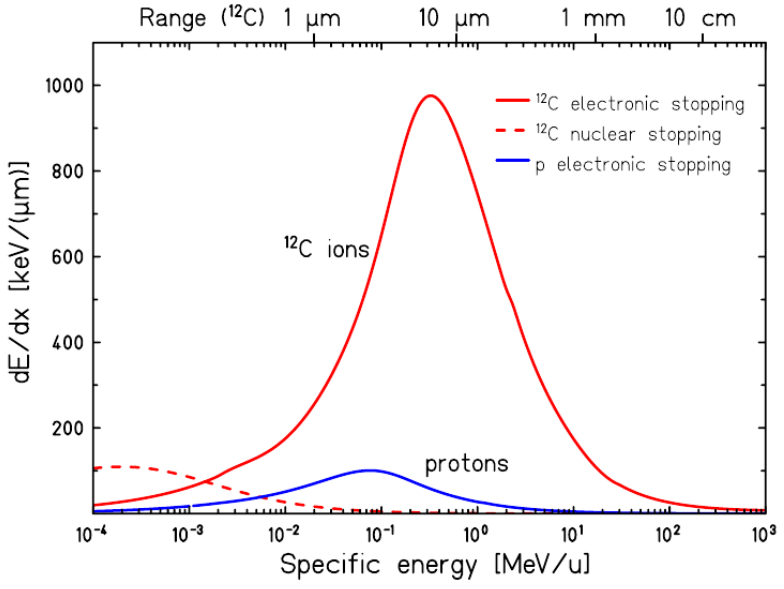

FIGURE 1.2: Specific energy loss dE/dx of ^{12}C ions and protons in water. At the top is indicated the range of ^{12}C ions in water corresponding to their specific energy. Figure from [7].

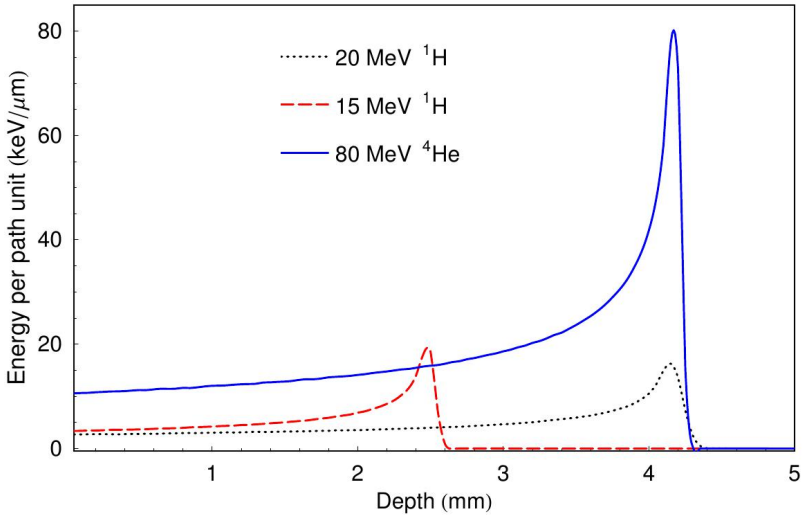

FIGURE 1.3: Bragg curves of various heavy charged particles at various energies obtained through computer simulation. The position of the peak is dependent on the velocity and charge of the particle and on the properties of medium.

Furthermore the stopping power depends on the particle charge with the term z^2. Thus, a doubly charged particle with a given velocity has 4 times the collision stopping power of a singly charged particle of the same velocity in the same medium.

However, the most relevant quantity in the Bethe Bloch formula is the velocity of the charged particle. At non-relativistic velocity the stopping power is dominated by the overall $1/\beta^2$ factor. The energy loss rapidly decreases with the increasing particle velocity until about $v \simeq 0.96c$, where a minimum is reached. As the energy increases beyond this point the term $1/\beta^2$ becomes almost constant and the stopping power rises again due to the logarithmic dependence inside the bracket.
In the very low energy region, when the speed of the particle can be compared with the one of orbital electrons, the dE/dx reaches a maximum and then drops sharply again. Here a number of complicated effects occurs. The most important of these is the electron capture, *i.e.* the tendency of the particle to pick up electrons. This lowers the effective charge of the particle and thus the stopping power. This effect can be taken into account replacing z by an effective charge z_{eff}, which can be described by the empirical Barkas formula [8]

$$z_{eff} = z(1 - exp(-125\beta\ z^{-\frac{2}{3}})). \tag{1.10}$$

Figure 1.3 shows the specific energy losses along the track (as a function of the penetration depth) for various charged particles at different initial energies. For most of the track the charge of the ions is equal to the nucleus charge and the specific energy loss increases roughly as $1/E$ as predicted by Eq. 1.9. Near the end of the track the charge is reduced through electron pick up (Eq. 1.10) and the curve falls off. The shape

of these so called *Bragg curves* is the main reason for using heavy charged particles in radiotherapy.

Range

From the stochastic point of view charged particles can be roughly characterized by a common path-length, traced out by most such particles of a given type and energy in a specific medium. Because of the multitude of interactions undergone by each charged particle in slowing down, its path-length tends to approach the expectation value, that in average will be observed for a very large population of identical particles. This expectation value define the range of the particles.
Another related quantity is the projected range, which is defined as the largest range that a particle may have in a medium in a given direction. Since heavy ions tends to follow a straight path inside the medium for these particles the difference between range and projected range is small.

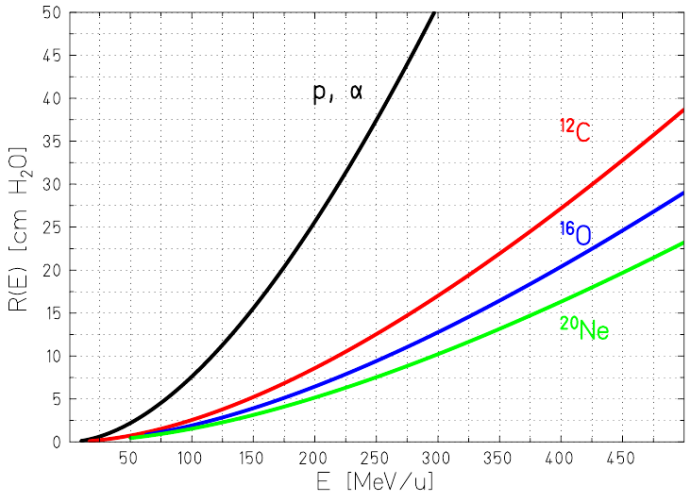

FIGURE 1.4: Mean range for heavy ions in water. Figure from [7].

Since the amount of energy transfered in each collision is generally a very small fraction of the particle total energy and, in the normal dense matter, the number of collision per unit path length is large, it can be assumed that the particle loses its energy continuously until the particle is stopped. This approximation is often referred as the "continuous slowing down approximation" (CSDA). Under this approximation the range of a particle with initial energy E_0 can be calculated from the stopping power as follow:

$$R_{CSDA} = \int_{E_0}^{0} \left(\frac{dE}{dx}\right)^{-1} dE \tag{1.11}$$

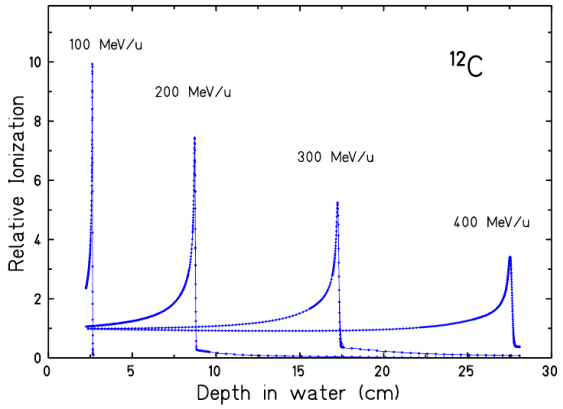

FIGURE 1.5: Measured Bragg curves of ^{12}C ions stopping in water. Figure from [9].

In reality, statistical fluctuations of the energy loss around its average value occur and cause a small spread of range values around the mean. This phenomenon is known as range straggling and is responsible for the larger width of the Bragg peak measured for an ion beam with respect to the calculation based on the average energy loss of a single particle. The range straggling increases with the penetration depth in a given material, resulting in Bragg peaks of larger width for higher initial energies of the same ion type, Figure 1.5. For different ion species the range straggling approximately varies as the inverse of the square-root of the mass. Therefore, at the same penetration depth heavier ions exhibit a narrower Bragg peak, Figure 1.6.

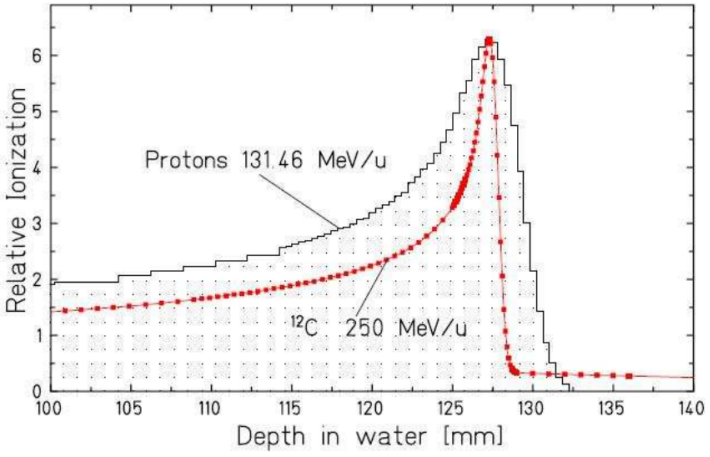

FIGURE 1.6: Measured Bragg peaks of protons and ^{12}C ions having the same mean range in water (normalized to the same peak height). Figure from [9].

Nuclear fragmentation

Although the probability of nuclear interactions is small, they leads to significant effects at large penetration depths. For this reason this processes will be briefly described in

this section.

The primary ion can undergo several different nuclear processes depending on the energy: interaction mechanisms go from transfer reactions, observed at low energies, to fragmentation processes, observed at the highest energies.

At low energies (< 20 MeV/u) the reactions can not be considered "*pure*" fragmentations. There are a lot of parameters which can determine a lot of different interactions varying from the elastic scattering to inelastic processes and fusion.
At high energies (> 200 MeV/u) violent nuclear interactions occur, a complete disintegration of both the target and projectile nuclei or a partial fragmentation can be observed. In general, the more frequent nuclear reactions, in this energy range, are peripheral collisions in which the projectile particle loses one or several nucleons. These kind of reactions can be described through a two step process. In the first step the nucleons, in the overlapping zone between the interacting projectile and target nuclei, are abraded, while the rest of the nucleons are assumed to undergo little changes in momentum. This phase can leads to the formation of highly excited pre-fragments which, during the second step called "ablation", lose their excitation by the emission of nucleons, clusters and γ-rays and re-arranges themselves corresponding to the remaining number of protons and neutrons. These fragments continues in the original beam direction with approximately the same beam velocity and contribute to the energy deposition until they are completely slowed down. Whereas the dose contribution from nuclear kickback is typically negligible, the spatial pattern of energy deposition is considerably affected by the secondary nucleons and fragments produced in nuclear reactions. For proton beams only the target nuclei can be involved in fragmentation processes. Vice versa for heavier ion beams the fragmentation concerns primarily the projectiles particles. One of the main consequences of nuclear fragmentation is, therefore, an exponential decrease of the primary particles fluence with the depth, x, according to the equation:

$$\phi(x) = \phi_0 e^{-Nx\sigma_R} \tag{1.12}$$

where ϕ_0 is the initial fluence, σ_R is the total reaction cross section, and N is the atomic density of the medium. On the top of Figure 1.7 the surviving fraction of ^{12}C ions of 200 MeV/u and 400 MeV/u traversing a thickness of water is shown. At 200 MeV/u still 70% of the primary ions reach the Bragg peak, whereas this fraction decreases to 30% at 400 MeV/u. This process leads to a build-up of lower-Z fragments along the penetration depth, this effect becomes more and more important with the increasing of the penetration depth. As an example, in Figure 1.8 are shown measured build-up curves for charged fragments of ^{12}C ions with $Z = 1$ to 5.

For kinematic reason , as already mentioned, these secondary fragments are moving in the same direction and with the same velocity as the primary beam. Since the range of particles with the same velocity scales as A/Z^2, these fragments have larger range compared to the primary ions. Therefore, they lead to an energy deposition behind the Bragg peak causing a characteristic tail in the depth dose distribution for larger depth, this phenomenon is shown in the lower panel of Figure 1.7.

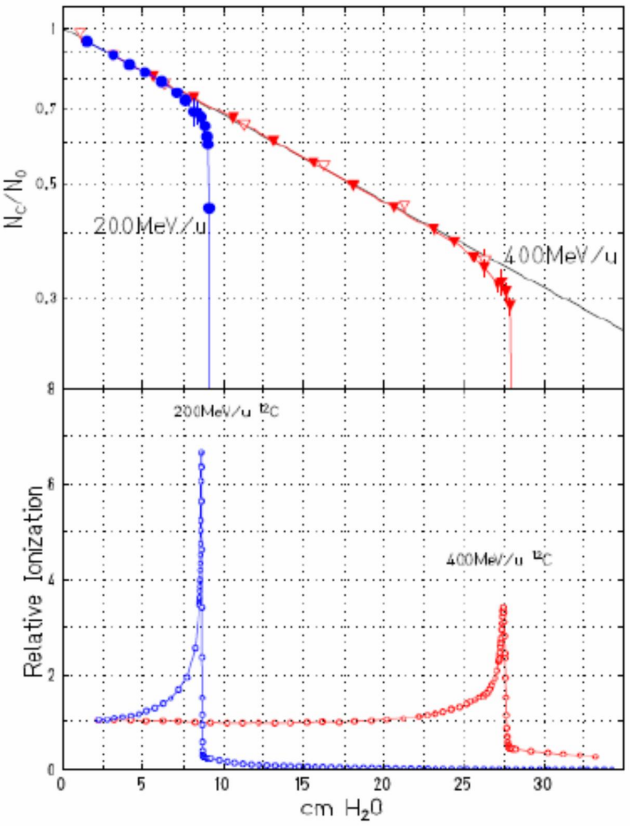

FIGURE 1.7: Top: Attenuation, due to fragmentation of primary carbon ions as function of the penetration depth in water for 200 MeV/u and 400 MeV/u. Bottom: two Bragg curves corresponding on the two energies. Figure from [10].

The angular emission of these secondary fragments contributes to a deterioration of longitudinal and transversal selectivity of the beam. Moreover, the effects of multiple Coulomb scattering are more pronounced for lower Z particles and this leads to an additional lateral spread of the beam.

The amount of fragments in general increases with the mass of the projectiles: in fact, it has been observed that for 400 MeV/u ^{20}Ne beam only 38% of the primary ions reach the Bragg peak at 16 cm depth in water, for ^{12}C ions the number of surviving with the same range is 52% [7]. For this reason ions heavier than ^{20}Ne are not advisable in therapy, carbon ions, instead, offer relatively good conditions. Furthermore the use of

positron emitters, like ^{11}C and ^{10}C offer the possibility to an *in vivo* range monitoring with positron emitting tomography (PET) techniques.

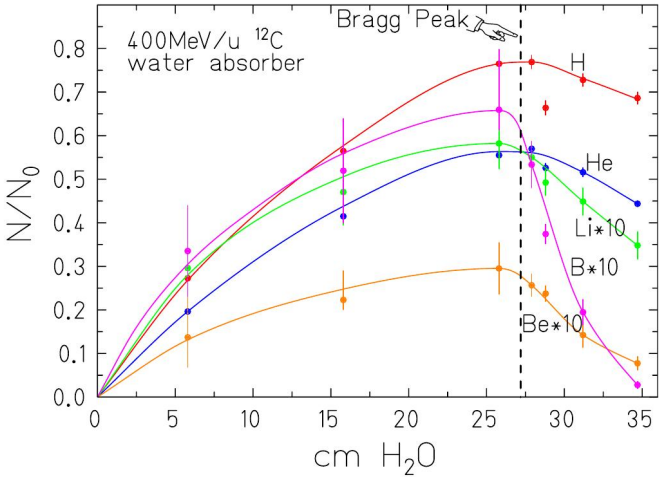

FIGURE 1.8: Build-up of secondary fragments produced by 400 MeV/u ^{12}C ions. Figure from [10]

.

1.1.3 Light charged particles: Electrons

Equations for the stopping of heavy charged particle (HCPs) can, to a certain degree, also be applied to electron projectiles. However, the details of the passage of electrons through matter are more complicated than in the case of HCPs. The main differences are the much smaller electron mass and the larger speed. Electrons may lose a large fraction of their energy in a single collision with an atomic electron and can be also scattered much more easily by nuclei than heavy charged particles: for these reasons their paths are usually not straight. In addition, for high energy electrons, the radiative mechanism for losing energy have to be also taken into account.

The electron path is, therefore, more branched compared to the one of a HCP, as shown in Figure 1.9. As the ionization events are scarce compared with that of HCP, electron radiation is considered as sparsely ionizing radiation. For the HCP the maximum range of the secondary electrons (*i.e.* δ-rays) emitted from the primary projectile decreases, with the decreasing of the HCP energy.

1.2 Dose distribution

Both photons and ions induce biological damage in matter via emission of secondary electrons, however, ion beams show a completely different spatial distribution of energy

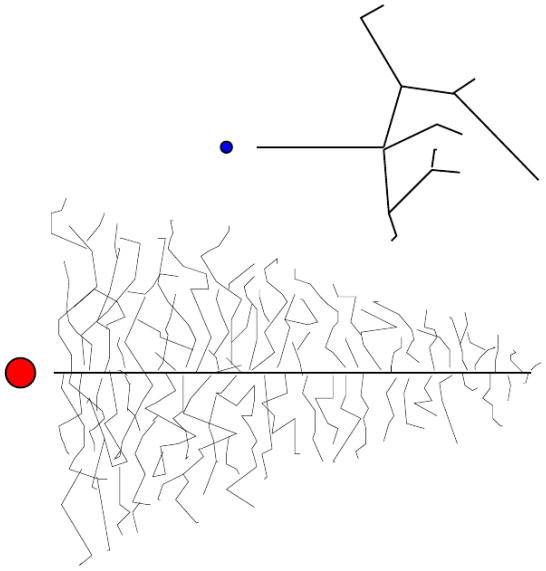

FIGURE 1.9: δ-ray track around an electron track (top) and a HCP (bottom)

deposition compared to photons. These differences lead also to different biological effects. However, before discussing the radiation dose deposition in matter, the more important dosimetric quantities have to be introduced.

1.2.1 Basics of Dosimetry

The aim of dosimetry is the calculation and assessment of the energy delivered from ionizing radiations to an absorber medium. For this purpose several specific dosimetric quantities have been introduced. The amount of energy absorbed by the irradiated medium can be established by the measurement or calculation of these quantities.

In dosimetry the following units and quantities definitions have been provided by the International Commission on Radiation Units and Measurements (ICRU) and are reported in the ICRU Report 60 (1998) [6].

Fluence. The number of particles entering in a volume of interest is a crucial quantity for all dosimetric considerations. The *particles fluence*, or simply the fluence, ϕ is defined as the quotient of dN by da, where dN is the number of particles incident on a sphere of cross sectional area da [6], thus

$$\phi = \frac{d\mathrm{N}}{d\mathrm{a}} \tag{1.13}$$

Fluence is measured in units of $1/\mathrm{cm}^2$.

Absorbed Dose. The *absorbed dose* is the most important dosimetric quantity. The definition of the absorbed dose is based on the concept of *energy imparted*. The energy imparted by ionizing radiation to matter within the volume V, with mass m and density ρ is defined as a stochastic quantity ϵ. Considering i particles interacting in the volume V, the energy imparted to it $\epsilon_{i,in}$ is the sum of energies from all charged and uncharged particles entering the volume , minus the energy of those leaving the volume $\epsilon_{i,out}$, plus any energy gains (or losses) Q from any nuclear reactions involved. Thus,

$$\epsilon = \sum_i \epsilon_{i,in} - \epsilon_{i,out} + Q \tag{1.14}$$

the absorbed dose is defined as the mean energy imparted in an infinitely small amount of matter, *i.e*

$$D = \frac{d\bar{\epsilon}}{d\mathrm{m}} \tag{1.15}$$

Dose is measured in Gray (Gy), which is defined as Jkg^{-1}. Dose is a macroscopic and non stochastic quantity.

For charged particle equilibrium (CPE) [1] condition the absorbed dose equals the product of particle fluence and mass stopping power

$$D = \phi \frac{1}{\rho}\left(\frac{d\mathrm{E}}{d\mathrm{x}}\right) \tag{1.16}$$

where ϕ is the primary particle fluence and $\left(\frac{1}{\rho}\frac{d\mathrm{E}}{d\mathrm{x}}\right)$ is the corresponding mass stopping power.

Linear Energy Transfer (LET). The *linear energy transfer* LET_Δ , sometimes also called *restricted linear collision stopping power*, is the amount of energy lost $d\mathrm{E}$ by a particle in a medium, due to secondary electrons with an energy less than Δ, over a distance $d\mathrm{x}$.

$$L_\Delta = \left(\frac{d\mathrm{E}}{d\mathrm{x}}\right)_\Delta \tag{1.17}$$

If Δ approaches ∞ the linear energy transfer gets numerically equal to the electronic stopping power, then

$$LET_\infty = \lim_{\Delta\to\infty} L_\Delta = \left(\frac{d\mathrm{E}}{d\mathrm{x}}\right)_{el} \tag{1.18}$$

In this work when referring to linear energy transfer we always intend LET_∞.

[1] Considering an irradiated volume V the CPE condition exist if, for every type of charged particles, entering and going out from the volume V the condition $\sum(T_{in})_c = \sum(T_{out})_c$ is verified. Where $\sum(T_{in})_c$ is the sum of the kinetic energy of a type of particle entering, c, in V and $\sum(T_{out})_c$ is the sum of the kinetic energy of the same type of particle going out from the same volume V. [11]

The SI unit for the LET is Jm^{-1}, usually dE is expressed in eV, or some convenient multiples or sub-multiples, and L_Δ in this thesis is expressed in MeVcm^{-1} .

1.2.2 Depth dose distribution

As already mentioned, the different energy deposition processes between photon radiation and heavy charged particle radiation lead to a completely different spatial dose deposition. The main difference concerns the depth dose distribution.

Photon radiation shows, according to the absorption low (Eq. 1.6), an exponential decrease of dose with depth. As mentioned in Section 1.1.1, for high energetic photon beams, the initial build-up, due to the forwarded Compton scattered electrons, shift the dose peak by few centimeters away from the surface.

The depth dose profile for heavy charged particles, on the other hand, is characterized by a distinct narrow peak at the end of their range, the Bragg peak. The depth position of this peak depends on the kinetic energy of the incident particles. This inverted depth dose profile make ions extremely suitable for ratiotherapeutic applications to deep seated tumors. The dose, indeed, is mainly deposited in depth (and thus in the tumor volume) with a high precision, sparing the normal tissue surrounding the tumor. Figure 1.10

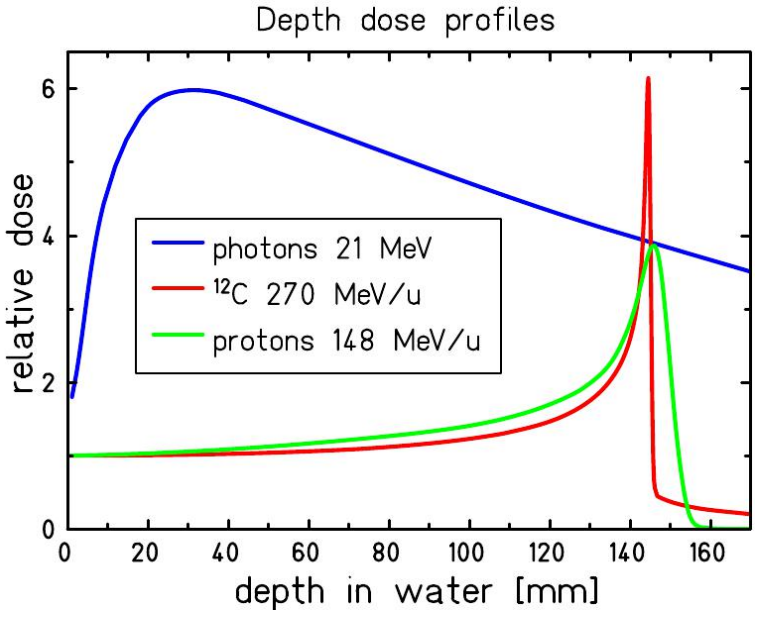

FIGURE 1.10: Depth dose distributions for 21 MeV photons, 148 MeV/u protons and 270 MeV/u carbon ions. Figure from [12].

shows different depth dose distributions for 21 MeV photons, 148 MeV/u protons and 270 MeV/u carbon ions.

For ion beam radiation therapy applications, in the case of active dose shaping devices (such as the GSI raster scan system), several weighted Bragg peaks of different energies are superimposed, in order to reach an uniform dose distribution on the tumor volume, as shown in Figure 1.11.

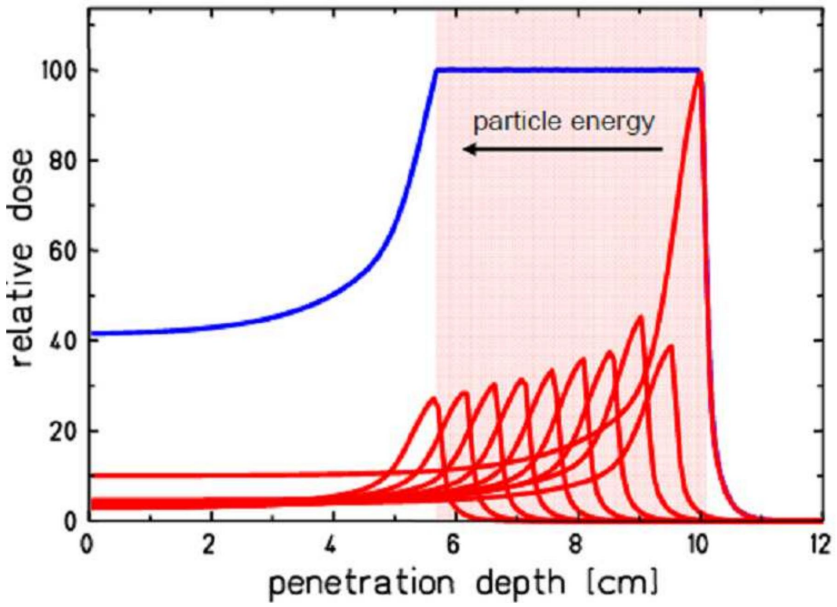

FIGURE 1.11: Extended target irradiation obtained by superimposition of intensity weighted Bragg peak of different energies. The distal peak is at the highest energy and intensity with respect to the others.

1.2.3 Radial Dose Distribution

Ion radiations differs from photon radiation also with respect to the microscopic spatial energy distribution.

Compton and photoelectric effects are the main processes involved in the photon energy deposition. During this processes secondary electrons are produced and, if the energy is sufficient, they can give rise to further ionization events producing tertiary and higher order generation electrons. The energy contribution of each photon in the absorber medium is small, therefore many photons are needed to reach doses in the order of 1 Gy. This leads to a random spatial distribution of the energy deposition events, *i.e.* to an homogeneous ionization density over the entire considered volume.

The energy distribution of heavy ions is completely different, Figure 1.12 shows a TRAX [13] simulation for proton and carbon ions of different energies in water. Looking at the figure is possible to notice that energy deposition in the target is still due to the emission of secondary electrons, however, the emission of these electrons is mainly peaked in a forward direction (ions are coming from the bottom). The fraction of secondary

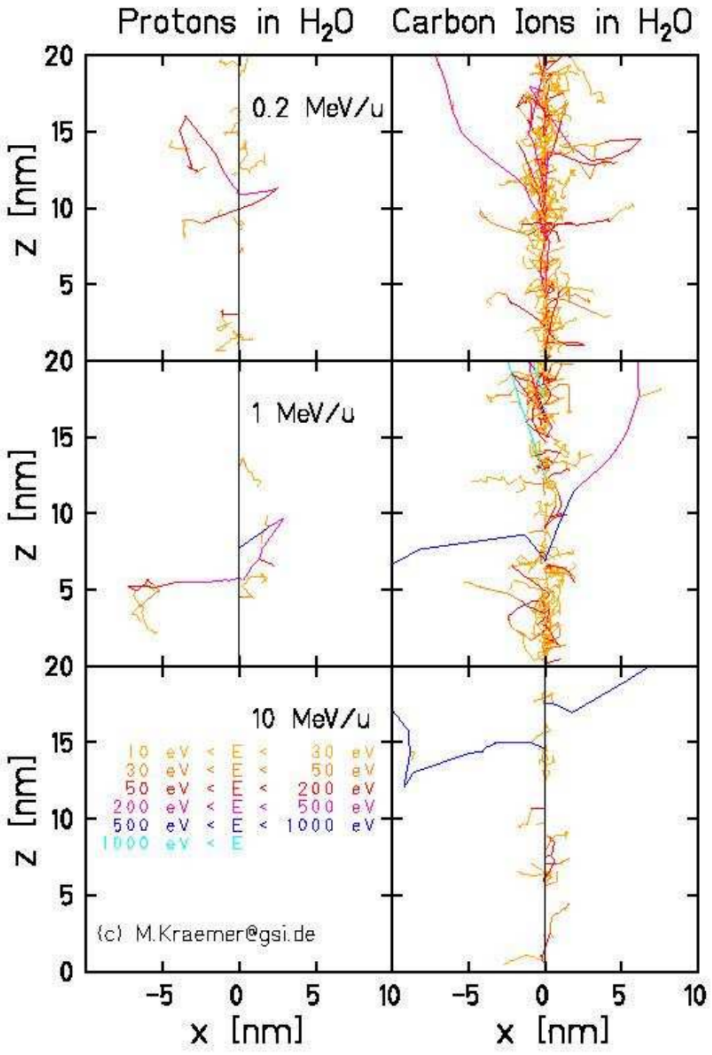

FIGURE 1.12: Simulated paths of δ-electrons created by ions of various energies (TRAX code [13]).

electrons emitted at large angles has, in general, comparably low energies, and thus short ranges. Therefore, the number of high energetic electrons, which can transport energy at large distances from the track, is small, and, thus,the spatial energy distribution is extremely localized along the trajectory of the primary ion [14]. In Figure 1.12, δ-rays are represented in different color depending on their energy (the energy color scale is reported in the bottom left of the figure). Hence, the spatial energy distribution is extremely localized along the trajectory of the primary ion [14].

The radial distribution of energy deposition within a particle track can be described in terms of the average dose deposition $D(r)$ as a function of the distance from the track center, r. In Figure 1.13 the so called radial dose profiles for carbon ions at different specific energy are shown. The radial dose distribution for intermediate distances from the track core is known to decrease with the inverse square of the distance. The width

of this distribution is related to the maximum range of the highest energetic electrons and depends on the energy of the primary particle: is larger for more energetic ions. However it is difficult to predict the radial dose distribution in the farthest, as well as in the closer, region from the path. This is due to uncertainties in electron range and energy relation, angular dependence of the secondary electron production cross section, and effects of δ-rays transport in matter, especially in medium with high atomic number.

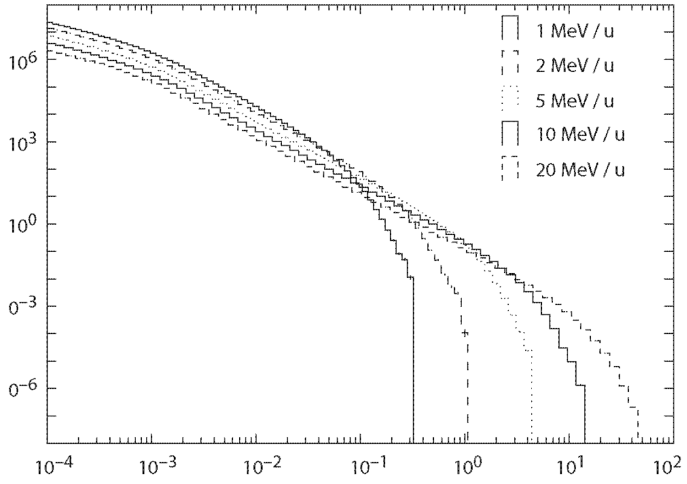

FIGURE 1.13: Local dose deposited in carbon ion tracks at different energies. Figure from [14].

In Figure 1.14 is shown a comparison between the microscopic distribution of energy deposition for photons and carbon ions at different energies. The different dose distribution are represented for the same average dose (2 Gy) delivered on a thin target with the typical size of a mammalian cell nuclei 10×10 μm. In the case of photons the distribution is flat and the expectation value of the energy deposition is homogeneously distributed.Low energetic, instead, ions exhibit an extremely high local dose, up to 10^6 Gy, deposited in a very small areas around the particle tracks, which is compensated by large areas between the track where no energy is deposited at all. It is significant to notice that, in order to reach the same dose, the number of particles increase with the decreasing of the LET (increasing of the energy) according with Eq. 1.16. Furthermore, the radius of the track increase with the energy, thus, the number of overlaps between ions track increases. Both this phenomenon, the increase of the fluence and of the overlaps, lead to an increasing homogeneity of the microscopic dose distribution with the increasing of primary ions energy.

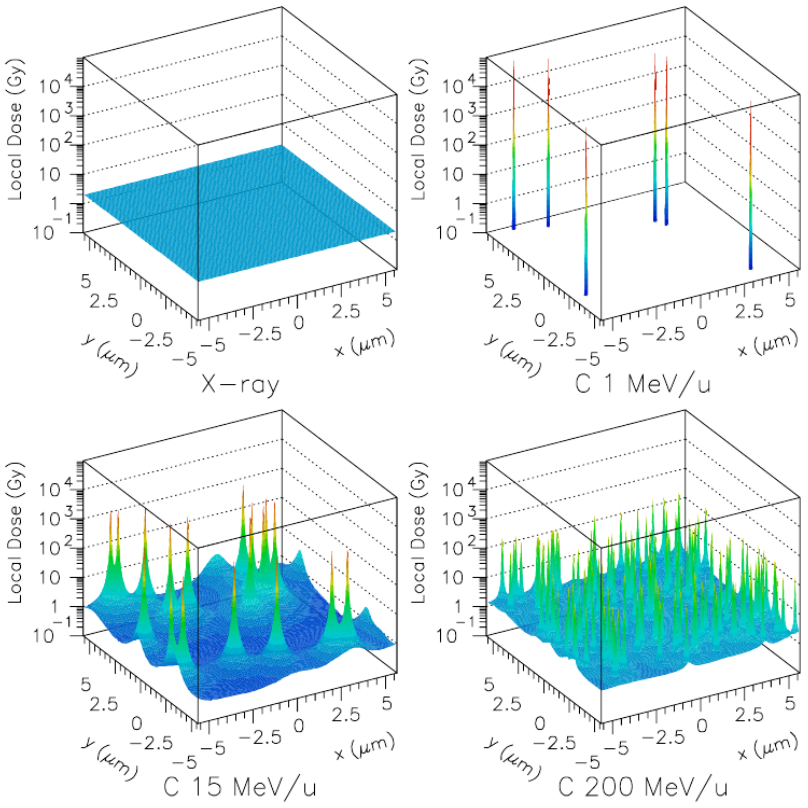

FIGURE 1.14: Microscopic dose deposition of photons (top left) and carbon ions at different specific energies. All the distributions are normalized to the same average dose of 2 Gy. Figure from [14].

1.3 Relative Biological Effectiveness

The changes in the biological effectiveness of radiations is the result of a complex combination of physical effects such as ionization density and biological parameters like the repair capability of the cell system. Therefore, the larger biological effect created by heavy ions radiation can be understood considering the different dose distributions of photons and ions. The high ionization density close to the particle track leads to a large probability of complex DNA damages such as clustered single or double strand breaks. In contrast, the homogeneous dose distribution of photons generates much more distant DNA damages. Since the repair capability of the cells decreases with the complexity of the DNA damage, the biological effect of heavy ion radiation is much larger than the one induced by photons.

Generally the capability of different radiations in killing cells are analyzed using the survival curves Figure 1.15. In these curves the fraction of survival cells is represented as a function of the dose. The most common way to parametrize the cell survival S is

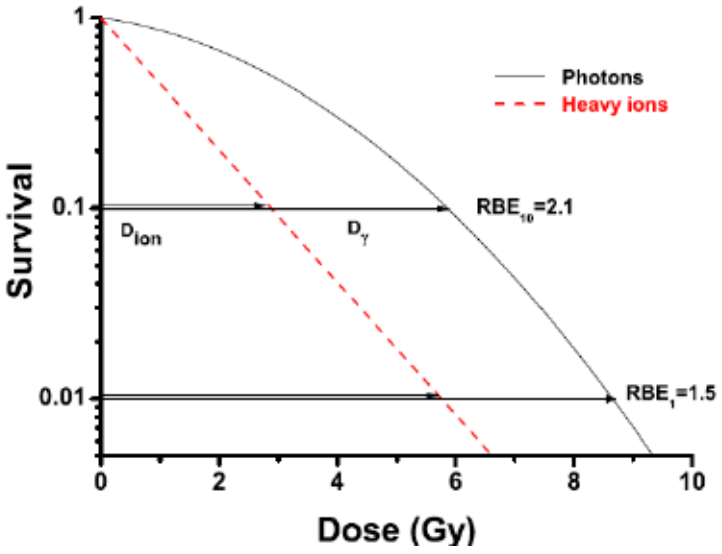

FIGURE 1.15: Definition of RBE for cell inactivation at two different survival levels 1% and 10%.

the linear-quadratic model,

$$S(D) = exp(-\alpha D - \beta\ D^2) \tag{1.19}$$

where D is the absorbed dose and α and β are specific coefficients characterizing the radiation response. The survival curve shows a typical shoulder shape determined by the ratio between α and β . This ratio is a very important quantity in radiotherapy because it is linked to the repair capability of the cells. Smaller value of α/β correspond to more pronounced shoulder of the dose response curve that means more repair capability.

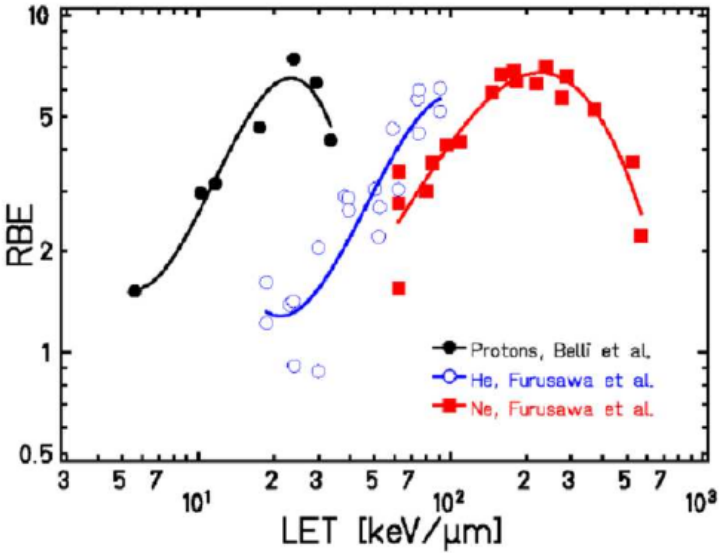

FIGURE 1.16: Dependence of RBE on LET and particle type. Figure from [14].

However, this is just a simplified description of the biological effects induced by radiation, the reality is much more complex and many other parameters occur. Some of them are taken into account considering the relative biological effectiveness (RBE). This quantity is defined as the ratio of the dose of a reference radiation (typically X-rays or γ-rays) to the dose of the radiation of interest, (e.g., ions) to produce an identical biological effect

$$RBE = \left.\frac{D_{ref}}{D_{ion}}\right|_{iso-effect} \tag{1.20}$$

In Figure 1.15 is shown the determination of RBE values by typical cell survival curves, where RBE values for cell inactivation are indicated for two effect levels 1% and 10%. As one can see from this figure the survival curve for heavy ions loses completely the "shoulder" (β approach to 0) due to the less capability of the cell to repair the high LET radiation damage. It is important to notice that each time a value of RBE has been provided the reference radiation and the level of biological effect have to be specified. Indeed, the value of RBE strongly depends on the effect level: the difference between photons and ions is high at low dose and decreases with the increase of the dose.

Moreover, for heavy ions different energies yield different dose effect curves. Qualitatively, this can be easily explained: for high energies (low LET) the track is wide, thus the ionization events occur far enough and make repair possible, yielding survival curves similar to sparsely ionizing radiations. With decreasing energy the diameter of the track shrinks and the LET increases. This leads to a high ionization density in the core of the track diminishing the repair possibility and yielding a significant increase of the RBE. At very high LET values, that means at the end of the particle path (for carbon ions is above 200 keV/μm) the local dose becomes higher than necessary for a lethal damage and the RBE decreases again[15]. In Figure 1.16 the dependence of the RBE from the energy of the particle for various ion is shown, it is important to notice that the position of the maximum of RBE changes for different ions.

The value of the radiobiological effectiveness , however, depends on many other parameter like the radiosensitivity of the cells and tissues, the fractionation scheme and the oxygenation. For all these reasons, finding a model able to predict the RBE with a good accuracy for all tissue types is a difficult task.

Chapter 2

Dosimeters

Radiation induced biological effects strongly depend on the dose. Therefore the capability to perform correct measurements or calculations of absorbed dose plays a key role for radiotherapy as well as for radiation protection. In radiotherapy, for example, the planned dose in the target volume should be delivered with an uncertainty of less than 5%, as recommended by ICRU (ICRU Report 24 [16]). Therefore, in order to ensure such high precision, for clinical application the dose measurement should be performed within an uncertainty lower than 1% [17]. For this reason devices able to measure the absorbed dose with an high precision and spatial resolution are needed. In this chapter some of the most wide spread detectors for dose verification in radiotherapy will be briefly overviewed.

2.1 Calorimeters

The most direct way to measure the absorbed dose is through calorimetry, under the assumption that the whole energy delivered by ionizing radiation within the medium is transformed to heat. The absorbed dose D is measured as a function of the temperature variation ΔT on a volume with a known mass and with a specific heat capacity c_p as

$$D = c_p \Delta T. \tag{2.1}$$

The use of calorimeter with the sensitive volume filled by water allows to get a direct measure of the adsorbed dose in water. However, calorimeter in graphite can be used for the same purpose as well, with the only precaution to convert the dose-to-graphite to the dose-to-water.

The measurement procedures require that the apparatus is in thermal equilibrium with the environment and that the irradiated volume is thermally isolated from its environment. These requirements are time consuming and laborious, which make the use of calorimetry outside the primary standard laboratory limited [18].

2.2 Ionization chamber

Gas filled ionization chambers are the most used detectors in dosimetry for radiotherapy. These dosimeters are based on the assumption that the dose deposited in a gas by ionizing radiation is proportional to the charge produced in the gas. It consists of a gas filled chamber with two electrodes. The electrodes exist in several designs, with a cylindrical outer electrode and a central electrode in the middle or two parallel plane electrodes. An electric field is create in the gas applying a voltage to the electrodes, thus the charge carriers, created by radiations ionizing the atoms of the gas, move to the electrodes where they can be measured. If J_c is the charge per unit of mass produced in the gas and the average energy required in order to produce an ionization event w is known, the dose deposited in the chamber D_c can be calculated by

$$D_c = J_c \frac{w}{e} \tag{2.2}$$

where e is the electron charge. However, the reading of ionization chambers require corrections for the influence of environmental conditions and charge recombinations.

Ionization chambers can be used for absolute and relative dosimetry, are reusable, offer an instantaneous dose measurement and have a high accuracy, however they need a power supply.

2.3 Semiconductor diodes detector

Although semiconductor detectors have been used mainly for gamma and X-ray spectroscopy, they are also very suitable as dosimeters.

A semiconductor diode dosimeter (usually silicon or germanium) is made of a $p-n$ junction. The bulk of the detector is constituted by a p region where the semiconductor material is doped with impurities which generate an excess of holes while a thin layer on the surface of the detector is a n region doped in such a way to create an excess of electrons. Electrons from the n region, near the p-n interface, tend to diffuse into the p region. In this diffusive process electrons leave in the n region positive charged ions.

At the same time holes from the p region near the p-n interface tend to diffuse into the n region leaving negative charged ions in the p region. Therefore, the region nearby the p-n interface, called *depletion layer*, becomes negatively charged on the p-side and positively charged on the n-side and generate an electric field which opposes the diffusion process for both electrons and holes. The equilibrium is reached when the electric field is strong enough to compensate the diffusion process.

Even in the absence of any external voltage, an electric field is thus generated at the interface between p-region and n-region and results in the so called built in voltage. When a charged particle passes through the depletion region, which is the active region of the detector, it produces electrons and holes. These charge carriers, under the influence of the above mentioned electric field, drift in opposite directions and generate a current which can be measured with an external amplifying circuit. In several applications, in order to increase the thickness of the depletion layer and the charge collecting efficiency, a reverse bias is applied.

Semiconductor detectors have several advantages with respect to ionization chambers. The energy required in order to produce an electron-hole pair in a semiconductor (in silicon is 3.6 eV) is ten times lower with respect to the energy needed for producing the same electron-hole pair in a gas (about 30 eV). Considering also that the density of a semiconductor, such as silicon, is about 1800 times that of the air, an ionizing particle passing through a silicon detector will produce approximately 18000 times as much charge as it would by passing through an ion chamber of the same volume [19]. This allow the construction of small detectors with a high energy resolution and a high reproducibility. Furthermore the time resolution is also very good.

2.4 Radiographic films

Radiographic films (photographic emulsions) are widely used for dosimetric measurements in radiation protection and radiation oncology [20]. Classic emulsions consist of microscopic grain, approximately of 1μm of diameter, of silver bromide (AgBr) placed in gelatin layers deposited on a supporting film.

The incident radiations can lead to a conversion of the Ag^+ ions in neutral silver atoms, Ag. Thus, each irradiated grain will contain some neutral Ag atoms (in general a grain contains approximately 10^{10} Ag^+ ions) which constitute the so called *latent image*. With a chemical process it is possible to develop the latent image: this process enhances the conversion of neutral silver atoms in the grain where some Ag atoms already exist, while it has no effect on the grain containing only Ag^+ ions, *i.e.* the ones which have not

been irradiated. At the end of this process the ions Ag^+ are removed leaving behind the opaque silver grains [19]. The presence of these neutral silver grains can be optically detected and it is related to the emulsion absorbed dose [11].

The effect of radiations results in an increased opacity on the film regions where larger doses have been deposited. The opacity level of a radiographic emulsion is measured by the *optical density* OD which is defined as

$$OD(x, y) = \log_{10} \frac{I(x, y)}{I_0} \tag{2.3}$$

where $I(x, y)$ is the intensity transmitted through the film point (x,y) when the film is illuminated with a light source of intensity I_0.

These dosimeters are characterized by a high spatial resolution and an high sensitivity. However, the relationship between the absorbed dose and the optical density is not linear and saturation effects occur when all the grain are irradiated. Furthermore the reproducibility of the signal strongly depends on the chemical developer process and in general it is difficult to reproduce the signal within an uncertainty better than 3% [11].

2.5 Thermoluminescent dosimeter, TLD

Thermoluminescent dosimeters (TLD) are widely used in personal dosimetry and medical applications. These devices are insulator or semiconductor materials with the capability to store information on the amount of ionizing radiation they have been exposed to. Subsequently they release these informations by emitting visible light when the material is heated (thermoluminescence, TL)[21]. The light emitted, typically in the blue or UV region, is proportional to the amount of absorbed energy.

Thermoluminescent materials are inorganic crystals, such as lithium fluoride (LiF) or calcium fluoride (CaF_2), containing suitable impurities which generate extra energy levels in the gap between conduction band and valence band, namely centers or crystal imperfections. It is possible to distinguish between two different kind of centers:

- Traps for the electrons and holes which can capture and hold charge carriers for long period of time;
- Luminescent center which emits light when electrons and holes recombine in such center.

Figure 2.1 schematically represents the thermoluminescence process. On the left panel, ionizing radiation creates a electron-hole pair. The electron is excited to the conduction

band where it migrates to an electron trap. At the same way the hole migrates to an hole trap. At room temperature these traps are deep enough (in terms of potential energy) to prevent the escape of the charge carriers from the traps. In order to liberate the charge carriers (detrapping), the crystal has to be annealed. The probability of releasing a trap

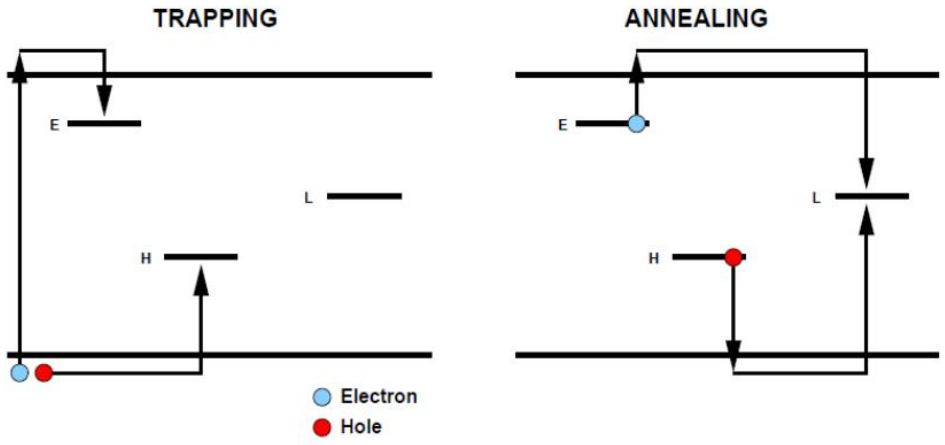

FIGURE 2.1: Trapping and annealing mechanism. E is an electron trap and H is an hole trap. L is the luminescence center for electron-hole recombination.

at temperature T is described by the Boltzmann distribution:

$$P(T) = s \cdot \exp\left(-\frac{\mathrm{E}}{\mathrm{k_B T}}\right) \tag{2.4}$$

where E is the trap energy depth, T is expressed in Kelvin, k_B is the Boltzmann's constant and s is called *frequency factor*. The latter depends on the lattice defect and in a simplified model can be assumed independent from the temperature. $P(T)$ increases with the temperature, and, then, the releasing probability of electrons and holes which are in the deeper traps increases by heating the crystal. The released charge carriers can now recombine and, if these recombination processes take place in luminescent centers, are accompanied by light photons, as shown in the right panel of Figure 2.1.

These photons can be detected with a photomultiplier which yields the so called *glow curve*: a curve which shows the thermoluminescent signal versus the temperature. By referring to the Eq. 2.4, as already mentioned it is possible to notice that, assuming constant values for E and s, the escaping probability $P(T)$ increase with the temperature T. Thus the released charge carriers rate will increase with the increase of T reaching a maximum at temperature T_m. This maximum is followed by a decrease of the signal due to the fact that the number of trapped electrons or holes is gradually exhausted [19]. Assuming that the number of recombinations in the luminescent centers is proportional to the charge carriers escaping rate, a maximum of the TL will be observed at T_m, which is called *glow peak*.

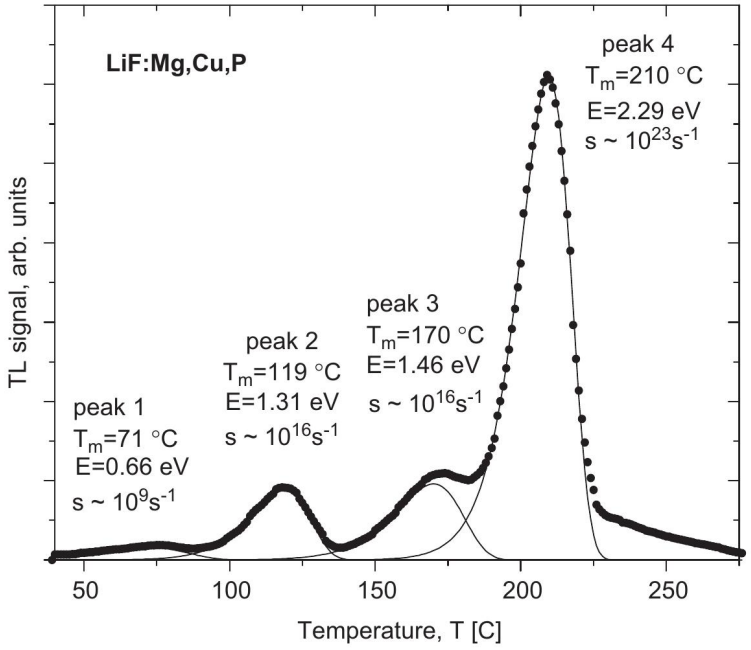

FIGURE 2.2: TL glow curve of LiF:Mg,Cu,P (lithium fluoride activated with Mg, Cu and P) detector irradiated with 10 Gy of ^{137}Cs γ-ray. Figure from [22].

The presence of more than one peak in the glow curve indicates the presence of traps at different energy depths E, within the crystal. An example of a glow curve is shown in Figure 2.2, the area below the curve is proportional to the amount of energy deposited within the detector by ionizing radiation.

In this work we will mainly focus on TLD consisting of lithium fluoride doped with magnesium and titanium (LiF:Mg,Ti), in particular we will refer to TLD-700 material which is LiF:Mg,Ti enriched in ^{7}Li. This is one of the most common type of TLDs and is widely used in medical dosimetry thanks to is low atomic number ($Z_{eff} = 8.2$) which only slightly differs from the tissue one ($Z_{eff} = 7.4$). A glow curve of TLD-700 is shown in Figure 2.3. Several peaks are visible in this figure, the largest is the so called peak 5 which has also a good temporal stability (half-life ∼80 years) and thus is one of the most important ones for dose estimation. The region beyond the peak 5 is known as high temperature region (HTR) where it is possible to notice the so called peak 6 or 7 which is the sum of several peaks, whereas for temperature lower respect to peak 5, the peak 2,3 and 4 are visible.

2.5.1 Signal Stability and reproducibility

The independence on time and on environmental conditions as well as the reproducibility of the readings are fundamental requests for the use of thermoluminescent material in dosimetric applications. Indeed, if the traps are not stable, *i.e.* they recombine before

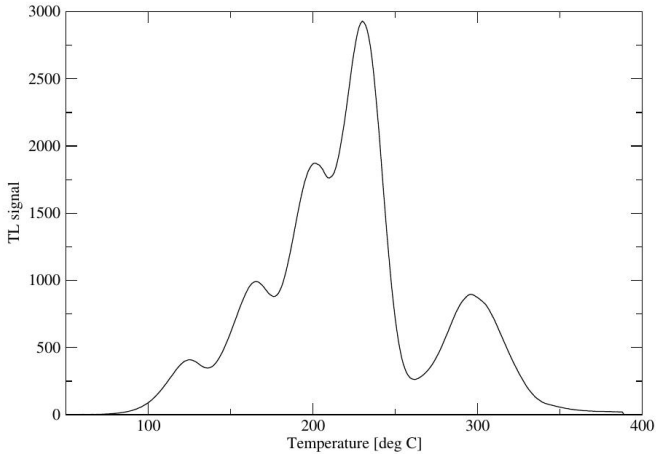

FIGURE 2.3: An example of TLD-700 glow curve.

the annealing process, distortions of the glow curve and alterations of the detector sensitivity can be observed. This process is called *trap leakage* and depends on two main factors: the room temperature and the half-life of the traps. High temperature traps are more stable and the leakage is smaller compared to lower temperature traps. Generally that the traps life corresponding to glow peak at $\simeq$200℃ have a half-life in the order of years, whereas glow peaks around $\simeq$100℃ have a half-life of the order of hours [19].

For this reason, in order to ensure a signal stability of the detector, TLDs are generally pre-annealed before starting the read out process at relatively low temperature (approximately 100℃): in this way the light contribution from the low temperature peaks is removed and the leakage is reduced.

Moreover, only a small part of the absorbed dose is converted in thermoluminescence. The ratio between the energy emitted as light during the heating process ε and the energy absorbed during the irradiation ε_0 is called intrinsic efficiency and is indicated with α, [23], thus

$$\alpha = \frac{\varepsilon}{\varepsilon_0} = \frac{N_{TL} h\nu}{mD} \tag{2.5}$$

where N_{TL} is the number of photon emitted during the annealing process and $h\nu$ is their energy, m is the average mass irradiated and D is the dose absorbed by the mass m. However, it is difficult to measure the intrinsic efficiency, indeed many processes contribute to the energy conversion such as the charge carriers production, the trapping and the detrapping processes, recombination etc [23]. For LiF (TLD-100), the intrinsic efficiency has been measured by Lucke as 0.039% [24].

Due to the low intrinsic efficiency and the strong dependence of the many processes TLDs can be used only under reproducible condition in order to ensure accurate and consistent results.

2.5.2 Dose response curve

Although it would be desirable for a TLD detector to have a linear dose response over a wide range of doses [22], most of TL phosphors show a supralinear response for doses above approximately 10Gy and all the TL materials saturate at very high doses. The deviation of the signal from linearity is usually described with the linearity index, $f(D)$, defined as

$$f(D) = \frac{TL(D)/(D)}{TL(D_0)/(D_0)} \tag{2.6}$$

where D is the given dose and $TL(D_0)$ is the TL signal for a low dose value D_0 which is within the linear region.

The dose response curve of TLD-700 is shown in Figure 2.4, where it is possible to notice that the detector response becomes supra-linear at doses of approximately 100Gy, whereas for doses larger than 10^4Gy a saturation of the detector response can be observed.

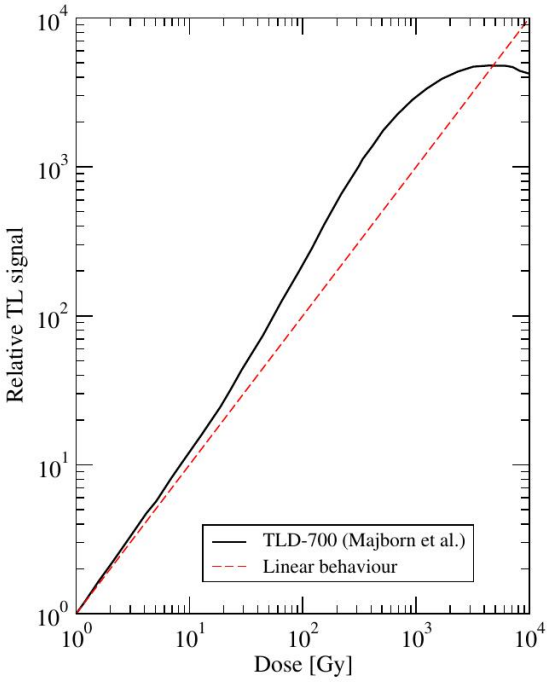

FIGURE 2.4: Dose response curve for TLD-700 material exposed to ^{60}Co γ-rays.

Chapter 3

Detector efficiency calculations: models

With the development of heavy ion accelerators and of ion beam therapy the interest in heavy charged particles dosimetry, and particularly dosimetry with solid state detectors, increased remarkably.

The main advantage of this kind of detectors, compared to the ionization chambers, is the higher signal, due to their high ionization density. This allows the achievement of higher spatial resolution and smaller dimensions of the detectors. However, the high ionization density leads also to saturation effects and non linear responses with the dose, as shown in Chapter 2. This characteristic cause a straight dependence of the detector response on the dose distribution which is one of the main limitations for the use of this kind of detectors in heavy charged particles (HCPs) dosimetry. Moreover, the response of these detectors depends also on the quality of the radiation. As an example, Figure 3.1 shows the glow curves of a TLD-700 after irradiation with 50 mGy of ^{60}Co γ-rays and 50 mGy of ^{20}Ne ions with a LET of 31.6 keV/μm [25].

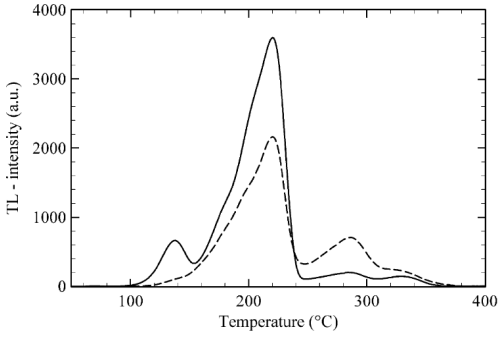

FIGURE 3.1: TLD-700 glow-curves after 50 mGy of ^{60}Co (solid line) and 50 mGy of ^{20}Ne ions with a LET of 31.6 keV/μm (dashed line). Figure from [25].

Furthermore, unlike photon radiation which creates a nearly uniform dose distribution over the whole detector, HCPs generate an extremely localized dose deposition along the trajectory of the primary ions. Several models describing the radial dose distribution around a particle path exist ([26], [1], [27], [28], [29] etc.). All of them predict a decrease of the dose with the radial distance r from the track center proportional to $1/r^2$ and, most of them, expected local dose values even higher than 10^6 Gy for r values below 1 nm [30]. Therefore, considering a detector characterized by a linear-supralinear-saturated dose response curve irradiated with an HCP, this detector will saturate in the closer region surrounding the track core, then it will respond in a supra-linear way for the intermediate distances and linearly for the external part of the track, as shown in Figure 3.2. The total signal will be the combination of the contributions of all these three regions.

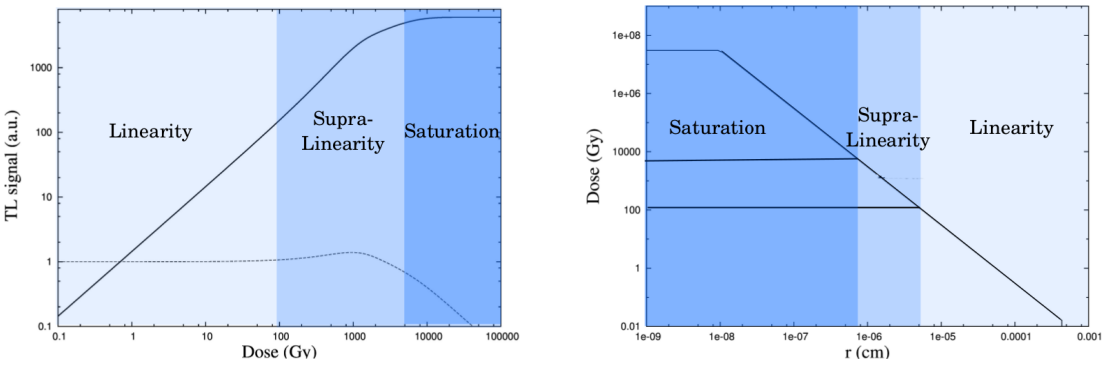

FIGURE 3.2: On the left panel: the solid line represent a dose-response curve of a solid state detector, exhibiting three different regimes: a linear, supra-linear and saturated response whereas the dashed line is the deviation of the signal from linearity. On the right, the radial dose distribution of a single ion. The deposited dose decreases with the distance from the center of the track, crossing all three aforementioned response regimes.

The radial dose distribution around an HCP is much more sharp when the particle is in the Bragg peak region with respect to the radial dose distribution of the same particle in the plateau of the depth dose profile. Therefore, the contribution to the saturation is larger for particles at the end of their path and, then, the efficiency of the dosimeter decreases with the increasing linear energy transfer (LET) of the considered particle.

The knowledge of efficiency curves of such detectors for HCPs dosimetry is therefore mandatory [2] [20] [31]. Several models with the aim of describing the efficiency of detectors under particle fields exist and it is possible to distinguish two main groups:

- Microdosimetric models
- Track structure models

In this chapter only track structure models, and specifically amorphous track structure models, will be presented with a special focus on TLDs. Before starting with the description of the various models the concept of relative effectiveness will be introduced.

3.1 Relative Effectiveness

The absolute or intrinsic efficiency, α, of a solid state detector is defined as the ratio of the mean energy detected ε_0, to the mean energy imparted to the detector by the radiation field ε, Eq. 2.5,

$$\alpha = \frac{\varepsilon_0}{\varepsilon} \tag{3.1}$$

The determination of this intrinsic efficiency is highly complex since various physical processes are involved [32]. Therefore, in order to describe the behavior of a dosimeter in a radiation field x different from the reference radiation field (usually ^{60}Co or ^{137}Cs γ-rays), the relative effectiveness (RE) η is used. In literature the definition of the RE is not unique, basically there are two definitions used [33]. There is the iso-response definition,

$$\eta_{iso-response} = \left.\frac{D_{ref}}{D_x}\right|_{iso-response} \tag{3.2}$$

which is the ratio between the dose applied with the reference radiation D_{ref} and the dose of the radiation type x, D_x, yielding the same detector response. It has to be noticed that this definition is similar to the definition of the relative biological effectiveness (RBE), which can be seen as the biological counterpart to the RE.

The alternative definition is the ratio of the response of the detector irradiated with radiation x, $S(D_x)$, to the response after irradiation with reference radiation, $S(D_{ref})$, at the same nominal dose.

$$\eta_{iso-dose} = \left.\frac{S(D_x)}{S(D_{ref})}\right|_{iso-dose} \tag{3.3}$$

In the following of this work only the iso-dose definition will be used. A schematic representation of these two quantities is shown in Figure 3.3

3.2 Amorphous track models

Amorphous track models (ATM) , are a group of models with the aim of describing the response of a system irradiated with HCPs following a phenomenological approach.

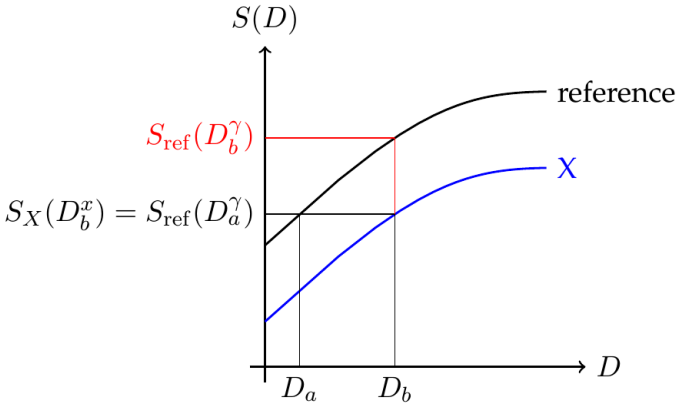

FIGURE 3.3: Schematic illustration of both RE definition.

These models, unlike 3D track structure models, do not describe in full detail the propagation of a track but consider the radial dose profile represented as a homogeneous dose distribution in the irradiated sample [34]. ATM are based on three main assumption:

- The dose deposition around the ion track can be described by a continuous radial dose profile.
- The effects of HCP radiations are mainly due to the secondary and higher order electrons and the contribution of each of these electrons does not depends on their origin. Thus, the local response of the detector to the various order electrons is the same and depends only on the local dose level.
- The detector response can be calculated folding the low-LET (photon and electron radiation) dose-response curve of the detector with the inhomogeneous dose distribution.

In the following sections three different approaches will be briefly described. At first the Butts and Katz model will be introduced. In this model the detector response is calculated from the activation probability of a sensitive center within the detector and the radial dose distribution is calculated using the Rutherford scattering cross section formula for the secondary electrons. Afterwards, the track interaction model (TIM), which determine the detector response with consideration on the recombination probability, will be treated and, finally, the local effect model (LEM) will be described. The latter was originally conceived for biological systems but can also be extended to many solid state detectors. In this model the effect of HCPs radiation on a sensitive target is calculated convolving a parametrization of the radial dose distribution around an ion track with a parametrization of the low-LET dose response of the detector.

3.2.1 Butts and Katz model

This amorphous track structure model was first introduced by Butts and Katz in 1967 in order to predict the response of enzymes and viruses to heavy ion irradiation [35]. Later this model was applied by Katz et al. to explain the supra-linearity of thermo-luminescent dosimeters [36][37][26].

This model is based on the fact that the structure of the track of an heavy charged particle is determined by the radial distribution of the dose deposited by secondary electrons all around the primary ion trajectory. This dose deposition has cylindrical symmetry above the ion path with a width determined by the maximum range of δ-electrons, beyond which the dose drops to zero.

The detector is characterized by sensitive (cylindrical or spherical) elements, called targets. These elements can be activated by *"hit"* which represent a single event with enough energy to change the state of the element. After the activation the element is supposed to be stable: the state will not change even if other events occur afterwards. Many detectors such as photographic emulsions, alanine, scintillators as well as some biological processes like DNA single strand breaks and enzymes and virus inactivation need 1-hit in order to produce a signal. However, there are some types of photographic emulsions that need more than one hit for being activated. The latter are called multi-hit detectors. Furthermore, there are other systems which need the activation of more than one target in order to produce the observed end-point. An example of such multi-target detectors are cellular chromosomes [36].

Since the hits are independently distributed, the probability for activation can be described by the Poisson formula. In an uniform radiation field, for example γ-rays, in which in average there is one hit per target ($\bar{N} = 1$), the probability of not being hit ($n = 0$), is :

$$P(n = 0) = \frac{\bar{N}^n e^{-\bar{N}}}{n!} = e^{-1} \simeq 0.37. \tag{3.4}$$

The macroscopic dose of γ-rays at which each element is hit in average one time, or in other words, the dose at which 37% (e^{-1}) elements are not hit, is a characteristic parameter of the detector and is generally indicated as D_{37}. The average number of hit for a macroscopic dose D of γ-rays can be calculated as $\bar{N} = D/D_{37}$.

Considering 1-hit detector irradiated with a dose D of sparsely ionizing radiation. The probability to be activated, P_1 (the probability to receive at least 1-hit) is given by one minus the probability of not being hit $P(n = 0)$.

$$P_1 = 1 - P(n = 0) = 1 - e^{-\bar{N}} \tag{3.5}$$

Whereas for a 2-hit detector, the activation probability P_2 is given by the probability to be hit at least two times:

$$P_2 = 1 - (P(n=1) + P(n=0)) = 1 - (1 - \bar{N})e^{-\bar{N}} \tag{3.6}$$

In the case of a 2-target detector activated by 1-hit the probability to reach a signal is given by

$$P(m=2) = (1 - P(n=1))^2 = \left(1 - e^{-\bar{N}}\right)^2 \tag{3.7}$$

Hence, the gamma dose-response curve of 1-hit, 2-hit and 1-hit 2-elements detectors will follow respectively Eq. 3.5, Eq. 3.6 and Eq. 3.7. TLDs shown a combination of 1-hit and 2-hit response, thus

$$TL_\gamma(D) = R \cdot P_1 + (1 - R) \cdot P_2 \tag{3.8}$$

with R being a weight factor which represents the fraction of 1-hit targets inside the detector. Systems like these show a supra-linear region in the dose response curve, which means that doubling the dose the response may increase more than twice.

In order to calculate the response of these detectors to heavy charged particles another parameter related to the size of the sensitive element has to be introduced: a_0 the radius of the target. The values of a_0 can be determined from high-LET radiation experimental results and are varying on a broad range, depending on the detector type: it can be in the order of a silver bromide grain for photographic emulsions down to the the size of the nucleus for a cell.

Considering a detector characterized by a 1-hit and a 2-hit components with respectively characteristic doses D_{37_1} and D_{37_2}, the calculation of the response after ion irradiation has to be done separately for the two components. First the 1-hit component, k_1, will be calculated.

According to Eq. 1.16 the dose deposited by the ion beam is $D_{tot} = \phi \times LET$. The TL signal is given by the activation probability of 1-hit sensitive target:

$$k_1 = 1 - e^{-\sigma_1 \phi} \tag{3.9}$$

with σ_1 the activation cross section for a single particle. The response of the detector after irradiation with ions can be calculated, according to the amorphous track structure theory, using the radial dose distribution around the ion as a transfer function relating the low LET response of the detector to its high LET response. The radial dose distribution around the ion path used by Butts and Katz is calculated using the Rutherford

scattering cross section formula for the secondary electrons and is given by [38]

$$D(r) = \frac{N_e e^4 Z_{eff}^2}{\rho_m \alpha m_e c^2 \beta^2 r^2} \left(1 - \frac{r}{r_{max}}\right)^{\alpha} \tag{3.10}$$

where Z_{eff} is the effective charge of the ion calculated according to the Barkas formula (Eq. 1.10), N_e is the density of the electrons and α is a parameter that can be extracted by fitting experimental data. In this work the derivation of the radial dose will not be treated while a complete description can be find in [35].

The activation cross section can be calculated integrating the activation probability (Eq. 3.5) all over the track of the incident ion, thus

$$\sigma_1 = 2\pi \int_{r_{min}}^{r_{max}} P_1\left(\frac{\bar{D}(r)}{D_{37_1}}\right) r \mathrm{d}r \tag{3.11}$$

where r_{max} is the maximum range of δ-rays and r_{min} is usually set about 1 Å or 10^{-2} Å [37]. $\bar{D}(r)$ is the average dose deposited by secondary electrons in a sensitive target of radius a_0 centered at a distance r from the projectile track.

The 2-hit component calculation is more complicated and the concept of *ion-kill* and *gamma-kill* has to be introduced. With the expression *ion-kill* is called an activation event in which the hits, needed in order to get the signal, are given by δ-rays produced by a single ion. Alternatively, an activation process in which the hits are produced by δ-rays coming from different ion tracks is called *gamma-kill*. The time scale of ion-kill processes is above 10^{-15} s, whereas the time scale involved in gamma-kill processes is in the order of the irradiation time [39]. The fraction of elements inactivated by ion kill processes will be, therefore, the initial population of gamma-kill. The fraction of the dose deposited on the detector by ion kill mode, P_I, is given by the ratio $P_I = \sigma_2/\sigma_0$. σ_0 is called saturation cross section and represents the geometrical cross section scaled by an empirical factor and σ_2 is the single ion inactivation cross section for a 2-hit detector. The latter can be calculated with Eq. 3.11 substituting P_1 with the 2-hit cumulative Poisson distribution, P_2, Eq. 3.6.

$$\sigma_2 = 2\pi \int_{r_{min}}^{r_{max}} P_2\left(\frac{\bar{D}(r)}{D_{37_2}}\right) r \mathrm{d}r \tag{3.12}$$

Therefore, the probability of an element to not being activated in the ion-kill mode, Π_i, is

$$\Pi_i = e^{-\sigma_2 \phi}. \tag{3.13}$$

Afterwards the remaining fraction of the dose ($(1 - P_I)D_{tot}$) is deposited via gamma-kill mode. The probability of not being activated by gamma-kill processes, Π_γ is also given

by the 2-hit cumulative Poisson distribution, however, this time the remaining dose has to be used and not the average dose delivered in a sensitive element, $\bar{D}(r)$.

$$\Pi_\gamma = 1 - P_2\left(\frac{(1-P_I)D_{tot}}{D_{37_2}}\right) \tag{3.14}$$

The fraction of sensitive elements inactivated over a population of N_0, after a given dose or fluence, is given by the product of the surviving probability after ion-kill mode times the surviving probability after gamma-kill:

$$\frac{N}{N_0} = \Pi_i \Pi_\gamma. \tag{3.15}$$

Thus, the response of the detector for the 2-hit component will be:

$$k_2 = 1 - \Pi_i \Pi_\gamma. \tag{3.16}$$

Finally, the response of a detector characterized by a mixture between 1-hit and 2-hit behavior, irradiated in a known ion field, will be the sum of the two components weighted by their respective contributions:

$$TL(D_i) = Rk_1 + (1-R)k_2. \tag{3.17}$$

The relative effectiveness can be, thus, calculated using Eq. 3.8 and Eq. 3.17.

3.2.1.1 Hansen and Olsen

Hansen and Olsen in 1984 adapted the Butts and Katz track structure model to one hit detectors, in particular they focused on dye films and alanine dosimeters [29], [40]. This model will be briefly described since, in this thesis, one hit detectors will not be treated, a complete discussion can be found in Hansen PhD thesis [40].

The relative effectiveness is defined as the ratio between the low-LET sensitivity, k_γ, and the one for high-LET radiations, k_i. The former is given as $k_\gamma = D_{37}^{-1}$, whereas for the latter, k_i is given by the ratio between the total activation cross section, σ , and the mass-stopping power:

$$k_i = \sigma\left[\frac{1}{\rho}\left(\frac{dE}{dx}\right)\right]^{-1}. \tag{3.18}$$

Hence, the effectiveness is given by:

$$\eta_{i,\gamma} = \frac{k_i}{k_\gamma} = \sigma D_{37}\left[\frac{1}{\rho}\left(\frac{dE}{dx}\right)\right]^{-1}. \tag{3.19}$$

As in Katz model the activation cross section, for 1-hit detector, can be calculated as in Eq. 3.11 where the activation probability is described by Eq. 3.5.

The most important difference with respect to the Katz model is the formulation of the radial dose distribution. Under the assumption of infinitesimal short track-thickness, the integral of the radial dose distribution around the ion track should be equal to the tabulated mass stopping force. On the other hand, in the Katz model this is not verified and the integral of the dose distribution gives values lower than the stopping power. In Hansen's model this issue is fixed with the definition of a core region of radius a_0 centered on the ion path which is considered separately from the rest of the track. The dose in this area is assumed to be constant and its value is given by the subtraction of the energy deposited in the rest of the track from the total energy delivered by the ions thus

$$D_{core} = \frac{1}{\rho}\left(\frac{dE}{dx}\right) - 2\pi \int_{a_0}^{r_{max}} D(r) r dr \tag{3.20}$$

where r_{max} is the maximum range of secondary electrons. In this way the difference between the LET and the integral of the radial dose distribution is added to the core. The size of the core region, a_0, is assumed to be equal to the size of the sensitive element and is determined by fitting experimental data, for alanine detector a_0 is in the order of 3 nm.

A similar formulation of the radial dose distribution was given by Chatterjee and Schaefer [41]. In this model it is assumed an equipartition of the energy transfer to the medium between glancing and close collisions. The former leads to excitation processes whereas the close collisions cause ionization events. A core of the track is defined as the central region of the track in which glancing collisions prevail whereas outside the core the energy deposition is mainly due to secondary electrons and only ionization events occur, this region is called penumbra .

From the assumption of equipartition of the energy, half of the total energy is delivered in the track core via excitation processes. However, in order to estimate the dose delivered in the inner part of the track, the contribution of ionization processes, in this region, has to be also taken into account. The radial dose in the track core is assumed to be constant (similarly to Hansen and Olsen model) while the width of this region change depending on the velocity following the empirical formula:

$$r_c = 0.0116\beta \tag{3.21}$$

where β is the relativistic expression for the velocity.

3.2.2 Track interaction model: TIM

The track interaction model (TIM) was introduced by Claffy and Attix [42] [43] during the 1970ies in order to explain supra-linear response of TL dosimeters following photons irradiation. Successively the supra-linearity and saturation of heavy charged particle TL-fluence response was modeled in TIM context by Horowitz [44].
The main assumption is that the electrons and holes produced along the ion trajectory spread radially away from the center of the ion path and are trapped near the track. This will results in an highly localized cone-like distribution of charge carriers, trapping centers and recombination centers.

The TIM models requires two different type of recombination centers: the thermoluminescence centers and other electron-trapping competing (non-radiative) centers [45]. After the capture of one electron the latter ones are inhibited. Therefore, when irradiating with HCPs the competing centers inside the particle track are all de-activated whereas in the region outside the particle track no charge carriers capture occurs and the competing centers are still all active [45].

The basic idea is that at low dose (low fluence) the recombination processes occur in a localized region in which the competitive non radiative processes are suppressed. In the case of sparsely ionizing radiation this is verified when the realized electrons have an high probability to recombine with their own holes. Whereas in the case of ion radiation the localized region is the area surrounding the ion track, in other world, this is verified when the recombination process (in the heating stage) occurs between charge carries and luminescent centers from the same track. Electrons escaping from the track, in fact, recombine with non radiative competing centers, thus no TL signal is produced in the inter-track region. In this condition the detector response is linear with the dose. With the increase of the fluence (high dose) the track distance decrease. When the average distance is lower than the migration range of the charge carriers it is possible that an electron escaped from the parent track reach a TL recombination center of a neighboring track. In this condition, therefore, the probability of recombination with TL centers increases, causing a supra-linear TLD dose response.

An extension of the TIM (ETIM) has been developed by Horowitz et al. [45] [46]. In this extension in addition to the supra-linear response also the saturation of TLDs is described. Furthermore the track structure and the track interactions are treated in a more sophisticated way. Since this work will not focus on the track interaction model all these extensions will not be further discussed.

3.2.3 Local Effect Model: LEM

The "Local Effect Model"(LEM), was developed by M. Scholz [1] [47] [48] with the purpose of predicting the response of biological systems following ion irradiation. This model has been successfully applied during the pilot project in GSI and presently is also implemented in a commercially available treatment planning system .

As the other models described in this work it relates the biological effects due to ion radiation to the corresponding effects after X-ray radiation. The critical target for cellular effects is assumed to be the cell nucleus, therefore the cellular response is entirely determined by the spatial dose distribution inside this target. The cell nucleus is divided in small sub-volumes in which the dose is assumed to be homogeneous. The dose delivered in each volume element, by the various ions passing through the nucleus, is calculated using an amorphous track structure model described in the following and their response is extrapolated from X-ray response curve at the corresponding dose level. The total effect on the cell is, therefore, calculated integrating the sub-volumes response over the entire cell nucleus. In Figure 3.4 is shown a schematic representation of the LEM basic idea.

Since the number of lethal events in a cell is assumed to be Poisson distributed, the survival probability (the probability to have $n = 0$ lethal events) after receiving a dose D is given by:

$$S(D) = P(n = 0, N_{ion}) = e^{-N_{ion}(D)}. \tag{3.22}$$

Where N_{ion} is the average number of lethal events and depends on the three dimensional dose distribution, $d(x, y, z)$ as follow:

$$N_{ion} = \int_{V_{nucleus}} \nu_{ion}[d(x, y, z)]dV \tag{3.23}$$

where ν_{ion} is the average number of lethal events per unit volume inside the target, $V_{nucleus}$. Assuming that the the local effect depends only on the dose distribution, and not on the radiation type, it follows that $\nu_{ion}(d) = \nu_x(d) = \ln S_x(d)/V$. Hence, the average number of lethal events due to ion irradiation can be related to the effect of photon radiation as shown in Eq. 3.24, which represents the most general formulation of LEM. Thus,

$$N_{ion} = \int_{V_{nucleus}} \frac{\ln\left(S_x[d(x, y, z)]\right)}{V} dV. \tag{3.24}$$

The survival curve is parametrized using the linear-quadratic model, see Eq. 1.19. Whereas, the radial dose distribution around an ion track is described with an amorphous track structure model which assume a constant dose in the track region close to

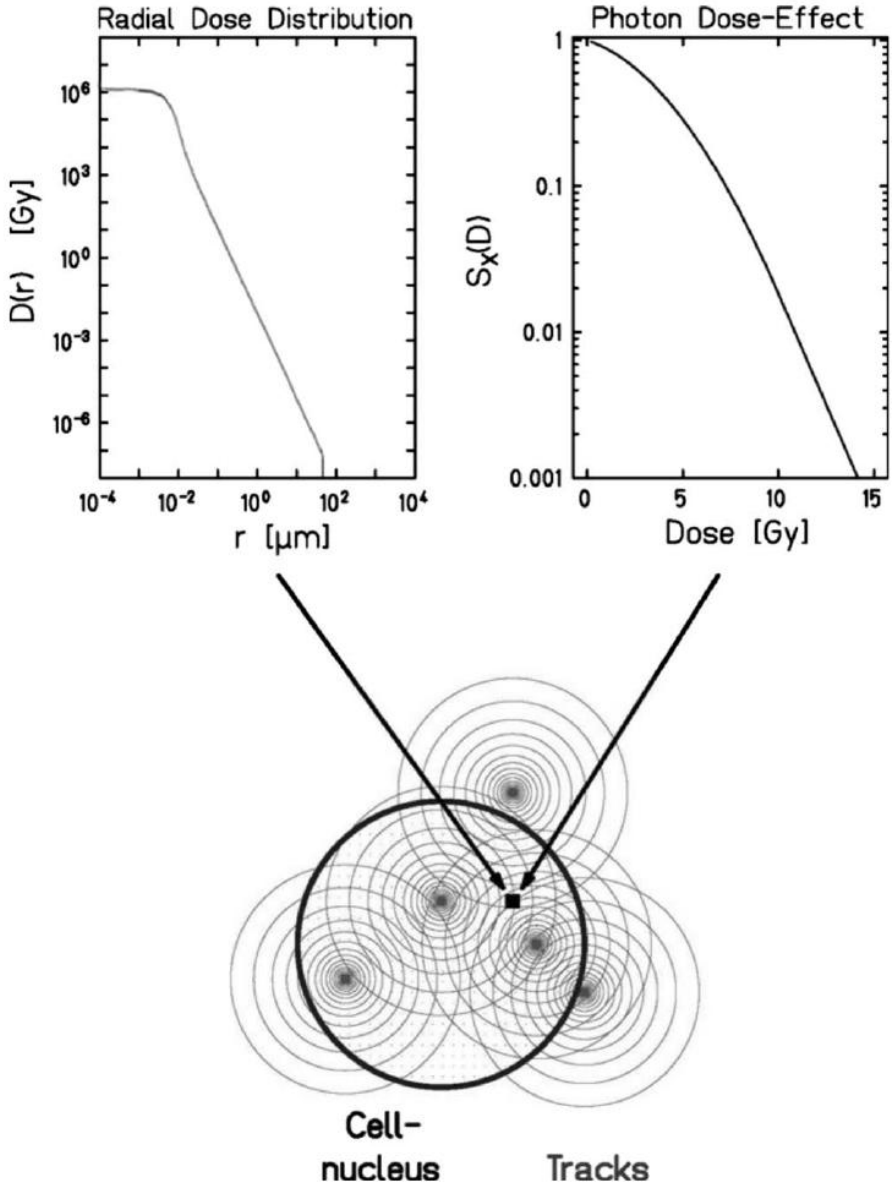

FIGURE 3.4: Schematic representation of the local effect model.The red circles correspond to the iso-dose levels.

the projectile trajectory and a dose decrease following a $1/r^2$ dependence in the outer part.

$$D(r) = \begin{cases} \lambda LET/r_{min}^2 & \text{if} \quad r \leq r_{min} \\ \lambda LET/r^2 & \text{if} \quad r_{min} < r < r_{max} \\ 0 & \text{if} \quad r_{max} < r \end{cases} \tag{3.25}$$

Where λ is a normalization factor chosen so that the integral of the radial dose distribution has to be equal to the LET. The maximum radius of the track, r_{max} represents the largest distance that the secondary electrons can reach. It depends on the energy of

the primary ion, E, and is determined by the following parametrization:

$$r_{max} = \gamma E^{\delta} \tag{3.26}$$

if r_{max} is expressed in μm and E in MeV/u, γ is equal to 0.062 and δ to 1.7. Whereas r_{min} is the core radius, it was assumed constant in the earlier version of LEM: $r_{min} = 10$ nm or $r_{min} = 0.3$ nm depending on the version. However, as in Chatterjee track model, in more recent versions the size of this region is assumed to be dependent on the ion velocity:

$$r_{min} = \beta_{ion} r_c \tag{3.27}$$

where β_{ion} is the relativistic speed of the ion and r_c describes the largest extension of the track core in the limit condition $v = c$ and it is chosen to maximize the agreement with experimental data [7].

Even if the local effect model has been developed in order to predict response of biological system following ion irradiation, it can be extended also for the efficiency calculations of many solid state detectors. In the following section a LEM-like model based on probabilistic approach will be presented whereas in the next chapter two implementation for TLDs efficiency calculations will be described.

3.2.3.1 Compound Poisson processes using successive convolution (CPP-SC)

The CPP-SC algorithm is a probabilistic approach based on Kellerer algorithm [49] developed by Greilich [50]. The main idea is to apply the Kellerer algorithm to fold the probability density function calculated from the radial dose distribution and to use it for calculating the response of some solid state detectors for heavy ions.

The iso-dose relative effectiveness is calculated for an homogeneous detector, positioned perpendicular to the beam, of negligible thickness Δz, according with Eq. 3.3.

In order to calculate the average response of the detector when irradiated with a beam of fluence ϕ of heavy charged particle with energy E and charge Z, a reference point P inside the detector is considered.
The probability frequency of having a dose d on P, $f(d)$, depends on the fluence, ϕ, and on the radial dose distribution around the ion path, $D(r)$.
Assuming r_{max} being the maximum range of secondary electrons, it is possible to assert that the dose contribution on the point P is due to the ion tracks passing within a circle C of radius r_{max} centered in P, see Figure 3.5. The number, n, of these track is Poisson distributed and with mean $\mu = \phi \cdot 2\pi r_{max}^2$.

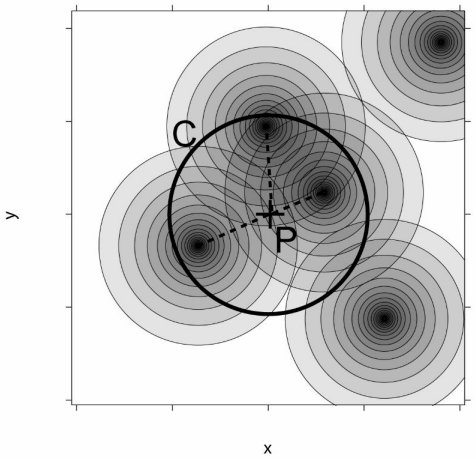

FIGURE 3.5

For a single particle passing in C, the cumulative distribution function of the local dose, $F_1(d)$, can be obtained from the inverse of the radial dose distribution $R(d) = D^{-1}(r)$ as

$$F_1(d) = 1 - \left(\frac{R^2(d)}{r_{max}^2}\right). \tag{3.28}$$

In the case of n particles the dose delivered on the reference point P is the sum of n independent and identically distributed tracks. The cumulative distribution function can be, therefore, calculated convolving $F_1(d)$ n times:

$$F_n(d) = \underbrace{F_1(d) * ... * F_1(d)}_{n \quad \text{times}} \tag{3.29}$$

The probability frequency $f(d)$ is the derivate of $F_n(d)$ and the heavy charged particle response can be obtained as the expected local response

$$S_{HI} = \langle s \rangle = \int_0^{d_{max}} S_X(d) f(d) \mathrm{d}d \tag{3.30}$$

The relative effectiveness can be, therefore, calculated according with Eq. 3.3 as

$$\eta = \frac{S_{HI}}{S_X(D)} = \frac{\langle s \rangle}{S_X \langle d \rangle} \tag{3.31}$$

where $\langle d \rangle$ is the average dose delivered on a generic point of the detector when irradiating with a dose D of low-LET radiation.

The main advantage of this algorithm is that the convolution can be performed using an approximated method introduced by Kellerer, which make the calculation faster with respect to the grid summation approach proposed by Geiss [2] and Monte Carlo simulations.

The CPP-SC is included in an open source computational library for amorphous track modeling called libamtrack [51][1]. Besides the CPP-SC , an implementation of the Katz ion/gamma kill (IGK) model and a grid summation algorithm (GSM), inspired on ECLaT, are provided. Furthermore various radial dose distribution model, stopping power tables and several predefined photon response curve are implemented. Presently the compound Poisson processes method has been applied to the study of cell survival by Grzanka [52] and for alanine detector by Herrmann [33].

[1] http://libamtrack.dkfz.de

Chapter 4

Detector efficiency calculations: implementations

After introducing several theoretical models with the aim of describing the response of TLDs irradiated with heavy charged particles, in this chapter we present two different approaches for TLDs efficiency calculations, based on the local effect model (LEM). At first we will describe the ECLaT software which has been developed by Geiss at GSI [2] [53]. This is a simple algorithm capable of calculating TLD efficiencies, together with their dependence on ion charge Z and energy E. The effectiveness values, computed by ECLaT, correctly describes experimental data but relies on some *ad hoc* prescriptions which are not completely justified from a theoretically point of view.

For this reason a new, simple analytical approach has been developed by the author of this work, the Single Ion approach, where the detector response is evaluated starting from the response of a single ion of the beam. In the following sections this method will be accurately described and its limits of validity will be analyzed. Furthermore, the robustness of the Single Ion approach against modifications of the radial dose distribution, as well as modifications of the detector response models, will be critically evaluated.

The computed values of the efficiency will be compared with experimental data as well as to other calculated values provided by different approaches. Moreover, the results of our model have been implemented in the treatment planning code TRiP98 [54] in order to perform signal calculations on a macroscopic target, irradiated with an extended carbon ion field. These results will also be presented and compared with experimental data at the end of this chapter.

4.1 ECLaT

ECLaT (efficiency calculation for all thermoluminescent detectors) is an algorithm based on a "LEM-like" model (Local Effect Model) for the calculation of the relative effectiveness of TLDs developed by Geiss at GSI [2] [53]. This model has been well received thanks to the good agreement with the experimental data and thanks to its simplicity. However, some issues were pointed out by N.Bassler in his PhD thesis [39]. In this section we are going to briefly describe the ECLaT approach and we are going to give an overview of the unsolved issues.

4.1.1 Description of ECLaT

This program computes the relative effectiveness of TLDs (see equation 3.3), as a function of the ion type Z, and energy E, starting from two main ingredients:

- a parametrization of the dosimeter low-LET radiation response curves;
- a model of the radial dose distribution $D(r)$.

The former has been obtained by the following parametrization of the experimental data of Majborn [55] [56](Figure 4.1)

$$TL_X(D) = c \times \left[a\left(1 - e^{-b_1 \cdot D}\right) + (1-a)\left(1 - e^{-b_2 \cdot D^2}\right)\right] \tag{4.1}$$

with a, b_1, b_2 fitting parameters and c arbitrary constant.

The radial dose distribution as a function of the distance from the ion path r is instead given by the simple formulation (similar to the one used in LEM) Eq. 3.25:

$$D(r) = \begin{cases} k & \text{if} \quad r \leq a_0 \\ k(a_0/r)^2 & \text{if} \quad a_0 < r < r_{max} \\ 0 & \text{if} \quad r_{max} < r \end{cases} \tag{4.2}$$

where k is a normalization factor, a_0 is the size of the track core and r_{max} is the maximum range of secondary electrons. The value of a_0 is kept fixed and it is of the same order of magnitude of the crystal lattice spacing ($a_0 \approx 1\mathring{A}$). The value of r_{max} depends on the energy of the primary ion (E). It is based on Monte Carlo calculations, after accounting for the maximum energy that an ion can transfer to an electron (classic kinematic value) and it can be parametrized as

$$r_{max} = (4 \times 10^{-5} E^{-3/2})\rho^{-1}, \tag{4.3}$$

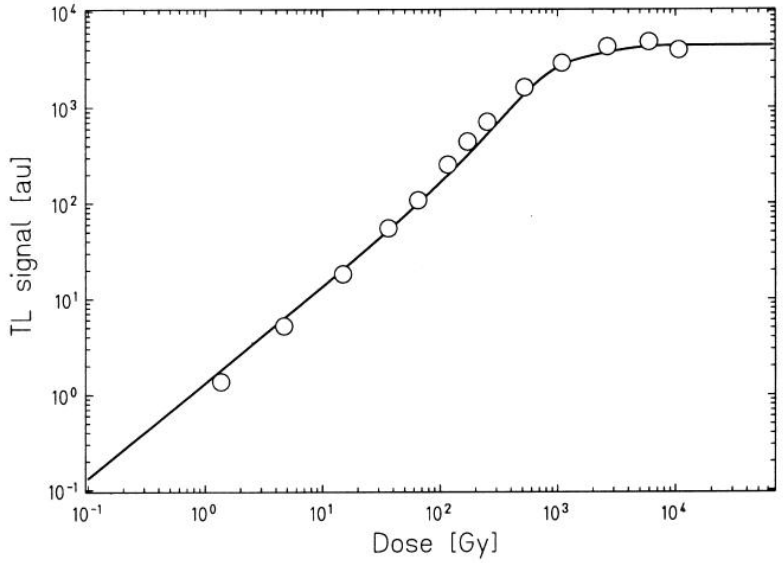

FIGURE 4.1: TL response as a function of the dose for low-LET radiation. The experimental data (∘) are taken form [55], the parametrization used (equation 4.1) is shown as a solid line. Figure from [56].

where ρ is the detector density in g/cm^3 and E is expressed in MeV/u. This parametrization is equal in form to the one used in LEM, Eq. 3.26, but with different numerical constants. The normalization factor k in Eq. 4.2 is given by:

$$k = C \times \frac{1}{2\pi\rho}\left(\frac{dE}{dx}\right)\left[\frac{1}{2} + \ln\left(\frac{r}{r_0}\right)\right]^{-1}\frac{1}{r_0^2} \qquad . \tag{4.4}$$

This is obtained by requiring that the entire dose deposited by a single particle is distributed over its track.

$$2\pi\cdot\int_0^{r_{max}} D(r)rdr = \frac{1}{\rho}\left(\frac{dE}{dx}\right). \tag{4.5}$$

The factor $C = 1.602 \times 10^{-10}$ in Eq. 4.4 is the conversion factor from MeV/g to Gy, since $\frac{dE}{dx}$ is usually express in MeV/cm .

With the definitions for the radial dose distribution and TL response given above the relative effectiveness, calculated at fixed dose D, is defined as [2]

$$\eta_{HI,\gamma} = \left.\frac{(S_{HI}(D)/D)}{(S_X(D)/D)}\right|_D \tag{4.6}$$

where $S_{HI}(D)$ is the signal produced from the detector following heavy charged particle irradiation and $S_X(D)$ is the signal produced by a low-LET reference radiation. To compute $\eta_{HI,\gamma}$, it is thus necessary to know both $S_{HI}(D)$ and $S_X(D)$. The computation of these quantities proceeds along the following steps and is schematically represented in Figure 4.2:

$S_{HI}(D)$

1. divide the TLD in slices;
2. on each slice, select an appropriate simulation area;
3. simulate on each area the passage of ions;
4. sample the area in voxels, *i.e.* areal pixels times the slice thickness;
5. compute the dose delivered by the ions on each voxel;
6. compute the detector signal for each voxel;
7. sum the contribution of all the voxels, areas, slices.

$S_X(D)$

1. compute the total dose delivered to the detector;
2. compute the signal following low-LET radiation.

Computation of $S_{HI}(D)$.
At first the detector is divided in slices orthogonal to the direction of the incoming beam. The slice thickness for each slice Δz is chosen so that the energy deposited on each slice is constant within 10%. In order to compute the energy loss in each detector slab, the algorithm makes use of stopping power tables for LiF material which are calculated with the code ATIMA [57]. For reference, in the original ECLaT code the thickness of the detector was 0.038cm.

Assuming a uniform distribution of the ion incidences on the detector surface, it is possible to restrict the simulation to a small area. The latter, noted as A_{Sim}, is computed as a function of the beam fluence ϕ as

$$A_{Sim} = n_{HI}/\phi \tag{4.7}$$

by requiring that, on average, the number of ions passing through the simulation surface should be $n_{HI} = 9$. The n_{HI} can be placed on the simulation area in one of two possible ways: they can be randomly distributed or placed on a regular grid.

In order to compute the detector signal, each simulation area is sampled in a grid with at least 10×10 voxels. The dose deposited by the n_{HI} ions on each voxel, ΔD_i

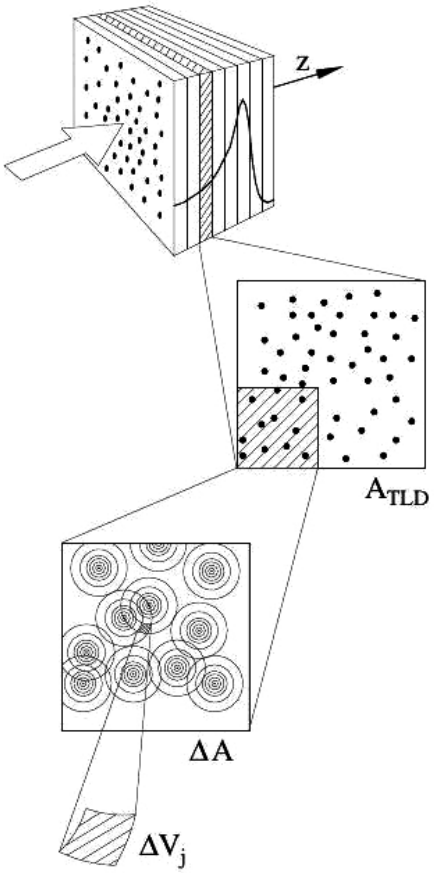

FIGURE 4.2: Schematic representation of ECLaT.

is computed using Eq. 4.2 and the detector signal for each volume element, $S_{HI,i}$ is calculated following Eq. 4.1

$$S_{HI,i}(\Delta D_i) = TL_X(\Delta D_i) \times V_{voxel} \tag{4.8}$$

where V_{voxel} is the voxel volume.

The signal of each simulation area is given by the sum of the contributions of all the voxels. Furthermore, the whole dosimeter signal can be computed normalizing the signal given from each simulation area to the slice surface and summing up these contributions for all the slices. The total dose delivered on the detector by the ion beam is calculated in analogous way.

Computation of $S_X(D)$.

In order to compute the signal produced by low-LET radiations, the total dose deposited by the ion beam of energy E, charge Z and fluence ϕ is calculated according to Eq. 1.16 as:

$$D_{tot} = \phi \times \frac{1}{\rho}\left(\frac{\Delta E}{\Delta Z}\right). \tag{4.9}$$

Here ΔZ is the thickness of the detector if the particles are so energetic that they can pass through the dosimeter; otherwise, if the particles are stopped inside the detector, ΔZ is the particles' range. ΔE is the total energy deposited on the TLD.

The detector signal given by a dose D_{tot} of low-LET radiation is computed assuming an uniform distribution of the dose within the whole detector and is given by:

$$S_X(D_{tot}) = TL_X(D_{tot}) \times V_{TLD} \tag{4.10}$$

where V_{TLD} is the volume of the detector.

In Figure 4.3 a comparison between the experimental data from Geiss [2] and efficiency curves calculated by ECLaT is shown.

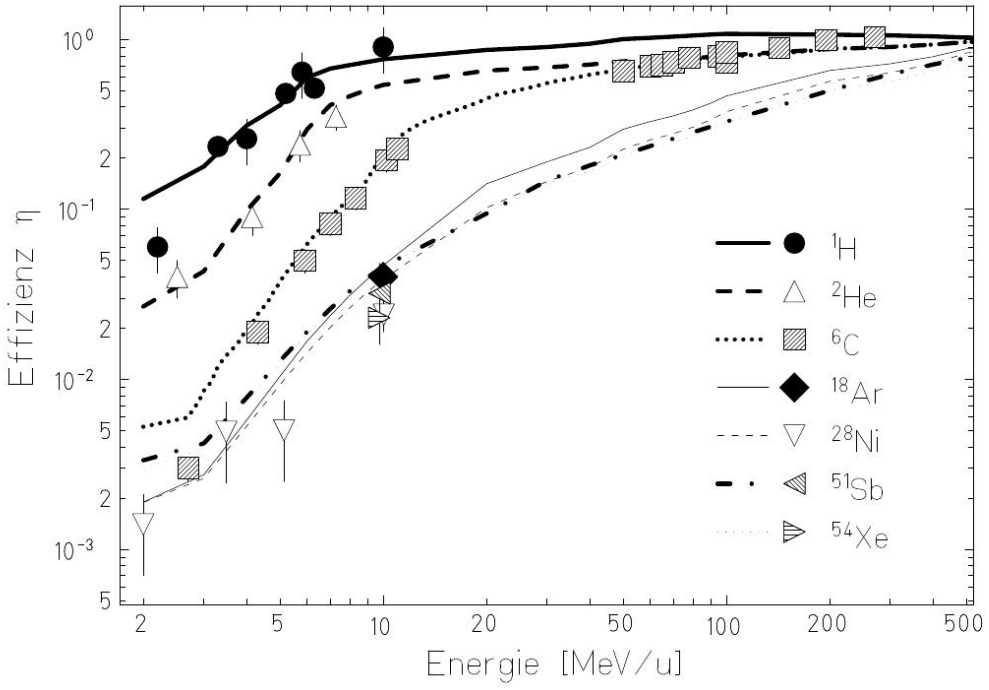

FIGURE 4.3: Relative effectiveness of TLD-700 as a function of the energy. Comparison between experimental data (symbols) and calculated values (lines). Figure from [2].

4.1.2 Limits of ECLaT

As reported in the PhD thesis of N.Bassler [39] there were some issues in the original code, most of which were successfully corrected by N.Bassler. However two main inconsistencies still persist: first, the effectiveness values are rescaled *ad hoc* to ensure that

they are bound between zero and one; second, the computation of the radial dose distribution as implemented in the code, differs from the one of Geiss [2] by a multiplicative constant.

Effectiveness normalization . The radial dose distribution around the ion trajectory becomes broader as the energy of the incident particle is increased: the maximum radius of secondary electrons increases according to Eq. 4.3 and the dose in the track core decreases (the normalization factor k decreases, Eq. 4.4). For very high energy, therefore, the dose distribution due to ion irradiation approaches the one following low-LET irradiation and the relative effectiveness should tend to the unity.
This condition is enforced in the code by imposing that, for energy values larger than $E = 10^4$ MeV/u, the relative effectiveness be equal to unity, rescaling the whole curve accordingly. As mentioned above, this normalization should not be required, as it should naturally arise from the physics of the model. However, when removing it, the relative effectiveness for very high energies reaches values in excess of 10^7 and this represents a lack of robustness of the program.

Radial dose distribution Another inconsistency was found in the source code: the expression for computing the radial dose distribution, as implemented in ECLaT code, is 5×10^4 times larger than the theoretically predicted one (Eq. 4.2), as shown in Figure 4.4. In particular the conversion factor C from MeV/g to Gy in Eq. 4.4 implemented on ECLaT is 9×10^{-6} instead of 1.602×10^{-10}. The motivation for the use of this conversion factor in the original code is still not clear. Substituting the theoretically correct

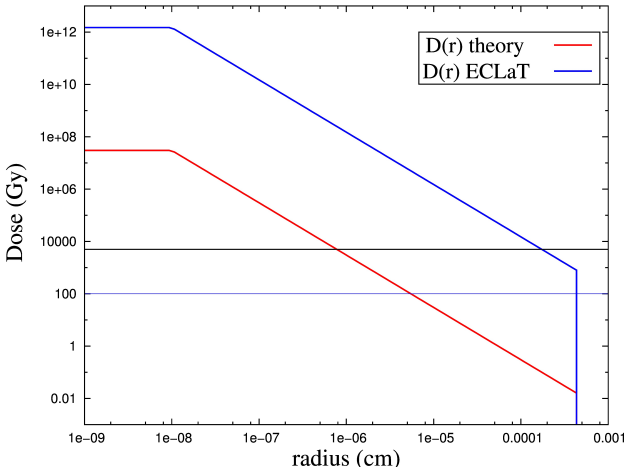

FIGURE 4.4: Comparison between the radial dose distribution used in ECLaT (in blue) and the radial dose distribution obtained from equation 4.2 with the normalization factor, k, calculated from 4.5 (in red) for 10 MeV carbon ion. The two horizontal lines represent the two dose levels above which supra-linear and saturated effects appear, see Figure 3.2.

conversion factor in the code a new problem appears: the dose distribution within the detector is undersampled. That distribution, as explained in the previous section, is computed sampling the simulation areas with a grid of 10×10 voxels. However this sampling is too coarse for narrow distributions, such as the radial dose distributions around ion tracks. This results in an underestimation of the dose delivered on the detector. The red curve in Figure 4.5 shows the results of effectiveness calculations using the theoretically correct radial dose distribution, compared with the experimental data from [2].

A possible solution is to make the grid more fine-meshed, but this would tremendously increase the computing time. E.g., Using a grid of 1000×1000 voxels the computing time increases by a factor of 10000 [39]. A modified version of ECLaT using a grid size of 1000×1000 and the theoretically correct radial dose distribution has been developed. Unfortunately the results are not satisfactory: it needs a week of computing time and the dose distribution is still undersampled (blue curve in Figure4.5).

Although the ECLaT efficiency curves are in good agreement with the data, the two problems detailed above, especially the one related to the sampling of the radial dose distribution, are not easily solvable. This may limit the robustness of the method. For this reason, different approaches to the calculation of the efficiencies of TLDs have been investigated in this work.

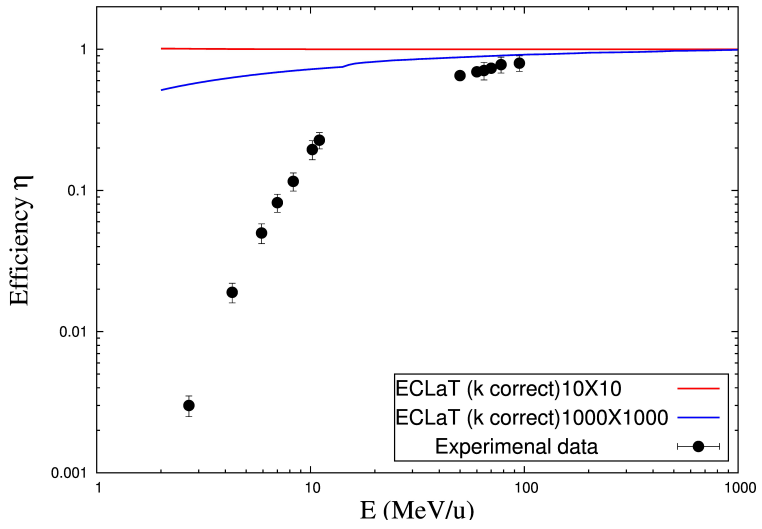

FIGURE 4.5: Effectiveness calculation using the theoretically correct radial dose distribution compared with experimental data from [2]. In red a sampling grid of size 10×10 has been used whereas the blue curve was obtained using 1000×1000 grid.

4.2 Single Ion approach

4.2.1 Description of the Single Ion approach

The Single Ion approach represents a basically analytical method to calculate the relative effectiveness of TL detectors according to Eq. 3.3. This model assumes that each ion contributes to the TLD response independently; thus, the detector signal after ion irradiation can be calculated by summing up the signal of all the individual ions. As ECLaT, this approach requires in input the knowledge of the radial dose distribution $D(r)$ and a parametrization of the low-LET dose-response curve for the dosimeter, $TL(D)$. The low-LET response and the radial dose distribution adopted are the same ones that are implemented in ECLaT (Eq. 4.1 and Eq. 4.2 respectively).

The main idea is to fold the radial dose distribution of a single particle with the detector low-LET dose-response curve, thus obtaining the TL radial distribution of a single ion, $TL(D(r))$, as shown in Figure 4.6. The signal generated by a single ion (S_{HI}) can be calculated by the integration of the TL radial distribution over the ion track. The relative effectiveness can be calculated, thus avoiding the sampling of the radial dose distribution. This represents a great advantage with respect to ECLaT, in which the problem of undersampling is one of the main limitations.

In order to calculate the relative effectiveness for a particle beam of given energy E, atomic number Z and fluence ϕ a simple algorithm has been developed. The relative efficiency at a fixed dose, D, is calculated, according to Eq. 3.3, as

$$\eta_{HI,\gamma} = \left.\frac{S_{HI}(D)}{S_X(D)}\right|_D, \tag{4.11}$$

where S_X is the TL signal given by a dose D of low-LET radiation. The computation of the two quantities $S_{HI}(D)$ and $S_X(D)$ is described below.

Computation of S_{HI} .
In analogy with the ECLaT program, the algorithm begins by dividing the detector into slices normal to the incident particle direction. The slice thickness Δz_i is chosen so that the energy variation of the primary ion inside the layer is constant within 1%. This differs from ECLaT, where a 10% margin was used. In order to calculate the energy loss in each detector slice, the algorithm makes use of stopping power tables calculated with the radiation transport code ATIMA [57].

For each slice (Δz_i) the TL radial distribution around a single ion, $TL_X(D_i(r))$, is calculated. As mentioned above, the signal produced by the ion on the i-th slice can be

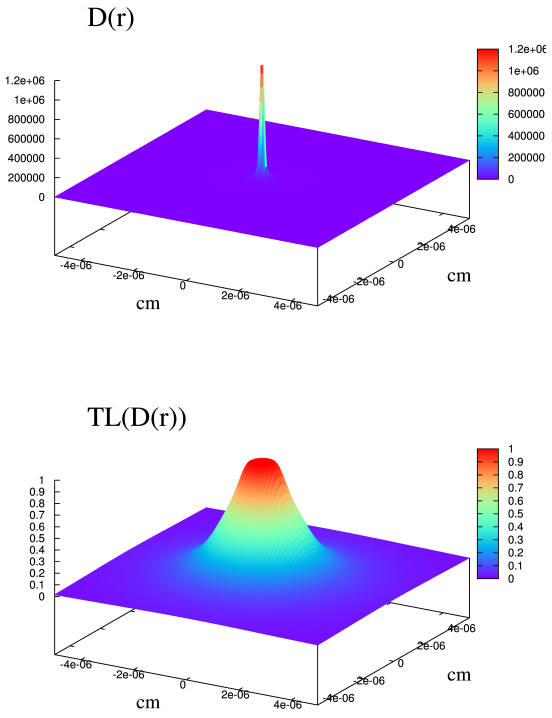

FIGURE 4.6: Radial dose distribution, D(r), (on the top) and TL response distribution, TL(D(r)), (on the bottom) around a single ion.

computed as

$$S_{HI_i} = 2\pi\Delta z_i \int_0^{r_{max_i}} TL_X(D_i(r))rdr, \tag{4.12}$$

where r_{max_i} is the maximum radius of secondary electrons. To obtain the signal S_{HI} produced by a single ion, the signal of all the slices is summed up:

$$S_{HI} = \sum_{i=0}^{\#\text{slices}} S_{HI_i}. \tag{4.13}$$

It is important to notice that, for the particular functional forms of $TL_X(D)$ and of $D_i(r)$ considered in this work, the integral for the calculation of S_{HI_i}, Eq. 4.12, can be solved analytically. Moreover, since we do not sample the radial dose distribution directly, but rather its image through the response function $TL_X(D)$, we are left with a smoother and broader quantity on which the sampling is much more effective (see Figure 4.6). This is extremely important when using numerical rather than analytical methods to compute S_{HI_i}, as it may become necessary for future developments and refinements of the model.

Computation of S_X .

As in ECLaT, the total dose deposited by the ion beam of energy E, charge Z and

fluence ϕ is calculated according to Eq. 1.16 as:

$$D_{tot} = \phi \times \frac{1}{\rho} \left(\frac{\Delta E}{\Delta Z} \right). \tag{4.14}$$

Here ΔZ is the thickness of the detector, if the particles are so energetic that they can cross the dosimeter; otherwise, if the particles are stopped inside the detector, ΔZ is the particles' range. ΔE is the total energy deposited on the TLD.

The signal S_X is computed on a small area which is defined as the area in which, on average, one ion is found. Similar to the definition given in Eq. 4.7, this area is computed as a function of the beam fluence ϕ as:

$$A_{Sim} = 1/\phi. \tag{4.15}$$

Thus, in analogy with the ECLaT computation Eq. 4.10, the signal S_X is given by

$$S_X(D_{tot}) = TL_X(D_{tot}) \times A_{sim} \times \Delta L, \tag{4.16}$$

where ΔL is the detector thickness.

In Figure 4.7 and 4.8 a comparison between the calculation with the single ion approach and experimental data [56] for different ions is shown. These results will be critically discussed in the following sections.

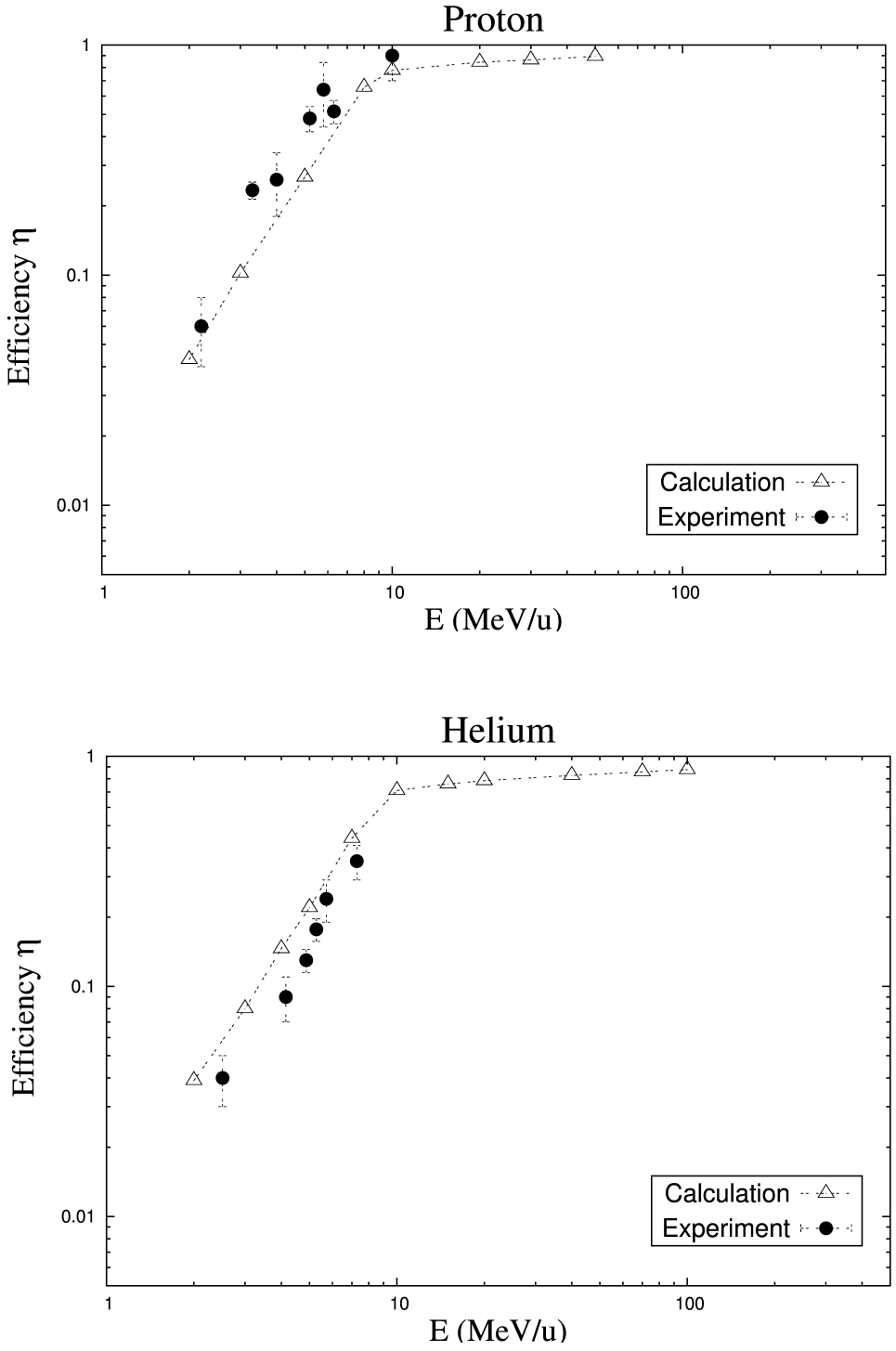

FIGURE 4.7: (see caption on next page)

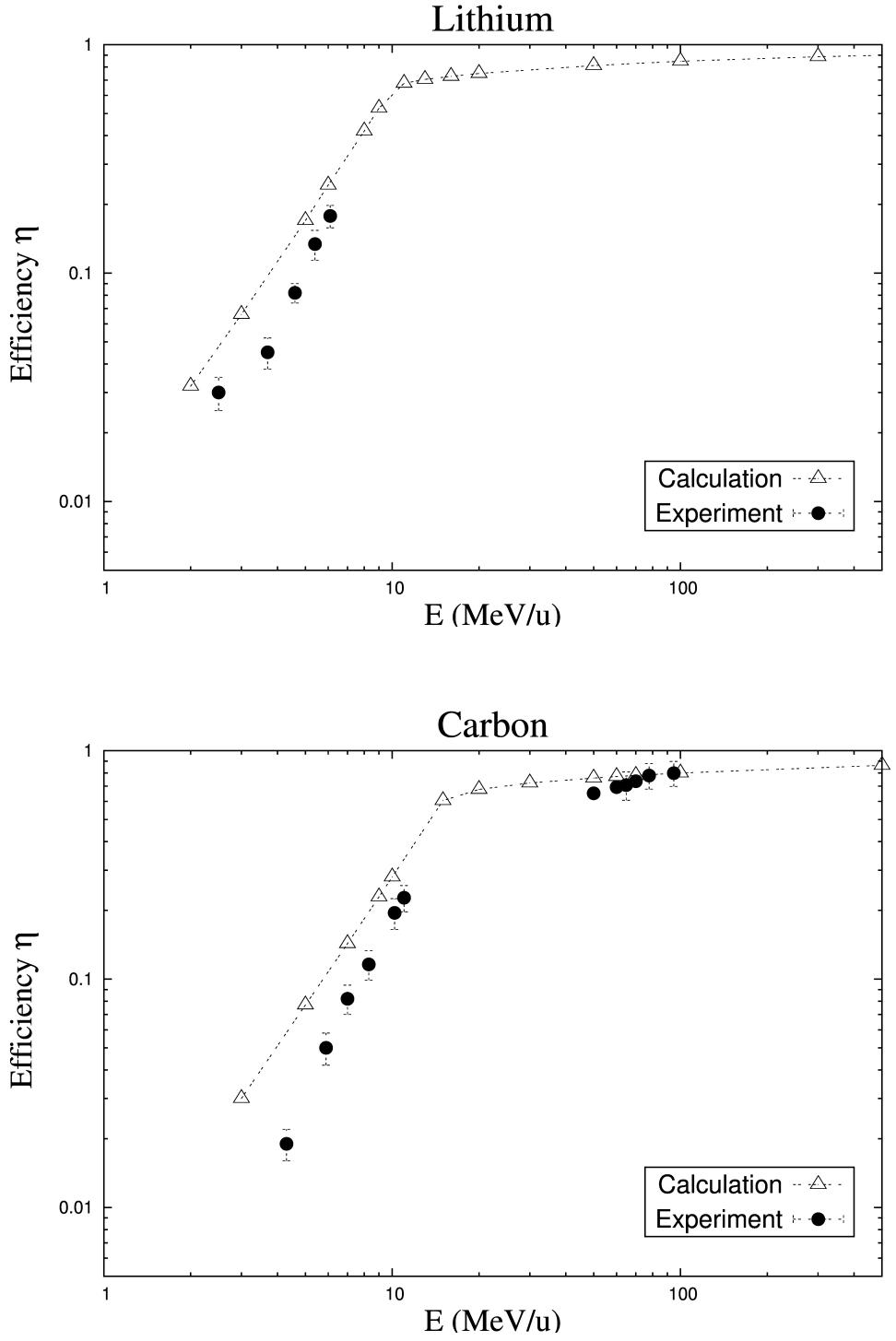

FIGURE 4.8: Single ion efficiency calculations for TLD-700 (empty triangle) compared with experimental results [56](full circle) for various ions. The fluence is $10^7 \mathrm{cm}^{-2}$.

TABLE 4.1: Single Ion calculation compared with Geiss experimental data [56].

Ion	Energy [MeV/u]	Efficiency η Experiments (Geiss 1998)	Single Ion calculation
H	2.2	0.06 ± 0.02	0.05 ± 0.01
	3.3	0.23 ± 0.02	0.12 ± 0.01
	4.0	0.26 ± 0.08	0.18 ± 0.01
	5.2	0.48 ± 0.06	0.3 ± 0.01
	5.8	0.64 ± 0.2	0.37 ± 0.01
	6.3	0.515 ± 0.06	0.43 ± 0.01
	10.0	0.9 ± 0.2	0.78 ± 0.01
He	2.5	0.04 ± 0.01	0.06 ± 0.01
	4.2	0.09 ± 0.02	0.16 ± 0.01
	4.87	0.13 ± 0.02	0.22 ± 0.01
	5.3	0.18 ± 0.02	0.26 ± 0.01
	5.7	0.24 ± 0.05	0.30 ± 0.01
	7.3	0.35 ± 0.07	0.48 ± 0.01
Li	2.5	0.03 ± 0.005	0.04 ± 0.01
	3.7	0.045 ± 0.007	0.08 ± 0.01
	4.6	0.082 ± 0.008	0.12 ± 0.01
	5.4	0.134 ± 0.02	0.17 ± 0.01
	6.1	0.178 ± 0.02	0.22 ± 0.01
C	4.3	0.019 ± 0.003	0.06 ± 0.01
	5.9	0.050 ± 0.008	0.11 ± 0.01
	7.0	0.082 ± 0.012	0.14 ± 0.01
	8.3	0.116 ± 0.017	0.2 ± 0.01
	10.2	0.195 ± 0.03	0.29 ± 0.01
	11.0	0.227 ± 0.03	0.33 ± 0.01
	50.0	0.651 ± 0.02	0.76 ± 0.01
	60.0	0.693 ± 0.02	0.77 ± 0.01
	64.8	0.707 ± 0.1	0.77 ± 0.01
	70.0	0.735 ± 0.02	0.78 ± 0.01
	77.8	0.779 ± 0.1	0.78 ± 0.01
	94.8	0.798 ± 0.1	0.79 ± 0.01

4.2.2 Discussion

As specified in the previous section, the Single Ion approach assumes that each ion contributes independently to the detector response. This condition is not always satisfied, thus restricting the validity range of the model. We are going to discuss the limitations arising from this issue in the following sections. However, despite these restrictions, the simplicity of the model makes possible to systematically study its robustness against changes in the input parameterizations. These include the use of different gamma response parameterizations, of different stopping power tables and different submodels, and corresponding parameters of the track core radius. Before discussing on these effects, we need to make some considerations about the experimental data against which the model was compared.

4.2.2.1 Considerations on the experimental data

In literature, several experimental data for the effectiveness are available. However, in this work we will always compare the efficiency calculations with Geiss measurements [2]. Indeed, often the experimental procedures are reported with omissions: the fluence values are not specified [58][59], or the thickness of the detector is not reported [59]. In other cases, the relative effectiveness is measured only for specific peaks of the detector glow curve [25] [59]. Furthermore, even in the works in which all these parameters are reported, it is often difficult to find data sets with enough efficiency values for different ion species. This is for example the case in the recent work of Gieszczyk [60], were only one or two efficiency values per ion are reported.

By comparing efficiency data from different authors, one can notice a general trend of decreasing efficiency as the LET values increase above approximately $10^2 - 10^3$ MeVcm^2/g (we report in Figure 4.9 a compilation of experimental data for the efficiency of TLDs). However, for any given LET value, the measured efficiencies do not agree among the different authors, making it difficult to pin down a single value to compare with our model. For example, considering 100 MeVcm^2/g protons, efficiency values between 0.4 and 0.85 are found. Furthermore, Ávila et al. [61] raised some doubts about Geiß's data, which show a behavior that goes against the general trend of the other authors.

There are many factors that can justify this differences in the values of efficiency measurements (Ávila et al.[61]), such as variations in impurity concentrations in detectors coming from different batches, varying in annealing procedures, post-annealing cooling, glow curve heating rate and TL-light self absorption.

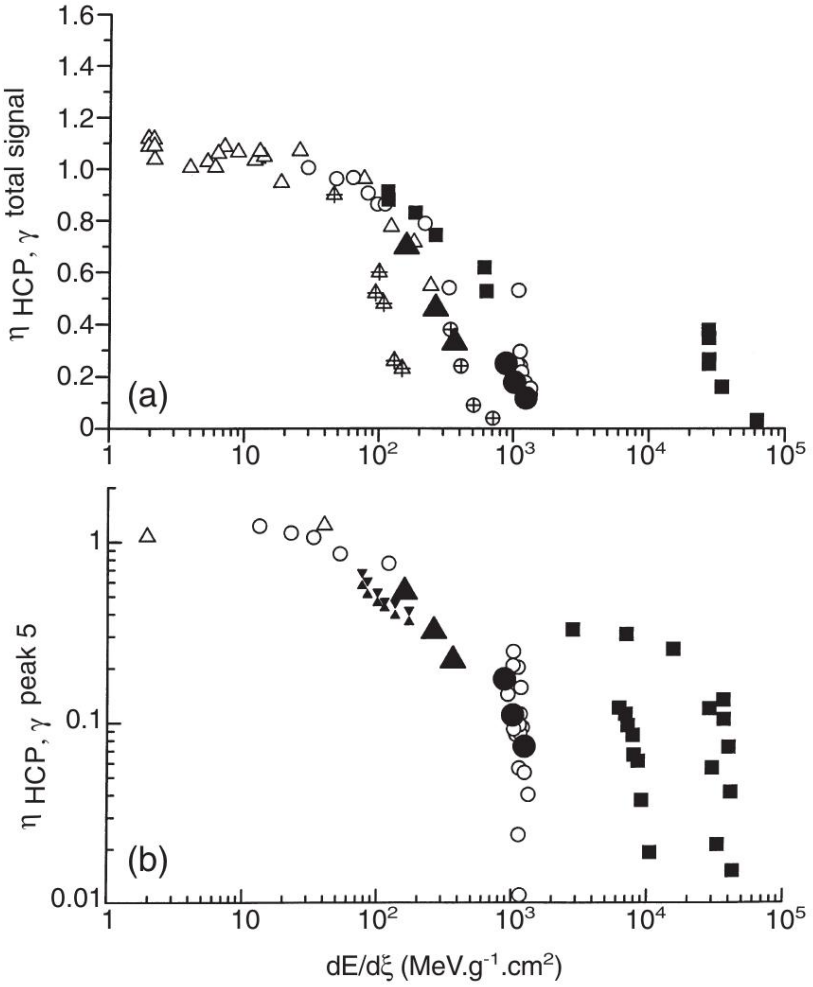

FIGURE 4.9: Relative TL efficiency with respect to ^{60}Co for the total signal upper and for peak 5 lower in LiF:Mg,Ti for several heavy charged particles as a function of mass stopping power: protons(triangles), helium (circles) and heavier ions (squares). Data from Geiss [2] are included and are represented by crossed symbols. Figure from [61]. The errors are not reported but are of the order of 10%.

In order to quantify the influence of experimental factor Ávila et al. [61] measured the relative effectiveness $\eta_{p,\gamma}$ for protons of 3 MeV with respect to ^{60}Co with TLD-100 varying the batch, the geometry of the detector, the annealing procedures and using different reader device. It was found that the use of different experimental procedures leads to values of $\eta_{p,\gamma}$ that vary between 0.44 ± 0.01 and 0.79 ± 0.08 for the total signal and from 0.36 ± 0.01 to 0.59 ± 0.05 for peak 5. In particular they pointed out that this spread can increase even more if, as in Geiss data, two different procedures are used to measure the two signals: the one given by ions and the one given by the low-LET reference radiation.

However, as observed by Bassler [39], there are many other factors that can lead to such a spread in the efficiency values. For example the TL light self-absorption in thick

detectors is not, in general, taken into account and in many case the fluence value is not reported. Furthermore, the way in which the energy deposition within the detector is calculated may change the result of the efficiency calculation. Indeed, in some papers the energy deposition is calculated assuming that the particle comes to a complete stop within the detector. In others, notably [2], the finite thickness of the detector is taken into account and consequently the possibility that the particle may cross the detector.

4.2.2.2 Inter-track effect

Since the TL response is linear in dose only for doses lower than D_{sup} (for TLD-700 D_{sup} is about 100 Gy), the ion contributions to the detector response are independent only when the tracks of different ions are not overlapping. Even when overlaps occur, the total dose delivered in the inter-track region is considered to be in the linear regime (*i.e.* it must be less than D_{sup}).
Inside the code the signal given by the ion, S_{HI}, and the total dose, D_{ion}, are calculated on the whole track size while the signal given by the reference radiation is normalized to the simulation area. This is certainly correct when the track of the ion is entirely included inside the simulation area, *i.e.* when the tracks of different ions are not overlapping. However, when the radial dose distribution around the ion trajectory exceeds the the simulation area A_{Sim}, it can be assumed that the dose delivered outside A_{Sim} is, on average, equal to the dose deposited by neighbor ions on the simulation area, as shown in Figure 4.10. Therefore, if the dose delivered in the overlap region is in the linear regime of the TL-response, the single ion approach can still be considered valid. Nevertheless, in this section the limitations due to the inter-track overlap will be discussed.

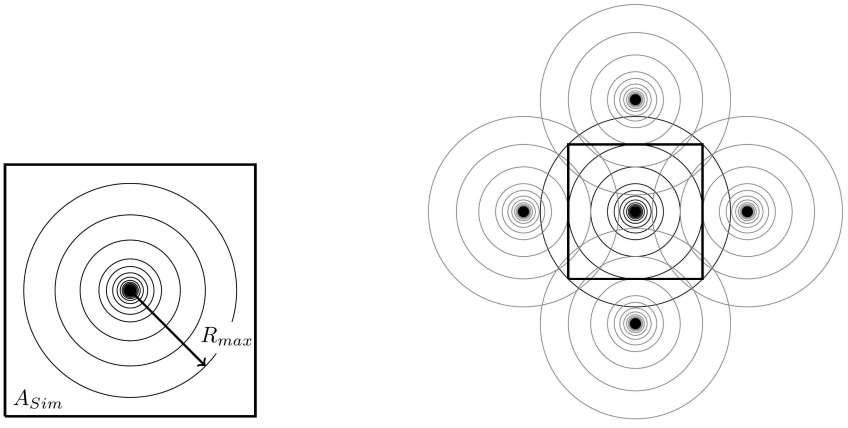

(a) (b)

FIGURE 4.10

The overlap probability depends on the average distance between ions and on the size of the tracks. As shown in Figure 4.11, the first one is determined by the fluence while the

latter depends on the maximum range of secondary electrons (and thus from the energy of primary ions, Eq. 4.3). For example, considering a beam with a fluence $\phi = 10^7$ cm^{-2}, the mean distance between two particles is $\sqrt{\frac{1}{\phi}} = 3.16 \times 10^{-4}$ cm . On average, the overlap between tracks occurs when the radius of the tracks is larger than half of the mean distance $\left(r_{max} > \frac{1}{2}\sqrt{\frac{1}{\phi}} = 1.58 \times 10^{-4} \text{ cm}\right)$, which corresponds to an energy of primary ions larger than 4.77 MeV/u.

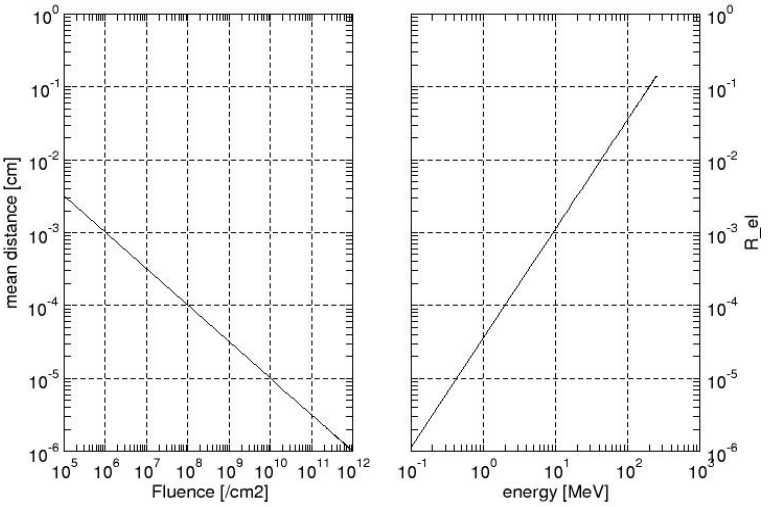

FIGURE 4.11: The variation of the mean distance between ions with the fluence is reported on the left. The dependence of the maximum radius of secondary electrons from the energy of the primary ion is shown on the right.

In order to study this limitation the following procedure will be adopted: the relative effectiveness is computed with the Single Ion approach, at fixed energy, for different fluence values. In Figure 4.12 the efficiency curves for carbon ions of 5 MeV/u, 10 MeV/u and 30 MeV/u are reported for fluence values between 10^4 cm^{-2} and 10^{11} cm^{-2}.

As expected, for relatively low fluences (below 10^8 cm^{-2}), the effectiveness does not change. However, increasing the fluence, the efficiency decreases, reaching a minimum, and then rising again. The beginning of the decrease is associated to the effect of supra-linearity in the inter-track region, where, as already mentioned, the ions can not be considered as independent. The growth of the effectiveness for the very high fluences is, instead, due to the saturation of the TL response for low-LET radiation (S_{HI} does not change with fluence while S_X goes to zero decreasing the simulation area Eq. 4.16).

It is possible to notice that the supra-linear and saturated region of the TL-response appears to be reached at lower fluence values for 5 MeV/u carbon ions. This behavior is counterintuitive since r_{max} grows with energy, thus, at fixed fluence, more overlaps are expected for the more energetic ions. This can be explained by noticing that the radial dose distribution around an highly energetic particle is broader; as a consequence

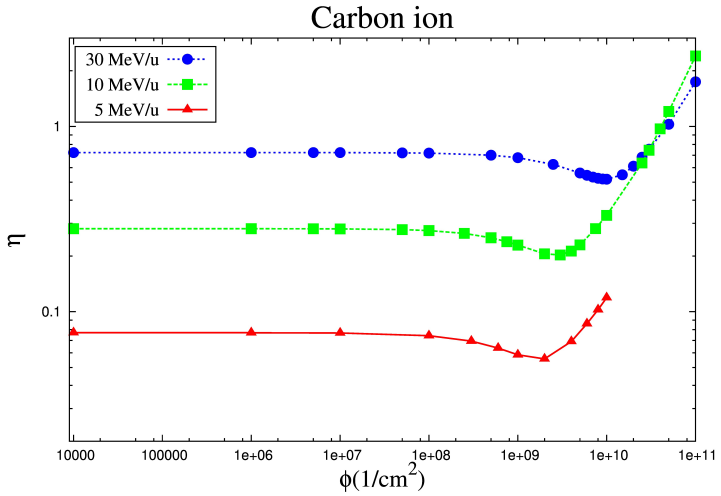

FIGURE 4.12: Relative effectiveness calculation with the single ion approach varying the fluence, for carbon ions of different energies.

the overlaps are large but their dose contribution is small. On the other hand the radial dose distribution around a low energetic particle is extremely narrow, overlaps have a low probability to happen but, when they occur, the dose delivered in the inter-track region is very large.

To better understand this behavior we performed simulations in which, at fixed energy E and fluence ϕ, n_{HI} ions are randomly distributed on the simulation area. This is defined as the area such that $A_{Sim} = n_{HI}/\phi$ and n_{HI} was fixed to be 10^4. In these simulations we estimated the number of ions overlapping with a reference point (fixed in the middle of the area) and the average delivered dose on that point[1]. In the top section of Figure 4.13 and 4.14 the number of overlaps is reported for fluence values between 10^4 and 10^{11} cm^{-2} , for two carbon ions of different energies. The delivered dose in the overlap is reported in the bottom section of the same figures.

By looking at the curve for $\phi = 10^8$ cm^{-2} on the image for 10 MeV/u carbon ions (the turquoise one), we see that on average there are approximately 0.7% ion tracks crossing the reference point. However, looking at the dose, it is possible to notice that the average dose delivered in the inter-track for this value of fluence is lower than 70 Gy. Therefore, even though the number of overlaps on the reference point is quite large, the total dose delivered by all these tracks is still in the linear part of the TL-response.
The supra-linear region is reached, for $E = 10$ MeV/u, for fluences approximately of 10^9 cm^{-2}. Saturation effects on the reference point occur for fluences larger than 10^{10} cm^{-2}, when the average distance between particle is less than 10^{-5} cm and almost all the track are overlapped. on the other hand, for 30 MeV/u carbon ion with fluences of 10^9 cm^{-2} the track are already completely overlapped. However, the dose delivered

[1]We thank N.Bassler for providing a preliminary version of the code used for this test.

on the point of interest is still in the linear region of the TL-response and the total saturation is reached only for fluences larger than 10^{11} cm^{-2}.

From these simulations we thus conclude that the supra-linearity regime is reached earlier for for less energetic ions, in agreement with the results obtained by the Single Ion approach Figure 4.12.

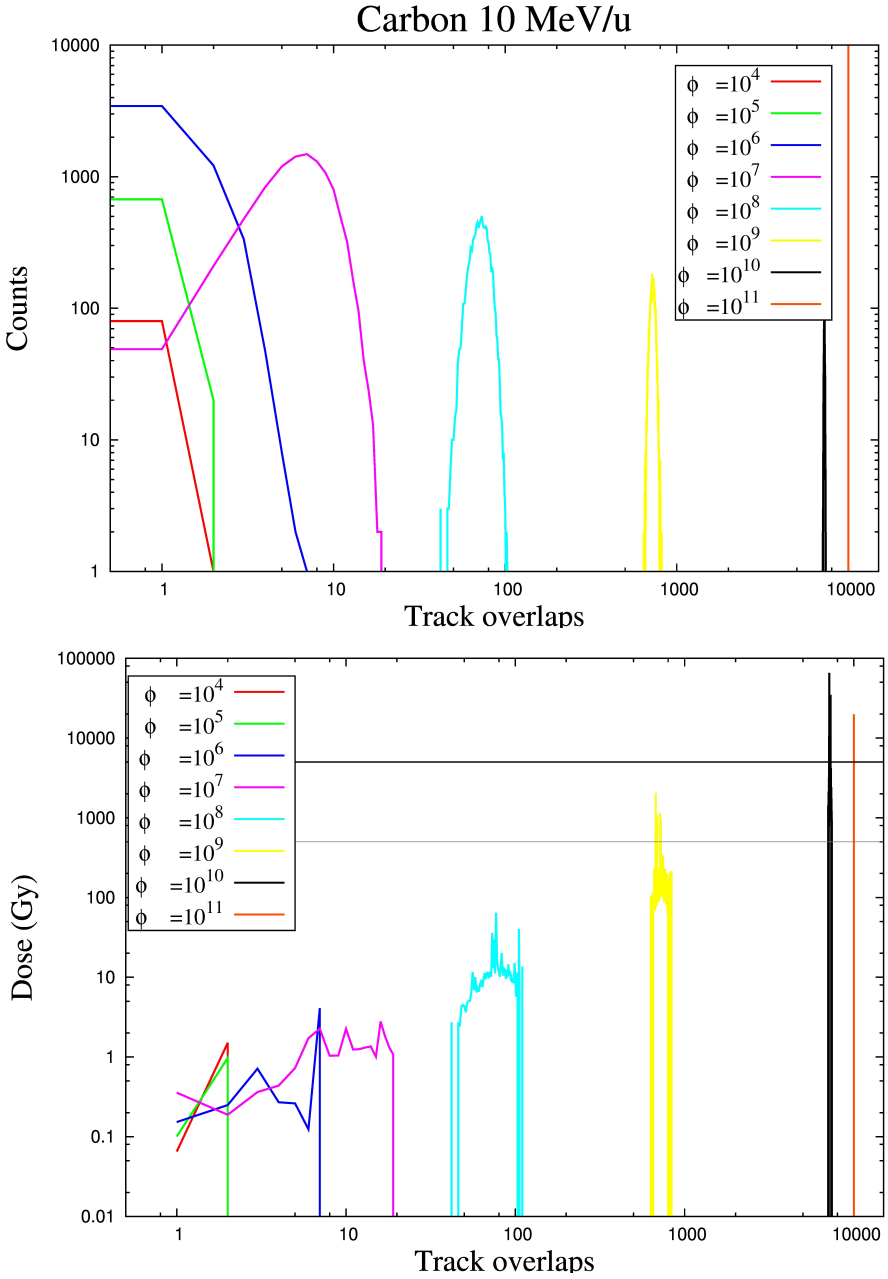

FIGURE 4.13: On the top: the occurrences of the various numbers of overlaps, for carbon ions of 10 MeV/u, for different values of fluence (legend, in cm^{-2}). Due to the logarithmic scale the counts for zero overlap could not be reported. On the bottom: average dose delivered on the point of interest during the overlaps described above. The gray horizontal line represent the dose beyond which the TL-response start to be supra-linear while saturation effects occurs for dose values exceeding the black horizontal line.

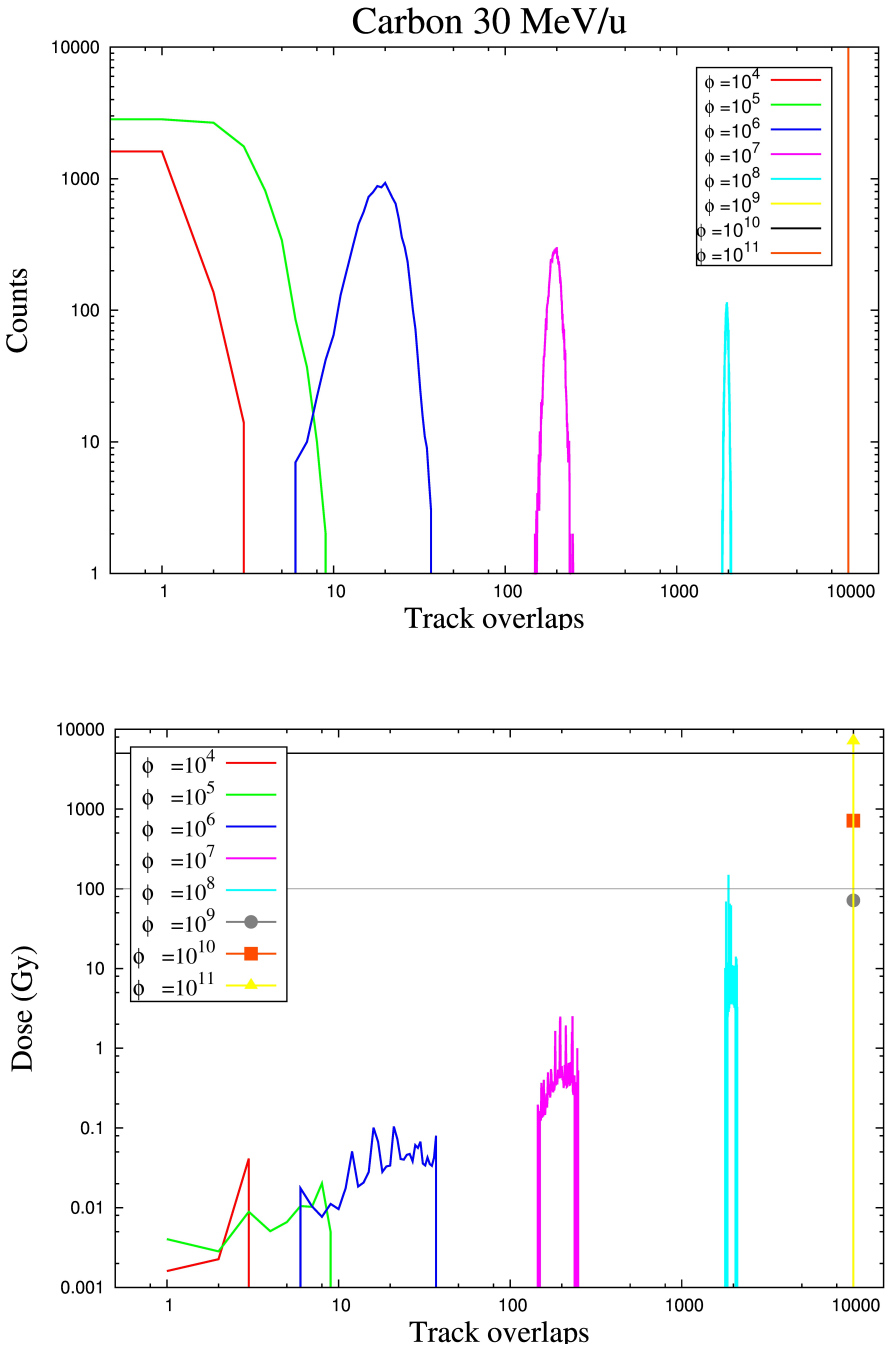

FIGURE 4.14: As Figure 4.13. The curve for $\phi = 10^9$ cm^{-2}, $\phi = 10^9$ cm^{-2}, $\phi = 10^9$ cm^{-2} are superimposed, for these fluence values, indeed, all the track are overlapped. The average dose delivered on the reference point is represented respectively with the gray circle, the orange square and the yellow triangle.

4.2.2.3 Dependence on the low LET response curve

In the Single Ion approach we implemented the same low-LET dose-response curve for the detector proposed by Geiss [2]. This curve is obtained by the following parametrization of Majborn's experimental data [55], Eq. 4.1:

$$TL_X(D) = c \times \left[a\left(1 - e^{-b_1 \cdot D}\right) + (a-1)\left(1 - e^{-b_2 \cdot D^2}\right)\right] \tag{4.17}$$

In his works Geiss suggested two different set of parameters: the first one in his PhD thesis (Geiss 1997) [56] and the second one in his paper (Geiss 1998) [2]. In this work we chose to adopt the first set where:
$a = 0.8$, $b_1 = 3 \times 10^{-4}$, $b_2 = 1 \times 10^{-6}$.
Whereas on Geiss 1998 the parameters proposed are:
$a = 0.59$, $b_1 = 5 \times 10^{-4}$, $b_2 = 2 \times 10^{-6}$.

In Figure 4.15 a comparison between the two different curves is reported while the impact of this difference on efficiency calculations is shown in Figure 4.16. The efficiency values calculated with the parametrization proposed in Geiss 1998 (in blue) are always larger than values calculated with the parametrization proposed in Geiss 1997 (in red). This behavior can be explained by noticing, in Figure 4.15, that the parametrization proposed in Geiss 1998 reproduce with more accuracy the supra-linear behavior and slightly over-estimate it, while the parametrization proposed in Geiss 1997 weight more the linear region under-estimating the supra-linearity.

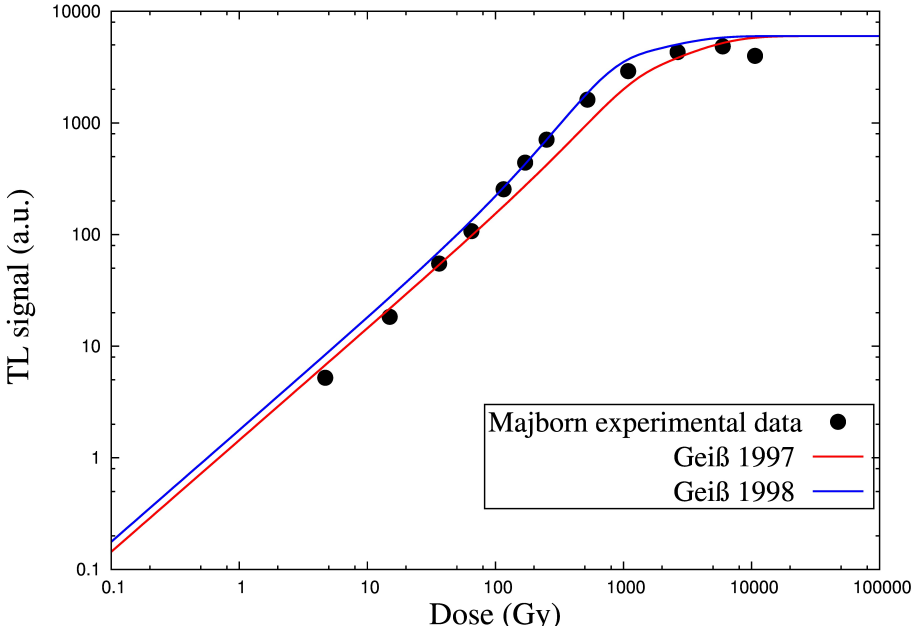

FIGURE 4.15: Comparison between Majborn experimental data[55] and the two parametric curves proposed by Geiss.

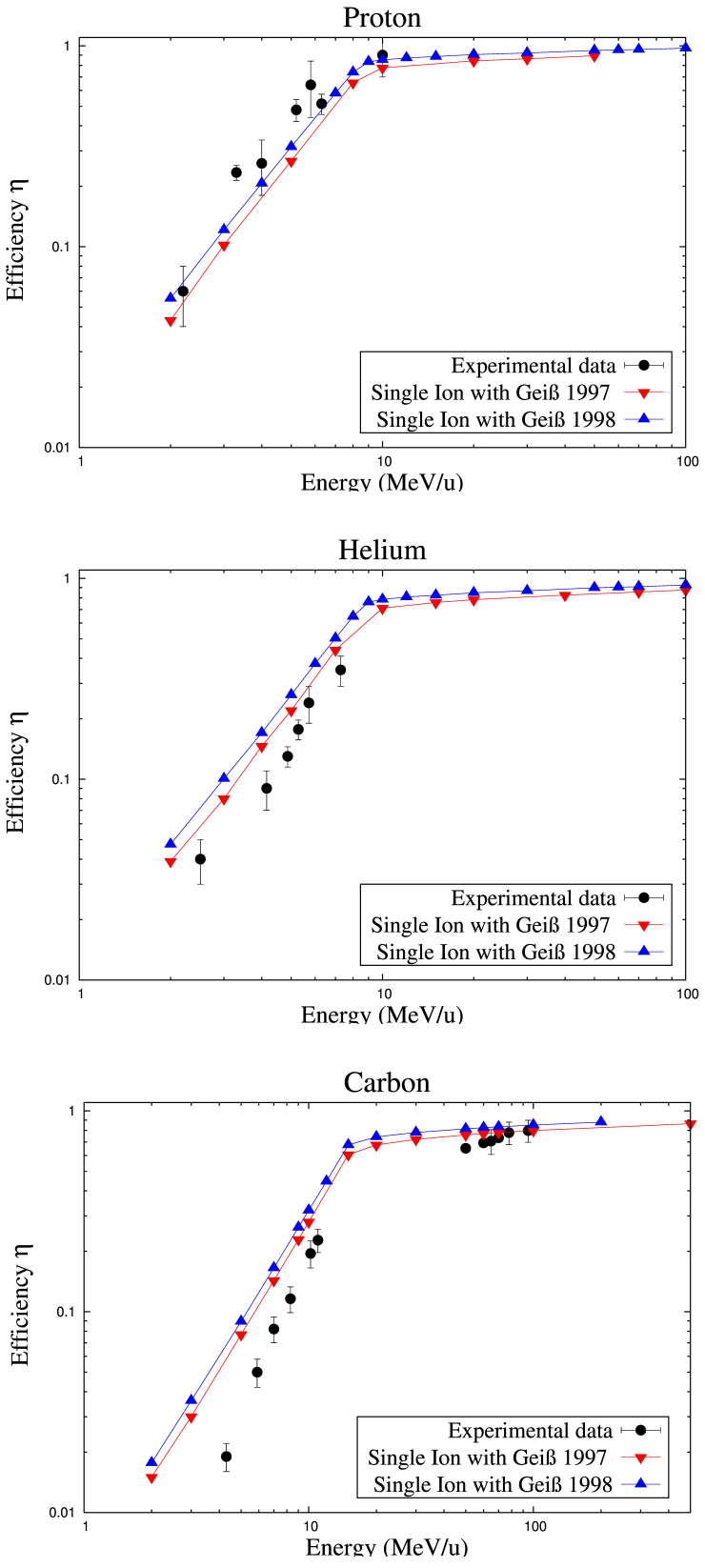

FIGURE 4.16: Comparison between experimental data [2] and efficiency curves calculated with the low-LET response curve proposed in Geiss 1997 (in red), and the one proposed in Geiss 1998 (in blue).

4.2.2.4 Dependence on the radial dose distribution

Besides the parametrization of the low-LET dose response curve, the knowledge of the radial dose distribution around the ion is the other fundamental prerequisite for efficiency calculations with the Single Ion approach.

In analogy with ECLaT, in the Single Ion has been implemented a "LEM-like" radial dose distribution, Eq. 4.2. The latter, as already explained, is assumed to be divided into two region: a core region, which is close to the particle trajectory, and a "penumbra", in which the dose is assumed to drop down by a function $1/r^2$ with the distance from the ion path. In the core region the dose is assumed to be constant and its value , k, is calculated imposing that the entire dose deposited by a single particle is distributed over its track Eq. 4.4. This approximation is valid for moderate values of transfered energy per electron, where build-up effects can be neglected. The size a_0 is kept fixed and is in the order of magnitude of the crystal lattice spacing. In the radial dose distribution model the implemented a_0 is set to 1 Å.

The impact of variation of the core size, a_0, in the calculation of the relative effectiveness is shown for carbon ions on the right of Figure 4.17. It is possible to notice that the efficiency values for a smaller core, $a_0 = 0.5$ Å, are lower. This can be explained by noticing that dose value in the core increase with the decreasing of the core size a_0, as shown Figure 4.17 on the left.

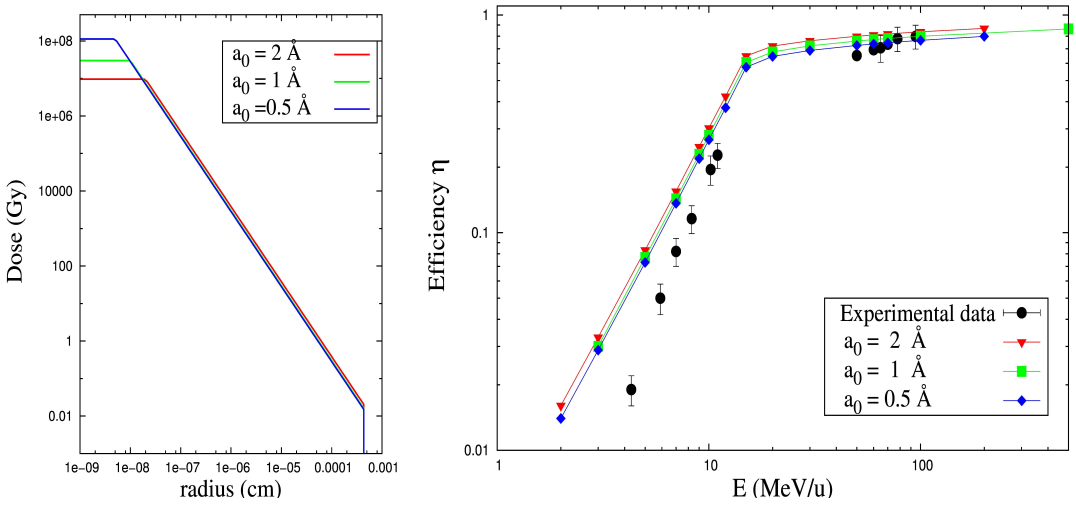

(a) (b)

FIGURE 4.17: On the left: radial dose distributions for 10 MeV/u carbon ion calculated for different values of a_0. On the right: relative effectiveness calculations of TLD-700 for carbon ion for different values of a_0 as a functions of particle energy.

4.2.2.5 Dependence on the stopping power table

Although in this work we always used the stopping power tables calculated with the code ATIMA [57], several other codes exist in literature to compute them. The impact on the efficiency calculation of using different stopping power tables will be discussed in this section.

In particular, for protons and alpha particles we also investigated respectively PSTAR and ASTAR stopping force tables which are provided by the National Institute of Standard Technology (NIST) [62]. Their values are identical to the ones reported in the ICRU report 49 [63]. These tables are theoretically evaluated for high energy values whereas, for the low energies, fitting-formulas based on experimental stopping power data are used.

For ions, we tested tables provided by the MSTAR code [64] and the ones indicated in the ICRU report 73 [65] and on its erratum and addenda [66]. The former are calculated by applying a charge scaling on the stopping force of alpha particles whereas the latter are based on theoretical considerations.

With the exception of the table from the ATIMA code, all the tables outlined above can be found in the open source library `libdEdx` [67] in which there is also an implementation of the Bethe-Bloch formula, extended to the low energies with a theoretical correction term.

On the left of Figure 4.18 the stopping force tables for several ions in LiF are shown. On the right hand side of the same figure, the impact of these tables on the calculation of the relative effectiveness calculation is reported. The calculated efficiency values do not show important variations changing the stopping power tables, these variation, indeed, are always lower then 7%.

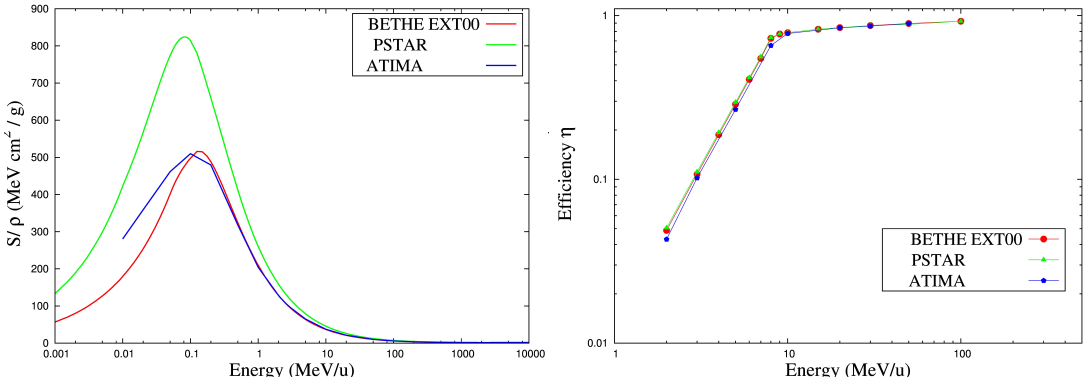

(a) Proton

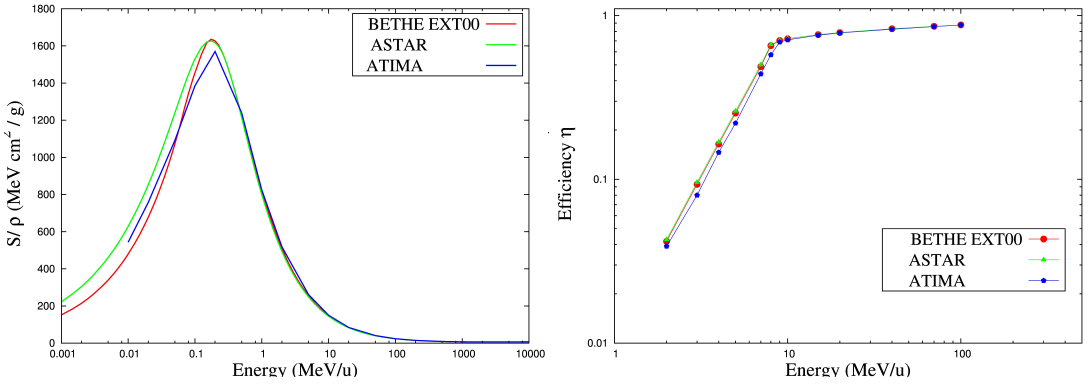

(b) Helium

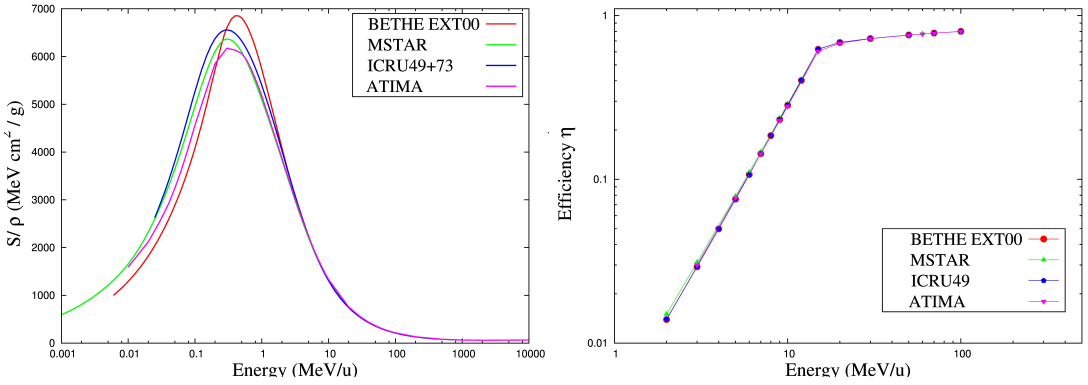

(c) Carbon

FIGURE 4.18: On the left a comparison among the different stopping power tables. On the right the impact of the different tables on the efficiency calculation.

4.2.2.6 Range straggling

A single ion energy deposition profile is characterized by a narrow Bragg peak near to the stopping point. However, this is not a realistic condition: in an ion beam, with many particles, statistical fluctuations of the energy loss in the many collision processes cause a spread of the range values, hence a Bragg peak broadening appears (as explained in

Section 1.1.2). For light ions stopped in water, range straggling amounts to about 0.1% of the mean range [7].

In the Single Ion approach this effect is not taken into account and the depth dose profile results in a sharp peak at the end of the path. Thus, depending on projectile initial energy, there are two possible conditions: the ion is completely stopped inside the detector and all the energy is deposited within the TLD or the projectile has enough energy to cross the dosimeter and the Bragg peak position will be outside the detector. Considering the range straggling, instead, these conditions are no longer the only ones possible. With range straggling it is not possible to pin down the position of the Bragg peak, especially when the ion range approaches the detector thickness. Therefore, when the Bragg peak position is close to the TLD edge, the amount of energy delivered within the detector fluctuates widely. This results in a smoothing of the efficiency curve. For example, for a carbon ion crossing a TLD 0.038 cm thick, this critical condition is expected for an energy of approximately 14.6 MeV/u.

In order to understand the impact of the range straggling on the effectiveness calculation, the Single Ion code has been modified. In this version, the fluctuations on the ion range are reproduced by associating to the ion under consideration a Gaussian energy distribution with mean value equal to the nominal energy of the beam. However, it has been observed that the impact of the range straggling is negligible. As mentioned above, indeed, the fluctuations on the range are approximately 0.1% of the mean range. To have such uncertainties on the mean range, the fluctuations of the energy should be of the order of 1% or lower.

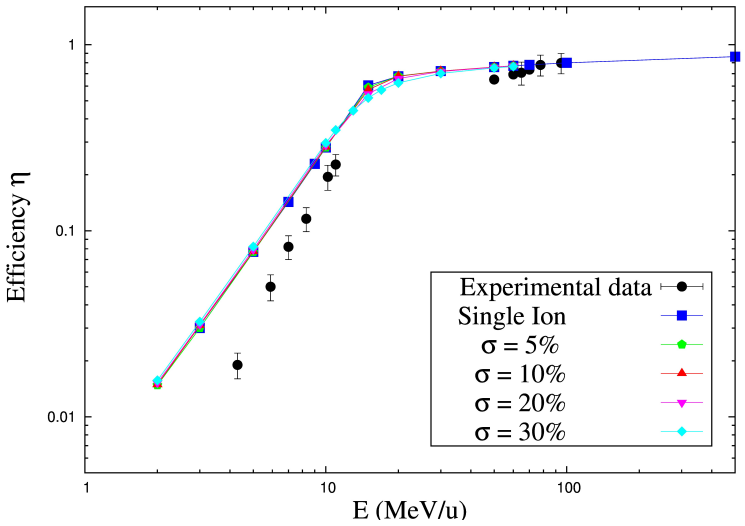

FIGURE 4.19: Efficiency calculation for carbon ions taking into account the range straggling. The incident energy is provided by a Gaussian energy distribution with different standard deviations.

For carbon ions, the impact of the range straggling starts to be visible for energy distributions with σ of approximately the 10% of the mean energy. In this case, in the energy region in which the range straggling effect should be more pronounced (around 14.6 MeV/u for carbon ions), variations on the efficiency values on the order of 5% can be expected. As limit condition fluctuations on the efficiency around 15% have been observed in the same energy region, for an energy distribution with standard deviation equals to 30% of the mean energy, as reported in Figure 4.19.

4.2.3 Comparison with the CPP

The results given from the Single Ion approach have been compared with another "LEM-like" model, namely the compound Poisson processes (CPP).

As mentioned in Section 3.2.3.1, the original version of CPP assumes an infinitesimally thin target. In order to make the two models comparable, therefore, the CPP program has been modified and the detector thickness has been introduced. The sampling along the thickness is obtained by dividing the detector in slices whose thickness is adjusted in a such way that the energy deposited on each slice is constant within 5%. A TLD thickness of 0.038 cm has been chosen, according with the one used in Geiss experimental data [2] and in the Single Ion approach.

A comparison between the modified version of the CPP and Single Ion efficiency calculations is shown in Figure 4.20. Both calculations were performed for fluence values of 10^7 cm^{-2} using the low-LET dose response curves proposed by Geiss in his PhD thesis, Eq. 4.1, and the same radial dose distribution used in ECLaT Eq. 4.2.

As shown in Figure 4.20, although the general tendency of both the models is the same, the efficiency values calculated with the CPP and and those calculated with the Single Ion approach show a remarkable deviation. Furthermore, the present model data seem surprisingly to show a better agreement with experimental data. The source of these discrepancies are not fully understood at the moment, and represent one of the directions of further investigation arising from the present work.

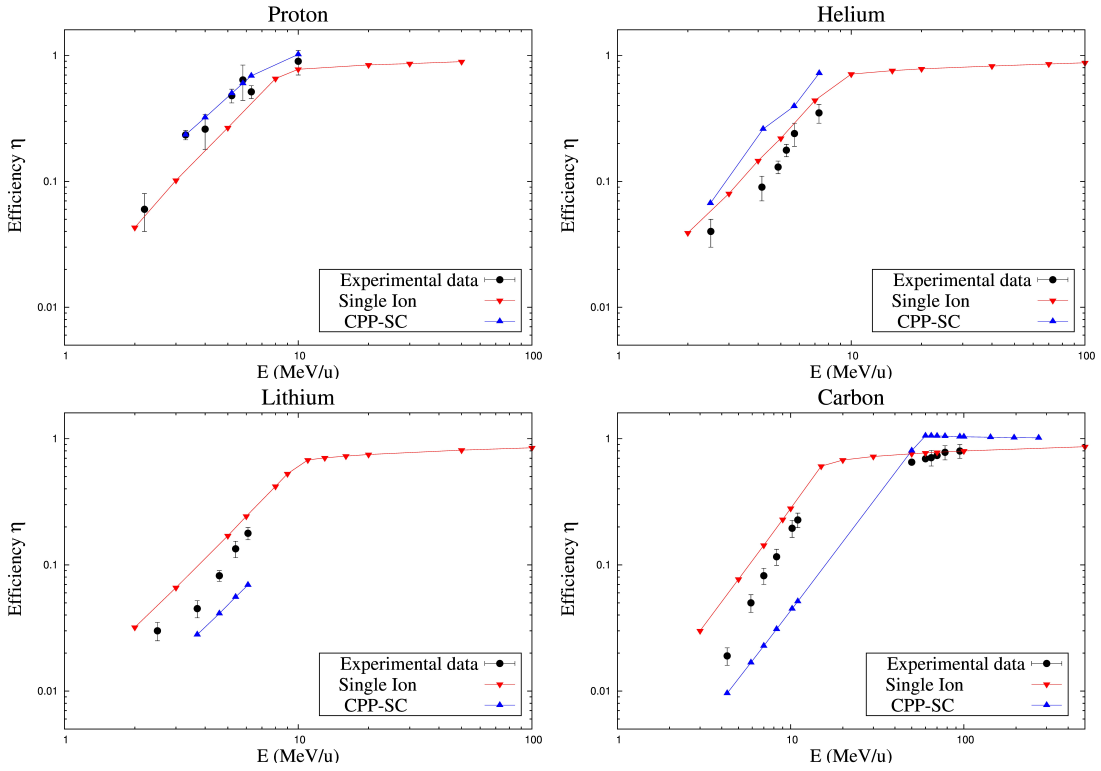

FIGURE 4.20: Efficiency calculation with the Single Ion approach, in red, and with the modified version of the CPP, in blue. The lines are eye guides connecting the point. The data for the CPP were kindly provided by S.Greilich

4.3 Calculation of the detector response for a macroscopic target irradiation with TRiP98

TRiP98 (TReatment planning for particle) is a code dedicated to the planning of radiotherapy with energetic ions, in particular ^{12}C, developed during the pilot project at GSI facility in 1997-2008 [54] [68]. This software is designed to cooperate with three dimensional active dose shaping devices like the GSI raster scan system , now available also in the most modern ion therapy centers of the world (HIT, CNAO, Med Austron, etc.). A schematic representation of the program is reported in Figure 4.21.

Presently, TRiP98 is mainly used as a research platform for heavy ion radiation therapy. Furthermore, thanks to its modular structure, it is particularly suitable to be extended in several different directions such as the multiple field optimization, the handling of moving targets, treatment with multiple ions, consideration of the oxygenation level, etc [69].

Moreover it allows not only dose calculation, but also predicting detector responses in

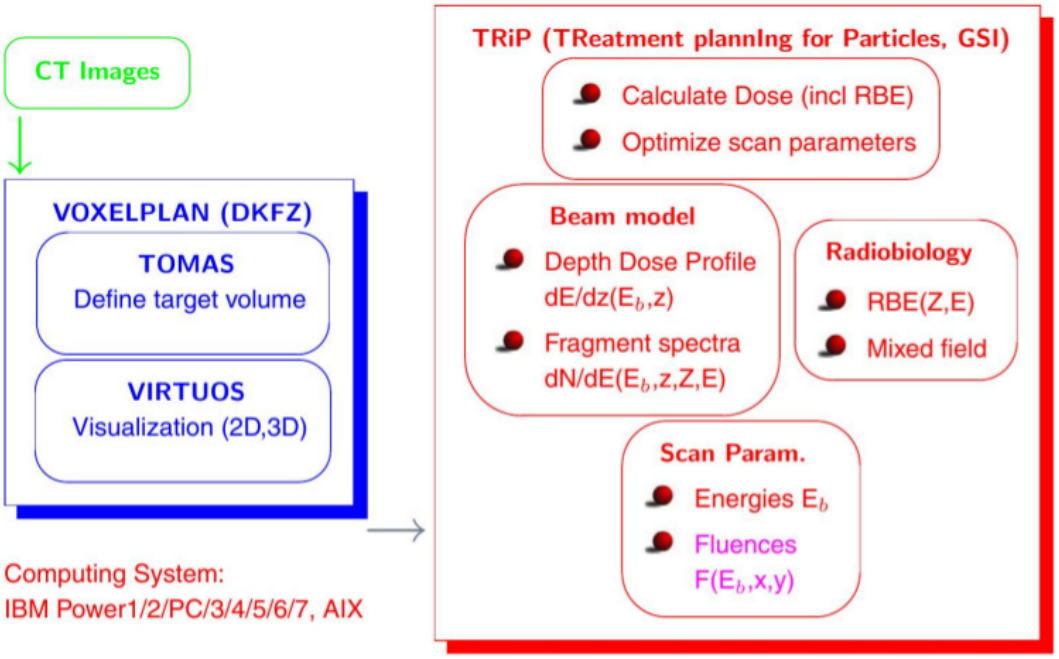

FIGURE 4.21: Schematic representation of the treatment planning system for particles TRiP98.

the mixed radiation field generated in a macroscopic target irradiation, for plan verification issues. In particular, a module for predicting the response calculation of solid state dosimeters was implemented. This implementation assumes the knowledge of the dosimeter's look up tables of relative effectiveness (RE). Indeed, the dosimeter response as a function of the position of the detector in a mixed field, $\vec{x}$, can be calculated combining the fragmentation spectra with the RE of different ions species, Z, and different energies, E (see Figure 4.22 for a schematic diagram of how the detector signal calculation is implemented on TRiP98). Thus, the signal can be calculated as

$$S(\vec{x}) = cost \times \sum_{i=1}^{Z_{proj}} \int_0^{E_0} \frac{dN}{dE}(\vec{x}, Z_i, E) \left(\frac{dE}{dx} \frac{1}{\rho} \right)_i \eta_{det}(Z_i, E) dE. \tag{4.18}$$

where $\left(\frac{dE}{dx}\frac{1}{\rho}\right)_i$ is the mass stopping power in the detector medium, $\frac{dN}{dE}(\vec{x}, Z, E)$ are the fragmentation spectra and $\eta_{det}(Z_i, E)$ is the detector relative effectiveness.

TRiP98 takes a computed tomography (CT) image as input. The CT is divided in voxels and the dose is calculated in the center of each voxel. Moreover the dosimeter is treated as a small CT (called micro-CT) embedded in to the larger phantom CT in order to allow signal calculation either on each microvoxel either as an average. The signal is then obtained by taking into account the overlap among the raster points of the beam scan system and the voxels of the micro CT (i.e. the micro-voxels). Furthermore, the detector is represented as a water-equivalent path-length inside the phantom CT, in order to reproduce the distortion that it leaves on the field.

In this section we aim at analyzing the impact of our computed efficiency tables when imported in a treatment planning tool for computing detector responses in a macroscopic irradiation of a phantom. This becomes especially important when considering the mixed radiation field generated by an extended target irradiation with the superimposition of several beam energies.

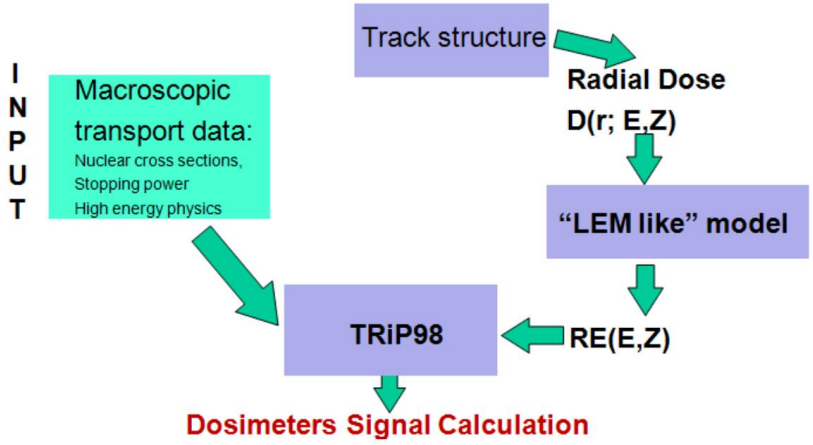

FIGURE 4.22: Schematic representation of detector signal calculation with TRiP98.

4.3.1 Implementation of the Single Ion efficiency table on TRiP98

Both ECLaT and Single Ion generate look-up tables of Relative Effectiveness for TLDs. In this section signal calculations with the efficiency table provided by these two approaches will be compared. However, the current version of TRiP98 can only handle radiographic film dosimeter, which are characterized by a different dose response [20]. For this reason, in this work, a slightly modified version of TRiP98 has been used, which also can calculate TLD signals. This version was developed by A.Carlino [70]

At first, the detector signal has been calculated for a single depth dose profile for 195 MeV/u ^{12}C ion beam. The impact of the two different tables is shown in Figure 4.23 where in red is represented the dose profile calculated by TRiP98 whereas the computed TLD-700 detector responses are reported in blue for ECLaT efficiency tables and in green for the ones provided by the Single Ion approach. The two calculations differs by as much as 17%. Unfortunately no experimental data are available for comparison.

We then considered an extended target irradiation (what is called spread out Bragg peak for irradiation with passive energy degradation), considering a 3 cm thick water target at a depth of 11 cm; we scanned the target with 28 energies, from a proximal energy of 234.6 MeV/u to a distal one of $E_{max} = 267.2$ MeV/u. Figure 4.24 shows a comparison between TRiP98 planned dose (in red) and the computed TLD signal response in the

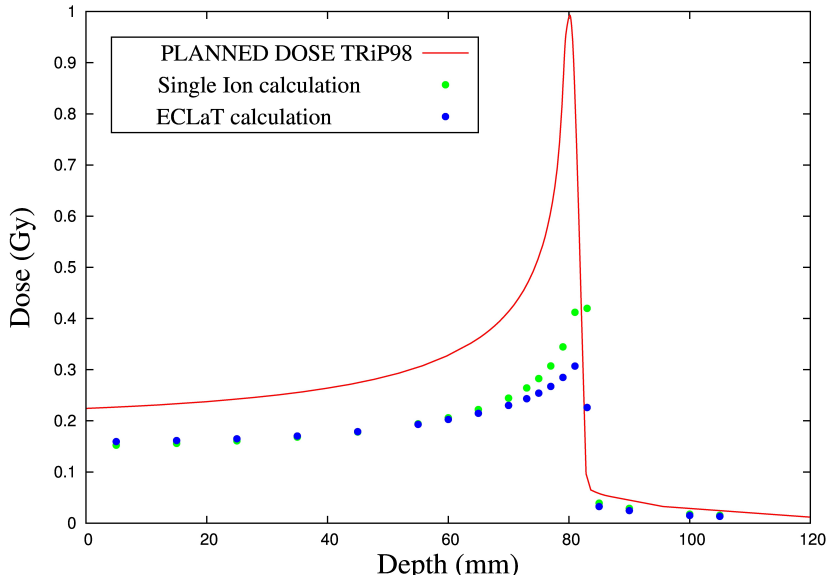

FIGURE 4.23: Detector response calculation for a single depth dose profile for 195 MeV/u ^{12}C ion beam calculated by TRiP98 (in red) and the computed TLD700 response in the beam eye view direction for ECLaT efficiency tables (in blue) and for the ones provided by the Single Ion approach (in green).

beam eye view direction for ECLaT efficiency tables (green) and the TLD700 response computed with the efficiency tables according to the Single Ion approach (blue). The prescribed physical dose to the target is 1 Gy. The black dots are experimental data measured during a recent beam-time at HIT and kindly provided by A.Carlino [70] The read out procedure of these data has been done by Dr. Thomas Berger, DLR (Institute for Aerospace Medicine, Cologne) .

As shown in Figure 4.23, the green curve of ECLaT and the blue curve of the Single Ion approach describe the data with similar accuracy.

Furthermore it is possible to notice that, for low ion energies (*i.e.* in the target region), the signal computed using the Single Ion efficiency tables seems to overestimate the experimental data. This behavior can be explained by noticing that also the relative effectiveness values provided by the Single Ion approach overestimates the experimental measurements, Figure 4.8

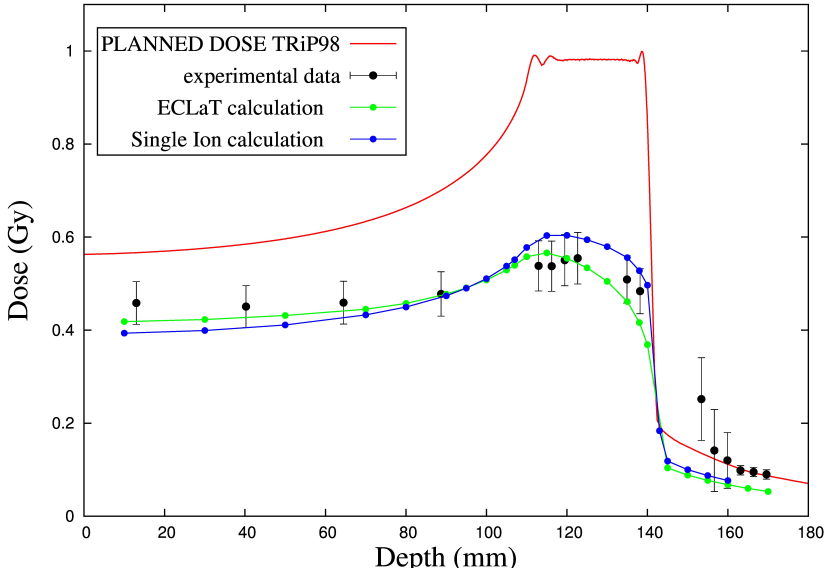

FIGURE 4.24: Depth dose distribution comparison among the planned dose by TRiP98, in red, and the computed TLD response calculated importing ECLaT efficiency tables, in blue, and the one provided by the single ion approach, in green.

Conclusions

In this work we studied the response of thermoluminescent detectors (TLDs) when irradiated with heavy ions. The dose response curve of these detectors is highly non-linear, and moreover it also strongly depends on the quality and on the energy of the radiation field. Thus, in order to extend the use of TLDs to heavy charged particle fields, precise efficiency tables must be established over a broad range of energy and particle charge.

Several theoretical approaches to describe the TLDs behavior exist in literature and in this work we focused on an extension of the 'local effect model' (LEM)[1]. This model stems from an amorphous track structure model and assumes the knowledge of both the radial dose distribution around heavy ion trajectories and the detector response to reference radiation.

In this context, an algorithm was developed by Giess et al. at GSI [2] with the aim of computing efficiency tables for heavy charged particle radiation fields. Although this approach has been well received, thanks to its simplicity and the good agreement with experimental data, some inconsistencies have been pointed out by Bassler [39], which limit the robustness of this method. In a first phase of this thesis work we tried to fix these issues, however we couldn't find any affordable solution without modifying the whole setup of the method.

For this reason a new, simple analytical approach, the Single Ion approach, has been developed and applied to calculate relative effectiveness tables for particles with different energy E and charge Z. This method computes the detector response starting from the response of a single ion of the beam. The dose contributions coming from the neighboring tracks are assumed to sum up linearly and this represents the main assumption (and thus limitation) of the model. For this reason particular care has been used in studying the effects of the overlap between neighboring tracks. It was found that the Single Ion approach is realistic only in the low fluence approximation, moreover it was also observed that the loss of linearity in the overlap region occurs, for more energetic ions, at larger fluence. The robustness of this approach against modifications of the radial dose

distribution of a single ion in the detector, as well as to different detector response models and different stopping power tables, has been verified. Furthermore, the calculated efficiency values have been compared with experimental data from Geiss [2], as well as with calculated values provided by different approaches, such as the compound Poisson process (CPP). Efficiency values calculated with the CPP and those calculated with the Single Ion approach show a remarkable deviation. Furthermore, the present model data seem surprisingly to show a better agreement with experimental data. These results were unexpected since the two methods are quite similar and the present one has a higher level of approximation. The source of these discrepancies are not fully understood at the moment, and represent one of the directions of further investigation arising from the present work. Moreover, in the experimental literature ambiguous findings on the efficiencies for various particle species are reported, and some doubts on the data used as comparison also in the present work have been raised by Ávila et al. [61]. For this reason, it would be of extreme importance to perform new reliable efficiency measurements as a benchmark to compare with.

Finally, we implemented our model data in the treatment planning code TRiP98 [68] and we performed signal calculations on macroscopic targets irradiated with an extended Carbon field. Also these results were compared with recent experimental measurements performed by Carlino [70] as well as with Geiss ECLaT calculations. As for pure efficiency calculations the agreement with the data is not perfect, however the accuracy in reproducing experimental results of the Single Ion approach is comparable with the accuracy showed by ECLaT.

We can therefore conclude that, although the Single Ion approach is at a first stage of development it is robust and shows an accuracy level comparable with previous calculations. Moreover, being analytical, it is computationally fast and can be efficiently integrated in treatment planning verification tools. All these characteristic make us confident and we are looking for new possible extensions allow to consider the method a valid alternative to the previous approaches, and open the way to its further extension, including incorporation of corrections for higher fluence values.

Bibliography

[1] M. Scholz and G. Kraft. Track structure and the calculation of biological effects of heavy charged particles. *Adv. Space Res.*, 18:5–14, 1996.

[2] O. B. Geiß, M. Krämer, and G. Kraft. Efficiency of thermoluminescent detectors to heavy charged particles. *Nuclear Instruments and Methods in Physics Research B*, 142:592–598, 1998.

[3] G. F. Knoll. *Radiation detection and measurement.* Jhon Wiley and Sons, 2000.

[4] W. R. Leo. *Tecniques for Nuclear and Particle Phyisics Experiments.* Springer Vrlag, 1993.

[5] F. M. Khan. *The Physics of Radiation Therapy.* Lippincott Williams and Wilkins, 2012.

[6] International Commission on Radiation Units and measurements, ICRU. Fundamental quantities and units for ionizing radiation. Technical report, 1998.

[7] D. Schardt, T. Elsässer, and D. Schulz-Ertner. Heavy-ion tumor therapy: Physical and radiobiological benefits. *Reviews of Modern Physics*, 82:383–425, 2010.

[8] W. H. Barkas. *Nuclear research emulsions. Vol.1: Techniques and theory.* 1963.

[9] D. Schardt, P. Steidl, M. Krämer, U. Weber, K. Parodi, and S. Brons. Precision Bragg-curve measurements for light-ion beams in water. *GSI-Report 2008-1 (GSI Scientific Report 2007)*, page 373, 2008 (unpublished).

[10] E. Haettner, H. Iwase, and D. Shardt. Experimental fragmentation studies with ^{12}C therapy beams. *Radiation Protection Dosimetry*, 122:485 – 487, 2006.

[11] R. F. Laitano. *Fondamenti di dosimetria delle radiazioni ionizzanti.* ENEA, 2011.

[12] Krämer M. et Durante M. Ion beam transport calculations and treatment plans in particle therapy. *Eur. Phys. J. D*, 2010.

[13] M. Krämer. Calculations of heavy-ion track structure. *Nuclear Instruments and Methods in Physics Research B*, 105:14–20, 1995.

[14] M. Scholz. Effects of ion radiation on cells and tissues. *Adv. Polym. Sci.*, 62:96–155, 2003.

[15] W.K. Weyrather. Medical applications of accelerated ions. In Jim Al-Khalili and Ernst Roeckl, editors, *The Euroschool Lectures on Physics with Exotic Beams, Vol. I*, volume 651 of *Lecture Notes in Physics*, pages 469–490. Springer Berlin Heidelberg, 2004.

[16] International Commission on Radiation Units and measurements, ICRU. Determination of Absorbed Dose in a Patient Irradiated by Beams of X or Gamma Rays in Radiotherapy Procedures . Technical report, 1976.

[17] C.P. Karger, O. Jäkel, H.Palmans, and Tatsuaki K. Dosimetry for ion beam therapy. *Phys. Med . Biol*, 55:R193–R234, 2010.

[18] R. Herrmann. *Prediction of the response behaviour of one hit detectors in particla beams.* PhD thesis, Department of physics and astronomy, Aarhus Universit, Denmark, 2012.

[19] F. H. Attix. *Introduction to Radiological Physics and Radiation Dosimetry.* John Wiley and Sons, 1987.

[20] B. Spielberger et al. Calculation of the x-ray film response to heavy charged particle irradiation. *Phys. Med. Biol.*, 47:410720, 2002.

[21] A.J.J. Bos. Theory of thermoluminescence. *Radiation Measurements*, 41:S45–S56, 2007.

[22] P. Olko. Microdosimetry, track structure and the response of thermoluminescent detectors. *Radiation Measurements*, 41:S57–S70, 2007.

[23] A.J.J. Bos. On the energy conversion in thermoluminescence dosimetry materials. *Radiation Measurements*, 33:737–744, 2001.

[24] W.H. Lucke and NAVAL RESEARCH LAB WASHINGTON D C. *Intrinsic Efficiency of Thermoluminescent Dosimetry Phosphors.* Defense Technical Information Center, 1970.

[25] T. Berger and M. Hajek. TL-efficiency-Overview and experimental results over the year. *Radiat. Meas.*, 43:146 – 156, 2008.

[26] R. Katz. Track structure theory in radiobiology and in radiation detection. *Nuclear Track Detection*, 2(1):1 – 28, 1978.

[27] F. A. Cucinotta, R. Katz, J. W. Wilson, and R. R. Dubey. Heavy ion track-structure calculations for radial dose in arbitrary materials. *NASA Thecnical Memorandum 3497*, 1995.

[28] A. Chatterjee and H.J. Schaefer. Microdosimetric structure of heavy ion tracks in tissue. *Radiation and Environmental Biophysics*, 13:215–227, 1976.

[29] J.K. Olsen and J.W. Hansen. Experimental and calculated effectiveness of radiochromic dye film to stopping 21 MeV ^{7}Li and 64 MeV ^{16}O . *NIM B*, 5: 497–504, 1984.

[30] W. Gieszczyk, P. Bilski, P. Olko, and B. Obryk. Radial distribution of dose within heavy charged particle tracks-model and experimental verification using LiF:Mg,Cu,P TL detectors. *arXiv:1401.6653*, 2014.

[31] R. Herrmann et al. Dose response of alanine detectors irradiated with carbon ion beams. *Medical Physics*, 38:1859–1866, 2011.

[32] J. Kalef-Ezra and Y.S. Horowitz. Heavy charged particle thermoluminescence dosimetry: track structure theory and experiments . *Int. J. Appl. Radit. Isot.*, 33:1085–1100, 1982.

[33] R. Herrmann, S. Greilich, L. Grzanka, and N. Bassler. Amorphous track predictions in libamtrack for alanine relative effectiveness in ion beams. *Radiation Measurements*, 46(12):1551 – 1553, 2011.

[34] H. Nikjoo, S. Uehara, D. Emfietzoglou, and F.A. Cucinotta. Track-structure codes in radiation research. *Radiation Measurements*, 41(910):1052 – 1074, 2006.

[35] J. J. Butts and R. Katz. Theory of RBE for heavy ion bombardment of dry enzymes and viruses. *Radiat. Res.*, 30:855–871, 1967.

[36] L. Larsson and R. Katz. Supralinearity of Thermoluminescent Dosimeters. *Nucl.Instrum.Meth.*, 138:631–636, 1976.

[37] M.P.R. Waligorski and R. Katz. Supralinearity of peak 5 and peak 6 in TLD-700. *Nucl.Instrum.Meth.*, 175:48–50, 1980.

[38] Z. Chuxiang, D.E. Dunn, and R. Katz. Radial distribution of dose and cross-sections for the inactivation of dry enzymes and viruses. *Radiation Protection Dosimetry*, 13:215–218, 1985.

[39] N. Bassler. *Experimental studies relevant for antiproton cancer therapy.* PhD thesis, Department of Physics and Astronomy, Faculty of Science, University of Aarhus, 2006.

[40] J.W. Hansen. *Experimental investigation of the suitabilty of the track structure theory in describing the relatve effectiveness of high-LET irradiation of physical radiation detectors.* PhD thesis, Risø National Laboratory, DK-4000 Roskilde. Risø-R-507, 1984.

[41] A. Chatterjee and H.J. Schaefer. Microdosimetric structure of heavy ion tracks in tissue. *Radiation and Environmental Biophysics*, 13(3):215–227, 1976.

[42] E.W. Claffy, C.C. Klick, and F.H. Attix. *Thermoluminescence processes and color centers in LiF:Mg.Proceedings of the 2nd. International Conference on Luminescence Dosimetry*, pages 302–308. 1968.

[43] F.H. Attix. Further consideration of track interaction model for thermoluminescence in LiF (TLD-100). *Journal of applied physics*, 46(1):81–88, 1975.

[44] Y.S Horowitz. The role of microdosimetry in heavy charged particle induced thermoluminescence dose response. *Thermochimica Acta*, 135:127–132, 1988.

[45] Y.S Horowitz, D. Satinger, L. Oster, N. Issa, M.E. Brandan, O. Ávila, M. Rodríguez-Villafuerte, I. Gamboa-deBuen, A.E. Buenfil, and C. Ruiz-Trejo. The extended track interaction model: supralinearity and saturation he-ion tl fluence response in sensitized tld-100. *Radiation Measurements*, 33:459–473, 2001.

[46] Y.S Horowitz, O. Ávila, and M. Rodríguez-Villafuerte. Theory of heavy charged particle response (efficiency and supralinearity) in tl materials. *Methods in Physics Research B*, 184:85–112, 2001.

[47] M. Scholz. Calculation of RBE for normal tissue complications based on charged particle track structure. *Bulletin du Cancer/Radiothrapie*, 83, Supplement 1(0):50s – 54s, 1996.

[48] M. Scholz, A. M. Kellerer, W. Kraft-Weyrather, and G. Kraft. Computation of cell survival in heavy ion beams for therapy. *Radiation and Environmental Biophysics*, 36(1):59–66, 1997.

[49] A.M. Kellerer. *Fundamentals in microdosimetry.* In: The Dosimetry of Ionizing Radiation, chapter 2. Kase.K.R. and Bjärngard, B.E. and Attix, F.H. Eds. Academic Press, 1985.

[50] S. Greilich, U. Hahn, M. Kiderlen, C.E. Andersen, and N. Bassler. Efficient calculation of local dose distribution for response modelling in proton and ion beams. *arXiv preprint arXiv:1306.0185*, 2013.

[51] S. Greilich, L. Grzanka, N. Bassler, C.E. Andersen, and O. Jäkel. Amorphous track models: a numerical comparison study. *Radiation Measurements*, 45:1406–1409, 2010.

[52] L. Grzanka, S. Greilich, M. Korcyl, O. Jäkel, M. Waligórski, and P. Olko. The application of amorphous track models to study cell survival in heavy ions beams. *Radiation protection dosimetry*, 143(2-4):232–236, 2011.

[53] O. B. Geiß, M. Krämer, and G. Kraft. Verification of heavy ion dose distributions using thermoluminescent detectors. *Nuclear Instruments and Methods in Physics Research Section B: Beam Interactions with Materials and Atoms*, 146(14):541 – 544, 1998.

[54] M. Krämer, O. Jäkel, T. Haberer, G. Kreft, and Weber u. Treatment planning for heavy-ion radiotherapy: physical beam model and dose optimization. *Phys.Med. Biol.*, 45:3299–3317, 2000.

[55] B. Majborn, L. Bøtter-Jensen, and P. Christensen. *On the Relative Efficiency of TL Phosphors for High-Let Radiation.Proceedings of the 5th International Conference on Luminescence Dosimetry*, pages 124–130. 1977.

[56] O.B. Geiß. *Strahleninduzierte prozesse in LiF kristallen und verifikation dreidimensionaler dosisverteilungen nach shwerionenbestrahlung.* PhD thesis, University GhK Kassel, Germany, 1997.

[57] GSI. ATIMA, calculating ATomic Interaction with MAtter. unpublished. https://www.gsi.de.

[58] E.R. Benton, A.L. Frank, and E.V. Benton. TLD efficiency of ^{7}LiF for doses deposited by high-LET particles . *Radiation Measurements*, 32(3):211 – 214, 2000.

[59] P. Schmidt, J. Fellinger, and K. Hübner. Experimental Determination of the TL Response for Protons and Deuterons in Various Detector Materials. *Radiaton Protection Dosimetry*, 33(1-4):171–173, 1990.

[60] W. Gieszczyk, P. Bilski, P. Olko, R. Herrmann, H. Kettunen, A. Virtanen, and N. Bassler. Evaluation of the relative thermoluminescence efficiency of LiF:Mg,Ti and LiF:Mg,Cu,P TL detectors to low-energy heavy ions. *Radiation Measurements*, 5152(0):7 – 12, 2013.

[61] O. Ávila, M. Rodríguez-Villafuerte, I. Gamboa-deBuen, P. Avils, D. Estrada, A.E. Buenfil, C. Ruiz-Trejo, P. González, M.E. Brandan, and Y.S. Horowitz. On the correct measurement of relative heavy charged particles to gamma thermoluminescent efficiencies. *Radiat Prot Dosimetry*, 100((1-4)):87–90, 2002.

[62] M.J. Berger, J.S. Coursey, M.A. Zucker, and J. Chang. (2005). ESTAR, PSTAR and ASTAR: Computer Programms for Calculating Stopping-Power and Range Tables for Electrons, Protons and Helium Ions (version 1.2.3).

[63] International Commission on Radiation Units and measurements, ICRU. Stopping power and ranges for protons and alpha particles. Technical report, 1993.

[64] H. Paul and A. Shinner. An emphirical approach to the stopping power of solids and gases for ions from $_3$Li to $_{18}$Ar. *Nucl. Inst. Meth. B*, 179:299 – 315, 2001.

[65] P. Sigmund, R. Bimbot, H. Geissel, H. Paul, and A. Shinner. Stopping of ions heavier than Helium . *Journal of the ICRU*, 5(1), 2005.

[66] P. Sigmund, A. Shinner, and H. Paul. Errata and Addenda:ICRU report 73 (Stopping of ions heavier than Helium) . 2009.

[67] A. Lühr, J. Toftegaard, I. Kantemiris, D.C. Hansen, and N. Bassler. Stopping power for particle therapy: The generic library libdedx and clinically relevant stopping-power ratios for light ions. *International Journal of Radiation Biology*, 88(1-2): 209–212, 2012.

[68] M. Krämer and M. Scholz. Treatment planning for heavy-ion radiotherapy: calculation and optimization of biologically effective dose. *Phys.Med. Biol.*, 45:3319–3330, 2000.

[69] E. Scifoni, W. Tinganelli, W.K. Weyrather, M. Durante, and M. Maier, A. Krämer. Including oxygen enhancement ratio in ion beam treatment planning: model implementation and experimental verification. *Pub.Med.*, 58:3871–95, 2013.

[70] A. Carlino. Dosimetric characterization of proton and carbon ion beams:comparison between experiments and tps data. Master's thesis, Scuola di Specializzazione in Fisica Medica, Università degli studi di Palermo, 2012.

Acknowledgements (*Ringraziamenti*)

Per questo lavoro di tesi devo ringraziare per primi i miei relatori, la Prof.ssa Valeria Rosso e il Prof. Marco Durante, che mi hanno sostenuta e appoggiata durante questo percorso e, soprattutto, per le enormi opportunità che mi hanno dato. My sincere thanks goes to Michael Kraemer, for introducing me to the TLDs and, mostly, for his precious suggestions. *Un pensiero speciale lo devo a Emanuele Scifoni, il quale, oltre ad avermi seguito durante tutte le fasi di questo lavoro, mi ha anche appoggiata, sostenuta, spronata e motivata per tutto questo anno passato a lavorare insieme. Ho imparato molto da lui e gli sono grata per questo.* I really thank Steffen Greilich from DKFZ (Heidelberg), Niels Bassler from Aarhus University (Aarhus) and Thomas Friedrich from GSI (Darmstadt) for the many discussions and for their helpful suggestions. *Ringrazio di cuore Claudio e Jacopo per tutto l'appoggio e l'aiuto che mi hanno dato soprattutto in questi ultimi giorni* and I really want thank to Sebastian and Christoph for helping me with all my computer issues and for the good time spent together.

Ringrazio Marta, Tugba, Francesco, Enrico e Michele per i bei momenti tedeschi. E tutti i miei amici per gli anni pisani, in particolare ci tengo a ringraziare Ettore, Beppe, Matteo, Ylenia Cristiano che non sono stati soltanto dei compagni di università e Alfredo che ha condiviso con me l'ultima fase di questa esperienza. Ovviamente ringrazio Lello per essere sempre stato al mio fianco.

Ringrazio, in fine, i miei zii che mi hanno ospitata e sopportata per un sacco di anni, la Ale che mi vuole comunque un sacco di bene e i miei genitori che si sono sacrificati e che mi hanno permesso di arrivare fino qui.